Curiosity's robotic arm-mounted Mars Hand Lens Imager (MAHLI): Characterization and calibration status

Kenneth S. Edgett, Michael A. Caplinger, Justin N. Maki, Michael A. Ravine, F. Tony Ghaemi, Sean McNair, Kenneth E. Herkenhoff, Brian M. Duston, Reg G. Willson, R. Aileen Yingst, Megan R. Kennedy, Michelle E. Minitti, Aaron J. Sengstacken, Kimberley D. Supulver, Leslie J. Lipkaman, Gillian M. Krezoski, Marie J. McBride, Tessa L. Jones, Brian E. Nixon, Jason K. Van Beek, Daniel J. Krysak, and Randolph L. Kirk

MSL MAHLI Technical Report 0001, version 2
version 1: 19 June 2015; version 2: 05 October 2015

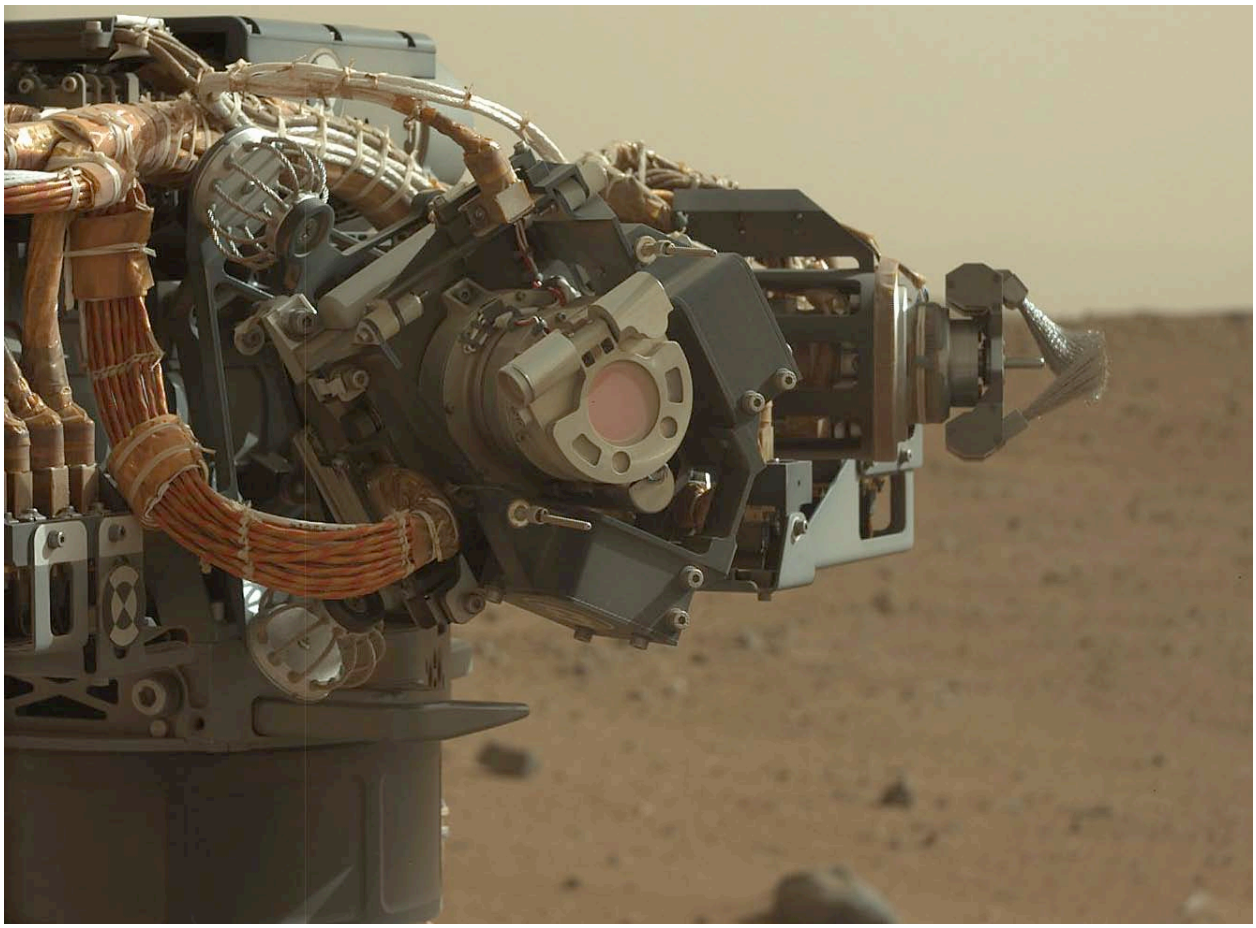

Citation: Edgett, K. S., M. A. Caplinger, J. N. Maki, M. A. Ravine, F. T. Ghaemi, S. McNair, K. E. Herkenhoff, B. M. Duston, R. G. Willson, R. A. Yingst, M. R. Kennedy, M. E. Minitti, A. J. Sengstacken, K. D. Supulver, L. J. Lipkaman, G. M. Krezoski, M. J. McBride, T. L. Jones, B. E. Nixon, J. K. Van Beek, D. J. Krysak, and R. L. Kirk (2015) Curiosity's robotic arm-mounted Mars Hand Lens Imager (MAHLI): Characterization and calibration status, *MSL MAHLI Technical Report 0001* (version 1: 19 June 2015; version 2: 05 October 2015). doi:10.13140/RG.2.1.3798.5447

Mars Science Laboratory (MSL) Mars Hand Lens Imager (MAHLI) Technical Report 0001

Cover photo

Mars Science Laboratory (MSL) rover Curiosity's Mars Hand Lens Imager (MAHLI; center) and Dust Removal Tool (DRT; right), as observed by the Mastcam-34 camera on Sol 30 (06 September 2012) in northern Gale crater, Mars. This is a portion of Mastcam image 0030ML0000400000100851E01.

Author affiliations

Michael A. Caplinger, Brian M. Duston, Kenneth S. Edgett, Tessa L. Jones[1],
Megan R. Kennedy, Gillian M. Krezoski, Daniel J. Krysak, Leslie J. Lipkaman,
Marie J. McBride, Sean McNair, Brian E. Nixon, Michael A. Ravine,
Kimberley D. Supulver, Jason K. Van Beek
Malin Space Science Systems, San Diego, California, USA

Justin N. Maki, Aaron J. Sengstacken[2], Reg G. Willson
Jet Propulsion Laboratory, California Institute of Technology, Pasadena, California, USA

F. Tony Ghaemi
Ghaemi Optical Engineering, San Diego, California, USA

Kenneth E. Herkenhoff, Randolph L. Kirk
U.S. Geological Survey, Astrogeology Science Center, Flagstaff, Arizona, USA

Michelle E. Minitti, R. Aileen Yingst
Planetary Science Institute, Tucson, Arizona, USA

[1]now at: *Cymer, San Diego, California, USA*

[2]now at: G*armin International, Olathe, Kansas, USA*

Change Log

- Version 2, 05 October 2015 – Equation 2 was incorrect; changed 3.4201 to 3.5201.

Table of Contents

Abstract

MAHLI (Mars Hand Lens Imager) is a 2-megapixel, Bayer pattern color CCD camera with a macro lens mounted on a rotatable turret at the end of the 2-meters-long robotic arm aboard the Mars Science Laboratory rover, Curiosity. The camera includes white and longwave ultraviolet LEDs to illuminate targets at night. Onboard data processing services include focus stack merging and data compression. Here we report on the results and status of MAHLI characterization and calibration, covering the pre-launch period from August 2008 through the early months of the extended surface mission through February 2015. Since landing in Gale crater in August 2012, MAHLI has been used for a wide range of science and engineering applications, including distinction among a variety of mafic, siliciclastic sedimentary rocks; investigation of grain-scale rock, regolith, and eolian sediment textures and structures; imaging of the landscape; inspection and monitoring of rover and science instrument hardware concerns; and supporting geologic sample selection, extraction, analysis, delivery, and documentation. The camera has a dust cover and focus mechanism actuated by a single stepper motor. The transparent cover was coated with a thin film of dust during landing, thus MAHLI is usually operated with the cover open. The camera focuses over a range from a working distance of 2.04 cm to infinity; the highest resolution images are at 13.9 μm per pixel; images acquired from 6.9 cm show features at the same scale as the Mars Exploration Rover Microscopic Imagers at 31 μm/pixel; and 100 μm/pixel is achieved at a working distance of ~26.5 cm. The very highest resolution images returned from Mars permit distinction of high contrast silt grains in the 30–40 μm size range. MAHLI has performed well; the images need no calibration in order to achieve most of the investigation's science and engineering goals. The positioning and repeatability of robotic arm placement of the MAHLI camera head have been excellent on Mars, often with the hardware arriving within millimeters of expectation. Stability while imaging is usually such that the images are sharply focused; some exceptions—thought to result from motion induced by wind—have occurred during longer exposure LED-illuminated night imaging. Image calibration includes relative radiometric correction by removal of dark current and application of a flat field. Dark current is negligible to minor for typical daytime exposure durations and temperatures at the Gale field site. A pre-launch flat field product is usually applied to the data but new products created from images acquired by MAHLI of the Martian sky are superior and can provide a relative radiometric accuracy of ~6%. The camera lens imparts negligible distortion to its images; camera models derived from pre-launch data, with CAHV and CAHVOR parameters captured in their archived labels, can be applied to the images for analysis. MAHLI data and derived products, including pre-launch images, are archived with the NASA Planetary Data System (PDS). This report includes supplementary calibration and characterization data that are not available in the PDS archive (see supplement file **MAHLITechRept0001_Supplement.zip**).

1 Introduction

Curiosity—the Mars Science Laboratory (MSL) rover—landed in northern Gale crater in August 2012. Mounted on the turret at the end of Curiosity's robotic arm, the Mars Hand Lens Imager (MAHLI) is a 2-megapixel color camera with a macro lens that can image targets at scales as high as 13.9 µm per pixel. The MSL science and engineering teams have used MAHLI for a wide range of science and scientific support imaging efforts, including geologic investigation of grain-scale characteristics of rocks, regolith and eolian deposits; range-finding in support of robotic sample extraction; documentation of samples and sample extraction sites; documentation of *in situ* geochemical analysis sites; examination and monitoring of particulate accumulation on hardware and instrumentation; inspection and diagnosis of instrument and hardware problems (such as wheel damage); and examination of the landscape and suspended dust in the atmosphere (*e.g.*, Blake *et al*., 2013; Minitti *et al*., 2013; Robinson *et al*., 2013a; Grotzinger *et al*., 2014; Stack *et al*., 2014; Campbell *et al*., 2014; Berger *et al*., 2014; Yingst *et al*., 2014).

This is a status report that describes the results of MAHLI characterization and calibration studies we performed on data acquired before launch, during the primary surface mission, and in the early months of the extended mission on Mars, through February 2015. We provide insights into the data set and access to information about the instrument and data that are unavailable elsewhere. The information herein, including the accompanying **Supplementary Materials (file MAHLITechRept0001_Supplement.zip)**, can be used by investigators who desire to improve upon our characterization or calibration, as needed, for specific scientific applications. Further, this report is a critical reference for data users who need to know how to determine the scale of features in MAHLI images and how to use the focus merge products produced by the instrument.

2 Mission and MAHLI overview

2.1 MSL mission

The integrated MSL cruise stage, aeroshell, descent stage, and Curiosity rover were launched from the Cape Canaveral Air Force Station, Florida, USA, on 26 November 2011 (Grotzinger *et al*., 2012). The spacecraft reached Gale on 06 August 2012 and the rover landed at latitude 4.5895°S, longitude 137.4417°E, in a valley between the crater's north wall and Aeolis Mons (informally known as Mount Sharp) to the south (Vasavada *et al*., 2014).

The MSL mission seeks evidence for habitable environments on Mars, particularly as recorded in the rock record (Grotzinger, 2009; Grotzinger *et al*., 2012; Grotzinger *et al*., 2015). The field site was selected for its abundant evidence of past interaction of water with rock and evidence for alluvial, fluvial, and possibly lacustrine, sedimentation (Cabrol *et al*., 1999; Malin and Edgett, 2000; Anderson and Bell, 2010; Milliken *et al*., 2010; Thomson *et al*., 2011; Wray, 2012; Siebach and Grotzinger, 2014). The mission's early geological results—to which investigation of MAHLI images contributed—include identification of fluvial conglomerates and sandstones

(Williams *et al*., 2013; Grotzinger *et al*., 2014; Kah *et al*., 2015); mudstones interpreted to contain organic molecules and a record of a past, habitable environment (Grotzinger *et al*., 2014; Vaniman *et al*., 2014; Freissinet *et al*., 2015); and the first *in situ* (on Mars) absolute age-dates for a sedimentary rock body and the timing of its re-exposure at the Martian surface (Farley *et al*., 2014).

2.2 MAHLI instrument and investigation

Edgett *et al*. (2012) described the MAHLI instrument and investigation; DiBiase and Laramee (2009) described the lens housing and mechanisms; and Ghaemi (2009) described the optics design. The investigation centers on grain-scale texture, structure, mineralogy, morphology, and stratigraphy of geologic material at the field site in Gale crater. The instrument consists of three hardware elements, a camera head on the rover's robotic arm turret (**Figure 1**), a digital electronics assembly (DEA) housed inside the rover's temperature-controlled body, and a calibration target mounted on the exterior of the robotic arm's shoulder azimuth actuator housing. Jandura *et al*. (2010) and Anderson *et al*. (2012) described the position of the MAHLI camera head on the turret and the nature of other tools on the arm, including sample collection devices in the form of a scoop and a drill.

MAHLI is a color camera with a focusable macro lens. It can focus on subjects at working distances of 2.04 cm to infinity with pixel scales ranging from as high as 13.9 µm/pixel at 2.04 cm range to 100 µm/pixel at ~26.5 cm range to even lower resolution at infinity focus. The image sensor is an ON Semiconductor (formerly Truesense Imaging; formerly Kodak) KAI-2020CM interline transfer charge-coupled device (CCD) without the standard cover glass. It has 1600 by 1200, 7.4 µm square photoactive pixels and color is achieved using red, green, and blue filtered microlenses arranged in a Bayer pattern (Bayer, 1976).

At the minimum working distance, the diagonal field of view (FOV) is 34°, the instantaneous field of view (IFOV) is 402 µrad, the focal ratio is f/9.8, and the effective focal length is 18.4 mm; at infinity focus, these values are 38.5°, 346 µrad, f/8.5, and 21.4 mm. **Table 1** provides details. An operable dust cover protects the MAHLI front lens element, composed of sapphire, from contamination. The dust cover has a transparent Lexan™ window so that images can be acquired and the LEDs can illuminate targets through the cover when it is closed. MAHLI has four white light and two longwave (365 nm) ultraviolet (UV) LEDs to illuminate targets for use, when desired, at night. Onboard the instrument data processing options include a focus merge capability, lossless and lossy data compression, and thumbnail (approximately 1/8th size) image production.

Table 1. MAHLI focal ratio, effective focal length, and fields of view

working distance (cm)	focal ratio (f/number)	effective focal length (mm)	IFOV (µrad)	diagonal FOV (°)	horizontal FOV (°)	vertical FOV (°)
2.25	9.80	18.39	402.4	33.8	26.0	19.5
2.81	9.52	18.69	395.9	34.8	26.8	20.1
3.75	9.22	19.06	388.2	36.0	27.6	20.7
5.63	8.91	19.55	378.5	37.1	28.5	21.4
11.25	8.63	20.25	365.4	38.2	29.4	22.1
infinity	8.47	21.41	345.6	38.5	31.1	23.3

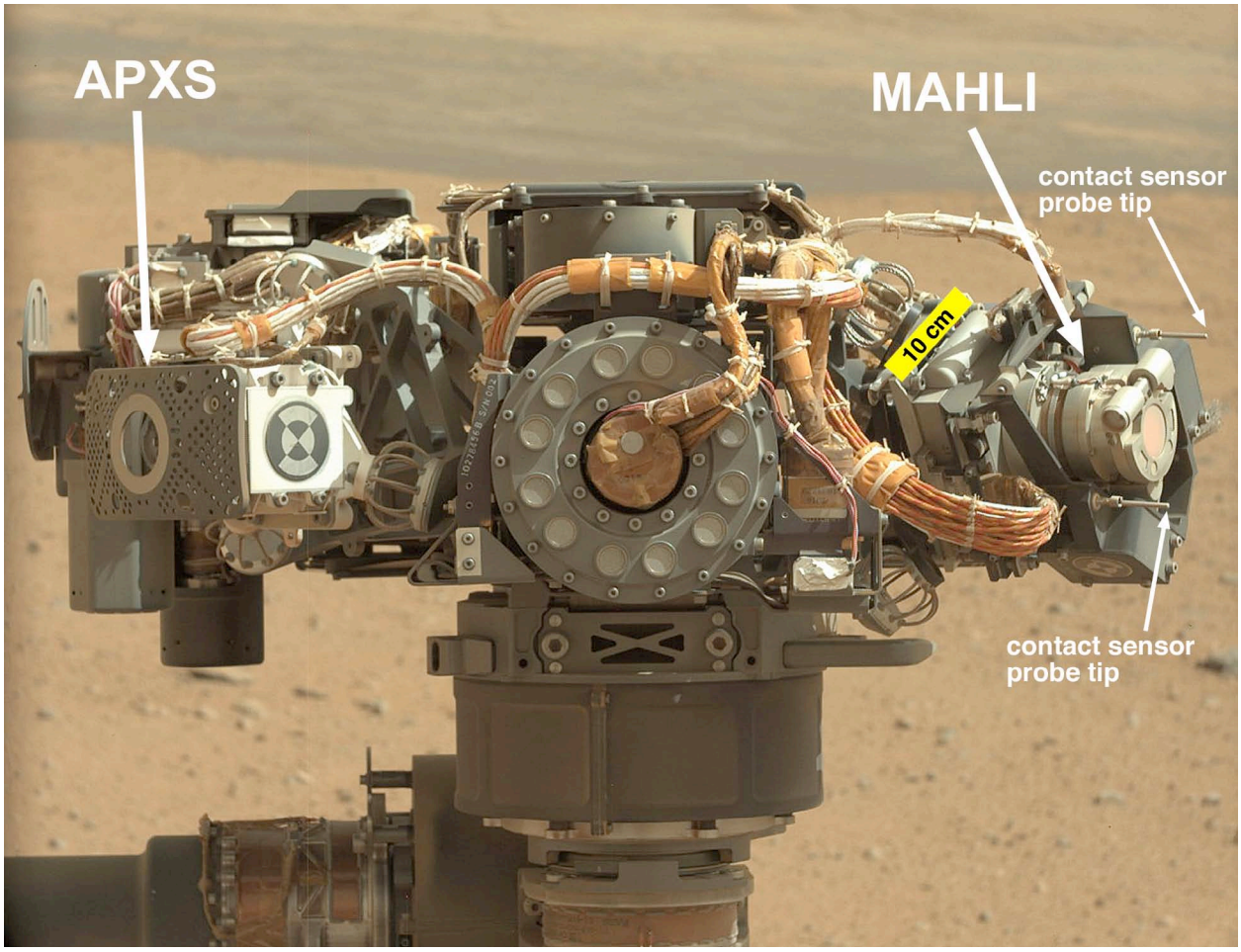

Figure 1. Turret on the end of Curiosity's robotic arm, as viewed by the rover's 34 mm focal length Mastcam on Sol 32 (08 September 2012). The turret carries two science instrument heads, that of the Mars Hand Lens Imager (MAHLI) and the Alpha Particle X-ray Spectrometer (APXS). In addition, attached to the turret are a drill, a brush, a scoop, and a sample handling and processing system (Jandura *et al*., 2010; Anderson *et al*., 2012). This is a sub-frame of Mastcam image 0032ML0000710000100863E02. The yellow bar represents 10 cm at the location it occurs in the figure.

The rover's robotic arm and turret position the MAHLI camera head for imaging (Robinson *et al*., 2013a) and the camera head is protected from collision with solid surfaces by two probes connected to switches that serve as contact sensors to stop robotic arm motion, if necessary (**Figure 1**). MAHLI image mosaics and stereopairs are obtained by robotic arm positioning.

3 Approach and timeline

3.1 Data availability

Until the mission ends, new, validated MSL MAHLI images and attendant documentation are archived regularly with the NASA Planetary Data System (PDS) Imaging Node (**http://pds-imaging.jpl.nasa.gov/**). Data in this repository include the images acquired by MAHLI in pre-

launch and interplanetary cruise testing during 2008–2012, as well as data received from Mars. Because MAHLI can store data onboard for weeks, months, and even years, the images are archived on the basis of when they are received on Earth, not when they are acquired on Mars.

Some data relevant to MAHLI characterization, calibration, and performance assessment are provided in the documents that accompany the PDS archive (Malin *et al*., 2013; Caplinger, 2013); other key data are in the **Supplementary Materials** that accompany this article (indexed in **Supplement S00**). All MAHLI image data and all image data acquired by other MSL cameras that were specifically used for analysis in this report are archived with the NASA PDS.

3.2 Conventions and definitions

3.2.1 Time

As noted, this report covers data acquired and analyses performed through February 2015. All calendar dates given herein are UTC. A *sol* is Martian day and has a duration of ~1.027 Earth days. Because it landed during local afternoon, the sol that Curiosity arrived on Mars was designated Sol 0 and the first full sol after landing was called Sol 1. The Primary Surface Mission was planned to last one Mars year, 669 sols, ending on 24 June 2014. However, the official Primary Mission end, based on NASA funding cycles, was Sol 763, 28 September 2014, as reflected in the MISSION_PHASE_NAME label in MAHLI archival products. Data acquired after Sol 763 were obtained during the MSL Extended Surface Mission.

3.2.2 MSL science and engineering tools and instruments

Grotzinger *et al.* (2012) summarized the suite of instruments and tools aboard Curiosity. Among these are the four cameras built by Malin Space Science Systems (MSSS) that share common electronics designs and onboard data processing capabilities: the 34 mm fixed focal length, focusable Mast Camera (Mastcam-34), the 100 mm fixed focal length, focusable Mast Camera (Mastcam-100), the Mars Descent Imager (MARDI), and MAHLI. In addition, we mention the following in this report: the robotic arm and turret, wheels (mobility system), drill, scoop, dust removal tool (brush; DRT), navigation cameras (Navcams), hazard cameras (Hazcams), Alpha Particle X-ray Spectrometer (APXS), x-ray diffractometer (CheMin), the rover's environment and meteorology experiment (REMS), the chemistry camera (ChemCam) with its laser-induced breakdown spectrometer (LIBS), the Dynamic Albedo of Neutrons (DAN) instrument, and the CHIMRA (Collection and Handling for Interior Martian Rock Analysis) sample processing and handling subsystem.

3.2.3 Distance and range

Working distance is a photography term that refers to the range between the front lens element of a camera and the subject imaged. MSL engineers use the term *toolframe distance*; in MSL literature and discussions this is also sometimes called *standoff distance* or *RP distance* (in which RP stands for *rover planner*, the personnel who operate Curiosity's robotic arm and mobility systems). MAHLI toolframe distance is the range between the subject photographed and the Y, Z plane defined by the two MAHLI contact sensor probe tips (**Figure 1**) when they are not in contact with a surface. In the MAHLI toolframe, the X-axis is equivalent to the instrument's optic (*z*) axis; the distance between the Y, Z plane and the subject is +X; the –X-

axis goes from the Y, Z plane into the camera. MAHLI working distance is 1.9 cm greater than the toolframe distance.

Understanding toolframe distance, and the relation to working distance, is important because MAHLI archival data products commonly reference toolframe distance. This information is provided in the image label (.LBL file) RATIONALE_DESC (a description of image acquisition or onboard focus merge product rationale) to inform the data user of the intended range between the camera and a given target.

The term, *range*, when used here in the context of describing a focus merge range map product, refers to the distance between the front lens element and in-focus elements of the imaged subject in a given MAHLI focus merge product. As each MAHLI focus stack is acquired at a fixed working distance, the range denotes the distance between the camera and the relief elements of the target (*i.e.*, subject), as indicated by grayscale pixel values (data number, DN) values in the range map product.

3.2.4 Terms relating to grain size

Grains in the regolith, eolian deposits, sedimentary rocks, or accumulated on rover hardware are referred to here according to the standard Wentworth (1922) sediment classification scheme (*i.e.*, *granules* are 2–4 mm in size, *sand* 62.5 µm – 2 mm, *silt* 3.9–62.5 µm, and *clay*-sized particles are < 3.9 µm across). *Mudstones* are rocks formed largely of clay- and silt-sized particles deposited in a liquid (*e.g.*, water) medium. *Dust* refers to clay- and silt-sized particles that were or are being transported by suspension in air/atmosphere (Pye, 1987). Dust suspended in the Martian atmosphere, in long-term suspension, is typically of the order of < 10 µm and, in most cases, < 2 µm in size (Pollack *et al.*, 1995; Tomasko *et al.*, 1999).

3.2.5 Image identification

The images mentioned in this report are indicated by their NASA PDS archival identifiers (ID). Mention of a range of image IDs, such as CAL_MH0809500160000493B00 – CAL_MH0809500290000506B00, implies an all-inclusive series of consecutively acquired images starting with image CAL_MH0809500160000493B00 and ending with image CAL_MH0809500290000506B00; in this example, the PDS archives show that there are 14 images in the series. Note that **Supplement S01** describes the pre-launch and interplanetary cruise tests as a function of acquisition date and image ID.

3.2.6 Parent and child images

Every MAHLI image has a *parent image*, the picture originally commanded to be acquired. Upon command, the parent image can spawn children (each a *child image*) onboard the instrument. Examples of children include thumbnail images (reduced-size versions of the parent, approximately 1/8th in terms of pixel dimensions), focus merge products, and any version of the image that is compressed differently than the parent (Edgett *et al.*, 2012). While a parent can be an image that was compressed during image acquisition, our best practice since landing on Mars has been to acquire and store (onboard the instrument) most MAHLI images in uncompressed 8-bit form. An uncompressed 8-bit parent image can be commanded for compression some time after acquisition and storage, whereas a parent that was compressed at the time of acquisition cannot be further compressed onboard the instrument. When a parent is stored onboard in uncompressed form, it can be used to create multiple versions of the image,

each time with a different compression scheme, for downlink to Earth. Thus, if the image received is over-compressed, we have the option to retrieve it again (as many times as necessary) in a less compressed form. Indeed, the majority of MAHLI images received from Mars have been losslessly compressed children of an uncompressed, 8-bit parent.

3.2.7 Color interpolation

The Bayer pattern color interpolation (also known as demosaicking) applied to MAHLI and Mastcam images discussed in this report was performed using the Malvar *et al*. (2004)-based algorithm included in the software onboard these instruments (Edgett *et al*., 2012). This is true whether the image was demosaicked onboard the instrument or on Earth.

3.2.8 Compand and decompand

Compand is a contraction of the terms, *compress* and *expand*. Upon acquisition, MAHLI images are in 12-bit form. They are nominally converted onboard the instrument to 8-bit products using a selected companding scheme. *Decompanding*, usually performed on Earth, restores the image to 12-bit form (typically stored as a 16-bit product). There are 33 MAHLI compand/decompand options; these are expressed as lookup tables that are permanently archived with the NASA PDS in Appendix B of the MSL Mastcam, MAHLI, and MARDI software interface specification document (Malin *et al*., 2013).

3.3 Instrument characterization and calibration approach

The MAHLI team pursued a prioritized approach to instrument characterization and calibration because performing these activities was and remains resource-limited. The resources include the interrelated parameters of time (schedule), availability of experienced personnel, and funding. The schedule for pre-launch calibration and characterization was largely dictated by the spacecraft launch date. Schedule after arrival on Mars is a function of resources available (*e.g*., power, mechanism and actuator temperatures, sun/illumination geometry, onboard data storage, data downlink) and the priority of activities planned (*e.g*., science data collection, rover driving) for any given sol.

Table 2 captures our calibration and characterization priorities. The first thing to understand about the prioritization is that the instrument on Mars performs as intended and that, following Bayer Pattern color interpolation, the science content and utility of the data are rich without performing additional image processing or calibration. **Figure 2** shows an example of an unprocessed (other than color interpolation) MAHLI image, acquired on Mars, for which the geological and surface operations information content is readily apparent. Our highest priority was to determine the scale of and range to in-focus features in MAHLI images. The next priority was to ensure that the images would not be blurred by motion of the robotic arm during image acquisition, and to understand the duration of motion damping after arm placement of the camera. With a focus on grain-scale geologic textures and structures, the investigation was not intended to provide quantitative measures of color (*i.e*., radiometry and spectroscopy) nor micro-relief (*i.e*., stereo photogrammetry). Thus, geometric and radiometric characterization, as well as LED performance characterization, were of a lower priority.

Figure 2. Example of an unprocessed MAHLI geologic image. This uncalibrated image is intended to show that much of the science and engineering content of MAHLI images are accessible without calibration or image processing or enhancement. The only alteration shown here, relative to the parent image, was to perform the same Bayer Pattern color interpolation that is available onboard the instrument. The scene shows Curiosity's first shallow test drill hole (created on Sol 180, 07 February 2013) and first full-depth (~6 cm) drill hole (center; created on Sol 182, 09 February 2013) at the John Klein sample extraction site. The holes have a diameter of 1.6 cm. The rock was interpreted to be a lacustrine mudstone (Grotzinger *et al*., 2014). Acquired on Sol 230 (30 March 2013), the scene is illuminated from the left/upper left and it covers an area 11.8 by 15.8 cm. This is MAHLI image 0230MH0001970010102701C00.

Table 2. MAHLI characterization and calibration priorities

Priority	Characterization	Justification	Specific determinations
1	Image range and scale	The most important geologic quantities to be determined from MAHLI images center on knowledge of the size of features observed and resolved.	Optomechanical system characteristics.
			Relation between focus, stepper motor count, working distance, and image scale.
			Image resolution and contrast (MTF).
			Depth of field.
			Onboard focus merge range map utility.
			Scale of features observed in MAHLI images.
2	Camera head positioning and stability	Important that (1) Curiosity's robotic arm can place the MAHLI camera head at desired locations and distances, (2) the images are not blurred by motion during image acquisition, (3) the duration of motion damping after arm placement of the camera head can be minimized so as to maximize time spent acquiring new data.	Pre-launch tests regarding camera motion during image acquisition.
			Motion damping before image acquisition.
			Camera motion during image acquisition as observed on Mars.
			Camera head positioning and repeatability.
			Imaging with incremental turret rotation.
3	Onboard image products	Ensure that MAHLI's onboard data acquisition, compression, product creation functions, and rover transmission of those products to Earth, are fully exercised.	Data compression and color interpolation.
			Product type identification, creation, and receipt on Earth.
			Onboard focus merge product creation and assessment.
4	Geometric	Confirm image distortion is minimal, as designed; maximally, derive a camera model that can be applied to quantitative 3-dimensional product creation.	System geometric calibration and camera model.
5	Image detection	Minimally, geologic image interpretability is enhanced when pixel-to-pixel variations and blemishes can be removed from the images and seams between mosaicked are unnoticeable. Maximally, to relate image DN to radiance.	Detector and system-level image detection.
			Bandpass and spectral throughput.
			System flat field.
			Color adjustment and white balance.
			Scattered and stray light.
6	Onboard illumination source	Determine the spectral output and Mars surface utility of MAHLI's white and ultraviolet LED illumination sources.	White light LEDs.
			Longwave UV LEDs.
			LED illumination relative to detector.
			Operational characterization.

3.4 Timeline

Table 3 describes the period over which the MAHLI flight instrumentation was assembled, tested, and operated on Mars. We acquired the first MAHLI images in mid-August 2008. The camera head was then disassembled and reassembled to adjust the positioning of the lens and focal plane assembly for improved infinity focus on 19–20 August 2008. We accidentally deposited some particulates on the CCD during this reassembly (see **Section 8.1.4**), so we disassembled the camera head, cleaned the CCD, and reassembled it on 25–26 August 2008. This was the final camera head integration. Thus, only data acquired from 26 August 2008, onward, can be used to characterize and calibrate the instrument.

Table 3. MAHLI characterization and calibration tests timeline

dates (UTC)	Sol	period	key events and tests
15–26 August 2008	—	Camera development	Camera head integration and performance testing at Malin Space Science Systems (MSSS), San Diego, California, USA.
3 September 2008	—		Camera head random vibration testing at Cubic Defense Systems, San Diego, California, USA.
6–11 September 2008	—	Thermal vacuum testing	Camera head and DEA thermal vacuum testing at Cubic Defense Systems.
15–25 September 2008	—	Calibration and characterization	Standalone camera calibration and characterization measurements at MSSS.
9–16 October 2008	—	Camera delivery	Camera head delivery from MSSS to JPL-Caltech in Pasadena, California, USA. (The DEA and calibration target were delivered in March 2010).
October 2008 – October 2010	—	Storage	Camera head in storage at JPL-Caltech. DEA and calibration target delivered to JPL-Caltech in March 2010.
5–10 November 2010	—	ATLO, Assembly, Test, and Launch Operations	First integration of MAHLI camera head, DEA, and calibration target with Curiosity rover; first functional testing. At JPL-Caltech.
13 November 2010			First MAHLI functional testing onboard rover.
17–18 November 2010			MAHLI imaging at robotic arm teach points.
24–30 November 2010			MAHLI imaging during rover system testing.
2 December 2010			MAHLI imaging at robotic arm teach points and robotic arm positioning and stability tests in support of MAHLI.
3–7 December 2010			Rover camera geometric calibration, including MAHLI.
3 February 2011			MAHLI imaging during rover system testing.
February 2011			Rover vibration testing, including before and after MAHLI imaging.
3–23 March 2011			Rover system thermal test (Novak *et al*., 2012), including MAHLI imaging and diagnostic tests.
1 April 2011			Rover electromagnetic interference and compatibility (EMI/EMC) testing, including MAHLI imaging and diagnostic tests.
17 and 27 May 2011			MAHLI flight software update and functional testing.
25–26 May 2011			Rover testing with MAHLI support imaging.
June 2011			Rover shipped to NASA Kennedy Space Center, Florida, USA.
28–30 July 2011			MAHLI imaging in support of rover system test and robotic arm teach point testing.
13 August 2011			Final instrument optics cleaning, at NASA Kennedy Space Center.
26 November 2011			Launch from Cape Canaveral, Florida, USA.
12 March 2012 20 April 2012 14 June 2012	—	Interplanetary cruise	Three periods of instrument check-out during interplanetary cruise.
6 August 2012	0	Primary surface mission	Landing in Gale crater, Mars.
7 August 2012	1		First MAHLI images acquired on Mars.
9 September 2012	33		First MAHLI dust cover opening on Mars; dust cover open/closed imaging.
10–13 September 2012	34–37		MAHLI Calibration Target imaging; robotic arm teach point tests.
22–23 September 2012	46–47		MAHLI participation in robotic arm repeatability test at rock, Jake Matijevic.
2 November 2012	86		MAHLI sky flat field imaging, including with dust cover closed.
22 January 2013	165		MAHLI Calibration Target imaging (night with white, UV LEDs).
4 February 2013	177		MAHLI wheel imaging focus characterization.
6 February 2013	179		MAHLI Calibration Target imaging & focus performance testing.
14 May 2013	274		MAHLI infinity focus test imaging.
3 July 2013	322		MAHLI Calibration Target, sky flat field, turret rotation imaging.
2 October 2013	411		MAHLI Calibration Target imaging.
4 December 2013	472		MAHLI wheel imaging motion damping characterization.
18 January 2014	516		MAHLI sky flat field imaging.
16 February 2014	544		MAHLI imaging of Mastcam Calibration Target.
5 April 2014	591		MAHLI Calibration Target imaging.
8 June 2014	653		MAHLI sky flat field imaging.
2 August 2014	707		MAHLI imaging of Mastcam Calibration Target.
28 September 2014	763		End of Primary surface mission.
29 September 2014	764	Extended surface mission	Start of Extended surface mission.
14 November 2014	808		stereo imaging of REMS UV Sensor for MAHLI stereo characterization.
1 December 2014	825		MAHLI Calibration Target imaging.
5 December 2014	828		MAHLI sky flat field imaging.
30 December 2014	853		Onboard focus merge options characterization.
22 February 2015	905		Dust cover open/closed autofocus test.

We performed instrument standalone testing in September 2008. This work included random vibration testing (to simulate launch), thermal vacuum testing (thermal cycling and operation validation; dark current assessment), and calibration and characterization testing. During this time, the MAHLI flight calibration target was unavailable (it was still being designed), the instrument's autofocus capability was not available until late in the calibration period, and the onboard focus merge capability was also not available.

Following stand-alone testing, we delivered the MAHLI camera head from MSSS in San Diego, California, to the California Institute of Technology's Jet Propulsion Laboratory (JPL-Caltech) in Pasadena, California, on 14 October 2008, to meet a schedule that assumed launch would occur in September–October 2009. In December 2008, NASA decided to delay the launch until the next opportunity, in October–December 2011. The camera head was then stored at JPL-Caltech from October 2008 through October 2010.

After the launch delay, we gave careful consideration as to whether to remove the camera from storage and acquire additional calibration and characterization data. We decided that doing so was not of sufficient value relative to the risk of transporting the instrument back to San Diego and then back, again, to Pasadena; the risk of further transporting the instrument while MSSS moved to a new location in November 2009; and the availability of personnel to perform testing on MAHLI hardware while our highest priority for that period centered on completing and delivering the MSL Mastcam instruments.

Our next opportunity to work with MAHLI came in November 2010 when engineers first integrated the hardware with the rover. Assembly, Test, and Launch Operations (ATLO) occurred at JPL-Caltech during November 2010 through May 2011 and at NASA's Kennedy Space Center in Florida in June through November 2011. ATLO activities that involved MAHLI included system tests under ambient conditions and inside a large environment chamber under Mars-like conditions (Novak *et al*., 2012). Activities also included MAHLI-centric robotic arm positioning, vibration, and motion damping tests; rover camera geometric calibrations; electromagnetic interference and electromagnetic compatibility (EMI/EMC) testing; and robotic arm teach point tests (Robinson *et al*., 2013b). Finally, before the Curiosity was mated with its descent stage and encapsulated in its aeroshell, co-author Ghaemi cleaned and inspected the MAHLI front lens element and dust cover window.

Launch occurred on 26 November 2011. We powered MAHLI on three occasions during interplanetary cruise to confirm post-launch operability and end-to-end commanding and data downlink. The cruise phase testing did not require movement of MAHLI's lens mechanism; we preferred to keep the mechanism in its launch restraint position throughout cruise to ensure that it would be ready for spacecraft entry, descent, and landing (EDL) on Mars.

MAHLI's first Mars data were acquired on Sol 1 (07 August 2012). MAHLI images of the MAHLI calibration target, the Mastcam calibration target, and the sky were acquired throughout the Primary Mission to provide performance and calibration data (**Table 3**). It was vital to acquire these data, even when our analyses lagged behind, to provide periodic monitoring that investigators could assess in the future. As noted above, the Primary Surface Mission ended on 28 September 2014, and the Extended Surface Mission began on 29 September 2014.

3.5 Impact of dust coatings

3.5.1 MAHLI dust cover

We designed MAHLI such that the full range of focus is available whether the transparent dust cover is open or closed. However, the cover became coated with a thin film of dust during landing. MSL's descent engines mobilized dust and sand (Schieber *et al*., 2013; Arvidson *et al*., 2014), some of which was deposited on the Lexan™ dust cover window. We realized that we could not open the dust cover for the first time on Mars without performing a visual inspection to ensure that no grains would obstruct its motion. Thus the first images we obtained—on Sols 1, 10, and 32—were acquired without opening the cover. Before the cover could be opened, we inspected Mastcam images of the camera head taken on Sols 30 and 32 (*e.g*., **Figure 1**) during the robotic arm characterization activity phase described by Robinson *et al.* (2013a). Our inspection revealed no obstruction, so we opened the cover on Sol 33 (**Figure 3**). Nominal imaging, since then, has always been performed with the dust cover open.

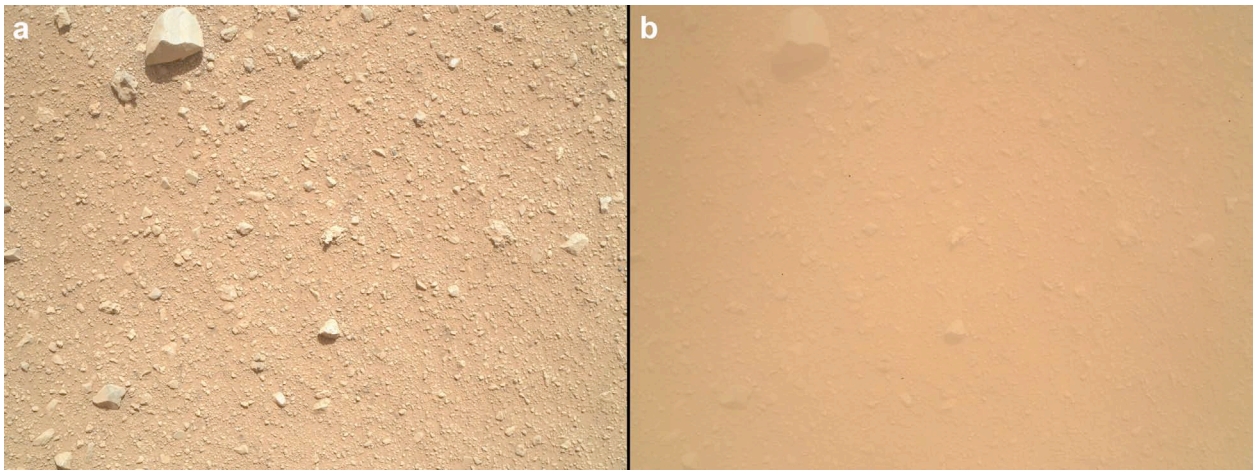

Figure 3. Impact of a thin coating of dust that adhered to the MAHLI dust cover transparent Lexan™ window during terminal descent on 6 August 2012. The presence of this coating removed the option for scientific data acquisition with the cover closed. **(a)** MAHLI image 0033MH0000700000100006C00, acquired with the dust cover open. **(b)** MAHLI image 0033MH0000690000100005E02, showing the same surface with dust cover closed. These images were obtained on Sol 33 (9 September 2012) when the dust cover was opened for the first time. These views look straight down on an 81 by 61 cm surface in front of the rover.

3.5.2 MAHLI calibration target

The MAHLI calibration target (**Figure 4**), along with the subjacent APXS calibration target (Campbell *et al*., 2014), is mounted on the robotic arm shoulder azimuth actuator. Edgett *et al.* (2012) described the calibration target in detail. It includes a bar target and a U.S. cent to monitor resolution and focus motor count performance; red, green, blue, 40% and 60% gray targets—spare material from the Mars Exploration Rover Pancam calibration targets characterized by Bell *et al.* (2003, 2006)—to monitor color performance; a longwave UV fluorescent target to confirm UV LED function; and a series of machined steps, 1 mm wide by 0.3 mm high, for micro-relief calibration.

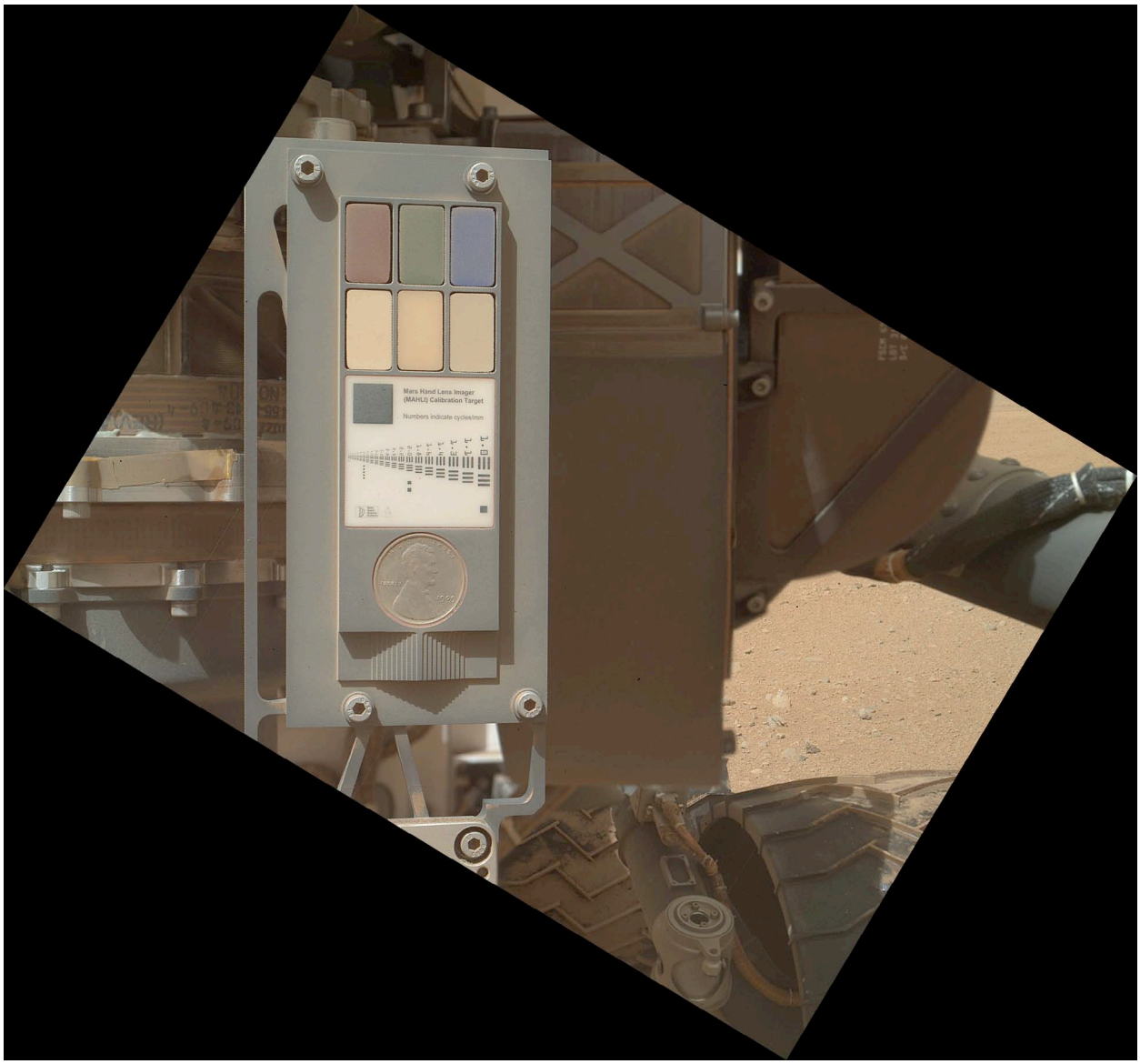

Figure 4. MAHLI calibration target mounted on Curiosity's robotic arm shoulder azimuth actuator, as seen on Sol 34 (10 September 2012). This is a composite of MAHLI image 0034MH0000470010100043C00, focused on the calibration target, and 0034MH0000470040100046E01, focused at infinity for a view of the Martian surface on the right side of the scene. The left front and middle wheels are also in view. For scale, the U.S. cent diameter is 19 mm.

The target is mounted vertically (**Figure 4**) to minimize accumulation of dust that can settle from aerial suspension. Unlike the Mastcam calibration target, which uses circular "sweep" magnets to reduce dust accumulation on color and gray swatch surfaces (Kinch *et al*., 2013), the MAHLI target contains no magnets because these could potentially interfere with Hall Effect sensors in the MAHLI camera head.

Like the MAHLI camera head, the calibration target was coated with dust during the rover's terminal descent on Sol 0 (see images 0034MH0000440010100031C00 and 0034MH0000450010100035C00). Coating of the calibration target by sediment mobilized by the descent engines was not unexpected, based on modeling performed during spacecraft development (Sengupta *et al*., 2009), but the actual nature, volumes, and flight trajectories of

materials mobilized were dependent on where the landing occurred and how much loose sand, silt, and clay-sized particles would be available for transport at that location.

Despite the vertical mounting, the calibration target also accumulated additional dust and sand-sized aggregates of dust throughout the primary mission. Some of these were removed—perhaps by wind or a change in electrostatic conditions—between Sol 591 and 825 (*e.g.*, compare images 0591MH0003710010203133C00 and 0825MH0003710010301615C00).

We designed the calibration target to take to Mars more capability than we might need. The accumulation of dust has not impeded its primary function to monitor drift (if it should occur) in the relationship between focus and working distance. The dust also has not to completely obscured nor rendered useless the color, gray, and fluorescent swatch targets, nor does it impede the option to use the stair step target to check 3-dimensional (3D) measurement performance.

To ensure the data have been collected, both for real-time monitoring and future performance and calibration analysis, we endeavor to image the calibration target once every 180 sols. We prefer to image the target in sunlight, but, at times, it has not been possible to avoid shadowing. **Table 4** shows that the interval between daytime observations has actually varied from as little as 89 sols to as much as 234 sols; the period between observations is a function of how the opportunities fit a busy schedule that includes many other strategically- and tactically-planned rover activities.

Table 4. Repeat intervals for MAHLI calibration observations on Mars

observation	intended sols interval	actual Sols data were acquired	actual sols interval
MAHLI Calibration Target	180	34	–
		165 (night only)	not applicable
		179	145 (since Sol 34)
		322	143
		411	89
		591	180
		825	234
Sky flat field imaging	180	86	–
		322	236
		516	194
		653	137
		828	175
Mastcam Calibration Target	no intended interval	544	–
		707	163

4 Image range and scale characterization

Knowledge of the scale of features observed in a MAHLI close-up image is vital to scientific interpretation. A common practice on Earth is to place an object of known scale in the field of view and photograph it along with the geologic target. For MAHLI aboard Curiosity, this is not possible but hardware can and does sometimes leave markings of known scale that are captured in the images (**Figures 2 and 5**).

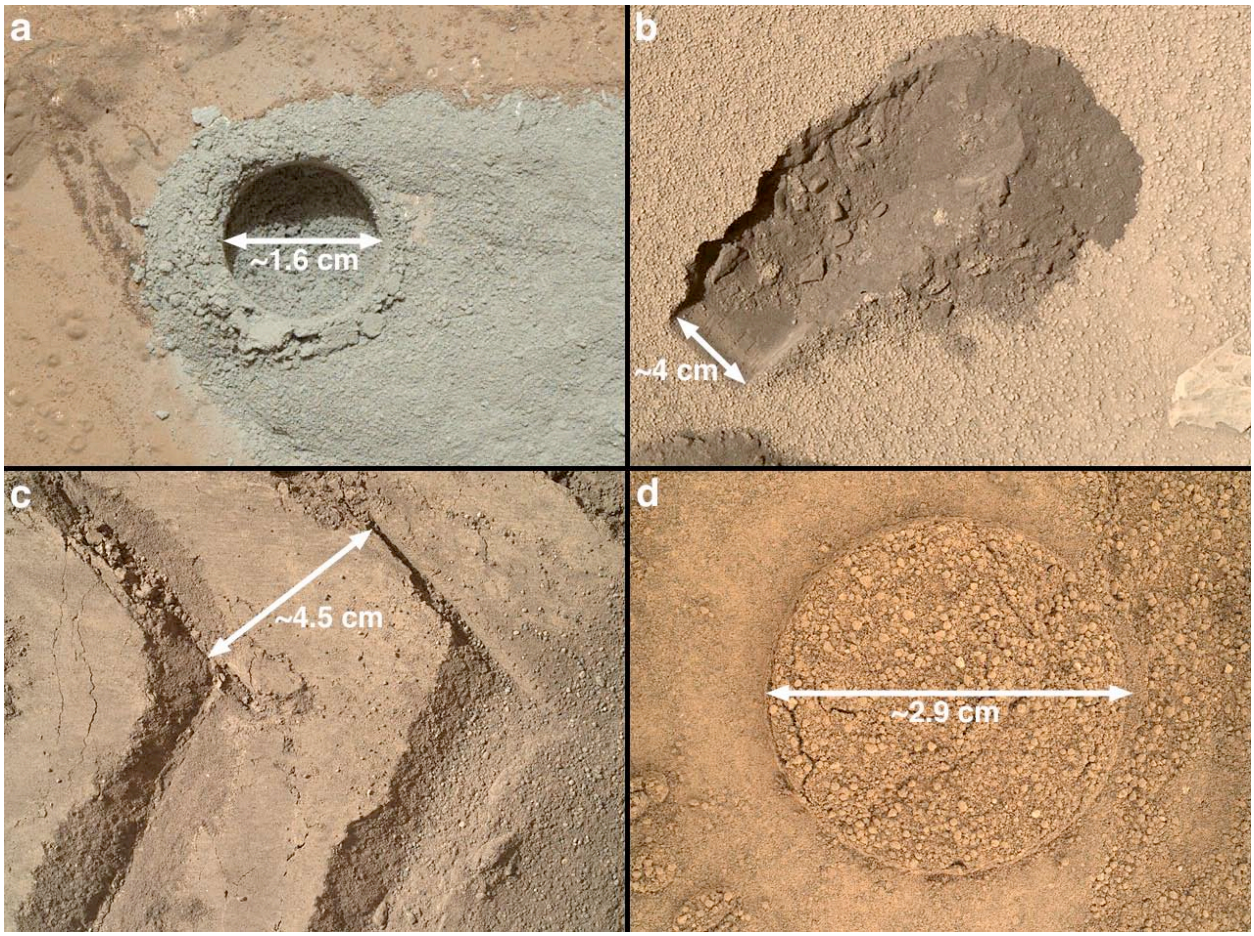

Figure 5. Examples of approximate image scale information provided by rover hardware interaction with geologic materials on Mars. **(a)** Drill hole in rock in a portion of MAHLI image 0180MH0001450010102513C00. **(b)** Scoop sample extraction site in a portion of MAHLI image 0084MH0001120010100946E01. **(c)** Imprints of rover wheel grousers pressed into eolian sediment in MAHLI image 0058MH0000230010100420C00. **(d)** Circular micro-mesa of relatively undisturbed, loose eolian fines surrounded by imprint of the APXS contact sensor plate in MAHLI focus merge product 0802MH0000400000300468R00.

Knowledge of range is also important. MAHLI is sometimes used as a range finder to inform subsequent tool and instrument placement on Mars; Minitti *et al.* (2013) described examples from the Rocknest eolian sand scooping investigation. A combination of knowledge about both range and scale, and sometimes measurements in 3D from stereo, have also been used to inform placement of Curiosity's drill, DRT, and APXS (*e.g.*, Robinson *et al.*, 2013a).

Thus, our highest priority instrument characterization effort was to determine the relationship between focus mechanism stepper motor count and working distance. This, in turn, provides a method to determine the scale of features observed in MAHLI images.

4.1 Optomechanical system characteristics

4.1.1 Stepper motor actions and motor count

A single stepper motor actuates MAHLI dust cover motion and lens focus (DiBiase and Laramee, 2009; Edgett *et al*., 2012). **Figure 6** illustrates the actions that occur over the range between 0 and 16100 steps. At motor count 0, a Hall Effect sensor detects that the mechanism is in its launch restraint position and MAHLI is in a mechanically safe state for rover motion (*e.g*., driving), Mars sample extraction (scooping, drilling) and processing, as well as (before arrival on Mars) launch and landing.

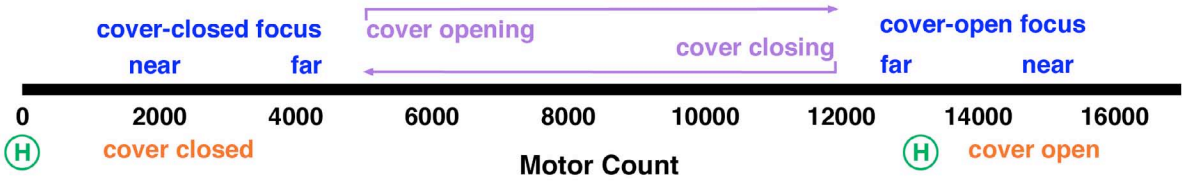

Figure 6. MAHLI mechanism behavior as a function of stepper motor count (*m*). The mechanism launch restraint is at m_{closed} 0. The (H) symbols indicate the location of Hall Effect sensors that confirm mechanical configuration relative to reported motor count.

When in the launch restraint position, the lens is in focus at its minimum working distance and imaging can be performed through the dust cover. When the stepper motor is activated, the motor counts increase or decrease, nominally one increment (one step) at a time. With the dust cover remaining closed, the lens focus group first moves from its minimum working distance focus position to its maximum (in focus at infinity). Then the cover begins to open. When fully open, the camera is again in focus at its minimum working distance. To focus on targets with the cover fully open, the motor steps backward toward the 12000 motor counts position. A Hall Effect sensor located in the middle of the dust cover open focus range confirms the physical position of the lens focus group relative to stepper motor count.

The correspondence between motor count and focus position (which translates into working distance and image scale) is unique to a given MAHLI camera head and requires empirical determination. **Section 4.2** does this for the MAHLI aboard the MSL rover Curiosity; these results are only valid for this MAHLI and only for data acquired after final instrument assembly on 26 August 2008.

4.1.2 Stepper motor count reportage

MAHLI reports the motor count position at which an image is acquired. In the PDS products, this position is called MSL:FOCUS_POSITION_COUNT. For example, a reported motor count (*m*) of 13996 is 13,996 steps from the *m* = 0 launch restraint position. From **Figure 6**, one can see that an image obtained at motor count 13996 is one in which the dust cover was open during acquisition.

During pre-launch testing, we observed that the flight unit MAHLI mid-range Hall Effect sensor is located near *m* = 13320, the dust cover becomes fully open at *m* = 15204, and becomes fully closed at *m* = 1350. We monitor the performance of the stepper motor relative to the actual position of the movable lens focus group using the mid-range and launch restraint Hall Effect sensors. We observed “skipping” on some occasions at very cold temperatures (< –50°C)

during pre-launch testing; this refers to a case in which the focus group detected a Hall sensor at a motor count different from expectation. This problem is avoided at nominal operating temperatures; however, when this occurs, it is possible that the motor count position reported by the instrument does not actually indicate the lens focus position. If we were to detect a case of skipping, then we would report this as errata in the NASA PDS archives. Thus far, no such cases are known to have occurred on Mars.

4.1.3 Dust cover motion

To fully open or close the dust cover, regardless of camera head orientation, takes about 2.5 minutes. We verified this by observation during pre-launch testing. Nominally, we only open the dust cover when the camera is commanded to acquire images in the cover-open state. The number of times the cover is actuated on a given sol depends upon whether MAHLI is being used to acquire cover-open images and the sequence of MAHLI imaging events specific to that sol. Commonly the cover is only opened once per MAHLI imaging sol, regardless of the number of targets imaged, but sometimes the cover is closed and re-opened if another activity occurs between MAHLI image acquisitions (*e.g.*, APXS placement, drilling, scooping, arm configuration change). Through Sol 911 (28 February 2015), the cover performed 604 open/close cycles, 407 of which were for contact science and engineering support, 197 of which were images of the landscape obtained when the robotic arm was stowed.

4.1.4 Lens focus

MAHLI can focus on targets at working distances ≥ ~2 cm with the dust cover open or closed. It can be autofocused or focused manually; it can also acquire focus stacks. Manual focus simply means that the stepper motor moves the lens focus group to a commanded motor count position.

Autofocus is determined by acquiring a commanded number of images (usually 10–30) at different focus positions that bound (with margin) the focus position of the anticipated working distance. This acquisition is followed by quality 80/100 grayscale JPEG compression (Joint Photographic Experts Group; see CCITT (1993)) and rapid, onboard analysis of the resulting compressed file sizes (Edgett *et al.*, 2012). The apex of the parabola fit to JPEG file size versus stepper motor count for the single least compressed image, the preceding image, and the succeeding image, determines the focus position (**Figure 7**). The motor then moves the lens focus group to that position and a focused image is acquired. The images obtained to determine focus via JPEG compression are not retained.

In practice, because targets can have varied relief across the field of view, we usually perform autofocus on a sub-frame of the full 1600 x 1200 pixel scene. Often, although not exclusively, this is a sub-frame of 480 x 480 pixels located at the center of the CCD. This approach ensures that a portion of a full-frame scene is in focus. Following the autofocus sub-frame acquisition, we usually acquire a larger (*e.g.*, full frame) image. This approach is not unlike that which occurs when the user of a consumer digital camera presses the shutter release half way and the photographer sees a box drawn in the scene in the viewfinder that indicates the portion of the field of view for which the camera has found focus. We usually do not downlink the MAHLI autofocus sub-frame, but we do receive their 1/8th-size thumbnail images to provide record that the operation occurred.

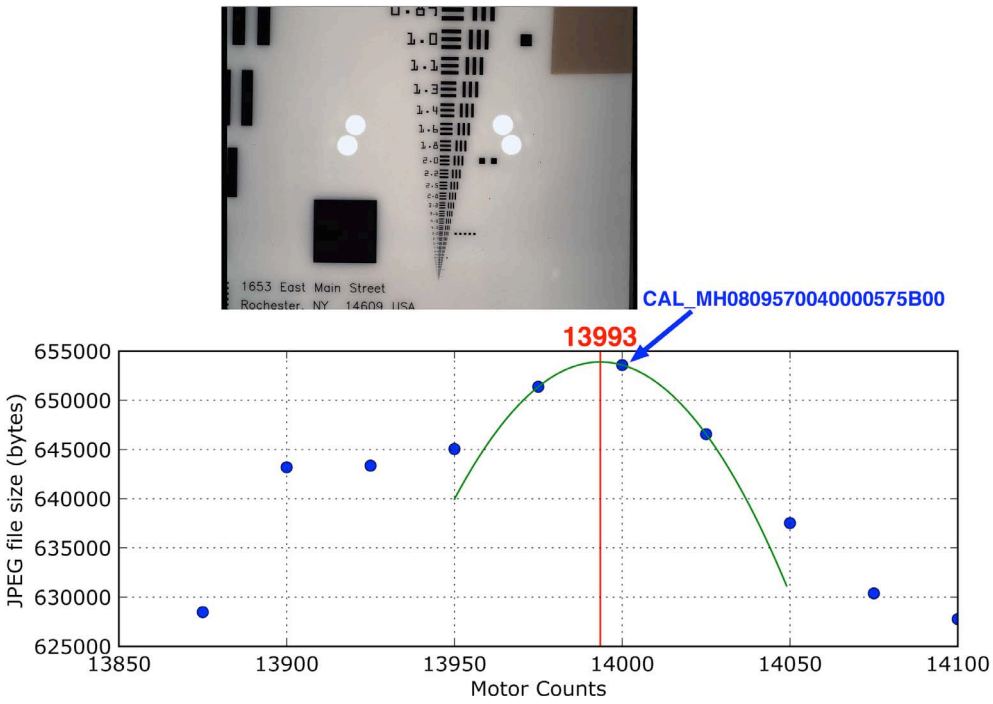

Figure 7. Example of MAHLI autofocus via parabola fit (green curve) to JPEG compressed file sizes as a function of focus position (motor counts). In this case, the 10 blue dots represent the compressed file sizes of MAHLI images CAL_MH0809570000000571B00 (m_{open} 14100) through CAL_MH0809570090000580B00 (m_{open} 13875). These were acquired at a working distance of 7.0 cm and the parabola fit indicates the best focus position is located at m_{open} 13993 (red line and font). The image closest to best focus, CAL_MH0809570040000575B00, is shown for reference; no image was actually obtained at m_{open} 13993 during this 17 September 2008 test.

4.1.5 Stepper motor and focus repeatability

Before launch, we observed that the arrival of the MAHLI stepper motor/lens focus group at the position of the mid-range Hall Effect sensor is repeatable to within ± 6 motor counts. Autofocus was also seen to arrive at a repeatable focus position within ± 6 motor counts as shown, for example, in the Figure 24 of Edgett *et al.* (2012).

4.2 Relation between focus, motor count, working distance and image scale

4.2.1 Pixel scale and image scale

MAHLI CCD pixels are squares of 7.4 µm by 7.4 µm size. Pixel scale is the size of the area on an imaged target that is covered by a single pixel; image scale is the full area of the image (whether 1600 by 1200 pixels or a sub-frame), as projected across the working distance onto a planar target oriented parallel to the CCD. Actual MAHLI targets on Mars are typically not planes, of course, but knowledge of scale as a function of working distance does permit measurement of the in-focus elements in an image. Note that scale is not necessarily equivalent to resolution; the resolution of in-focus elements of a scene is also a function of the camera system's modulation transfer function (MTF; **Section 4.3**).

The MAHLI optics design (Ghaemi, 2009) predicts that the relationship between pixel scale (p in µm per pixel) and working distance (d_w, in centimeters) is:

$$p = 7.687 + 3.4622 d_w. \quad (1)$$

In this relationship, pixel scale is the camera instantaneous field of view (IFOV; CCD pixel size divided by effective focal length) times the working distance plus the object space focal plane position. We have provided example focal lengths, object space focal plane positions, and computed IFOV and pixel scale as a function of working distance in **Supplement S02**.

Before launch, we acquired MAHLI images of targets of known scale (*e.g.*, **Figure 8**) at known working distances of up to 287 cm to empirically determine the relationship between motor count and working distance (**Section 4.2.4**). We also used these images to verify the relation between pixel scale and working distance in **Equation 1**. In each case, we measured the bars and squares on the bar targets in MAHLI images to determine the pixel scale for the image most in focus at each working distance. Edgett *et al.* (2012) found that the following equation provides the best fit to the observations:

~~$p = 6.9001 + 3.4201 d_w.$~~ $p = 6.9001 + 3.5201 d_w.$ *(corrected 5 October 2015)* (2)

Thus, **Equation 2** is the relationship the MAHLI team uses to determine pixel scale from working distance and *vice versa*. **Supplement S03** lists the images and measurements from those images that were used to determine **Equation 2**.

4.2.2 Minimum working distance

MAHLI was designed to acquire in-focus images of targets at working distances from 2.25 cm to infinity (Ghaemi, 2009). To confirm the minimum working distance performance, we positioned a bar target (**Figure 8**) in front of MAHLI and moved it, in 0.03 cm increments, away from the front lens element while the camera was focused at the minimum working distance position (in this case at a dust cover open motor count position, m_{open}, of 16100).

We performed this test three times. However, the second test (CAL_MH0809500160000493B00 – CAL_MH0809500290000506B00) was incomplete and thus we ignored these data. In the first test we acquired 16 images between d_w of 1.88 and 2.26 cm (CAL_MH0809500000000477B00 – CAL_MH0809500150000492B00); in the third test we obtained 26 images between d_w of 1.62 and 2.26 cm (images CAL_MH0809610000000605B00 – CAL_MH0809610250000630B00).

Using the same technique as MAHLI's onboard autofocus software, we JPEG-compressed (quality 99/100) each image from the two successful tests and plotted their file sizes as a function of d_w. Then we fit a parabola to the plotted position of the image with the largest file size and that of the two adjacent file sizes to determine d_w using the parabola vertex. The d_w at the vertex is interpreted this to be the position at which MAHLI would obtain the sharpest image (**Figure 7**). The target working distance was known to within ± 0.025 cm. We found that the minimum working distance at which MAHLI can obtain an in-focus image is at d_w = 2.04 ± 0.025 cm. For simplicity and for margin in planning robotic arm placement of the camera, we operate as if the minimum d_w is 2.1 cm, a value that we communicate to the robotic arm operators as a toolframe +X distance of 0.2 cm; this way, if the camera is slightly closer to the target (< 1 mm), it can still acquire an in-focus image.

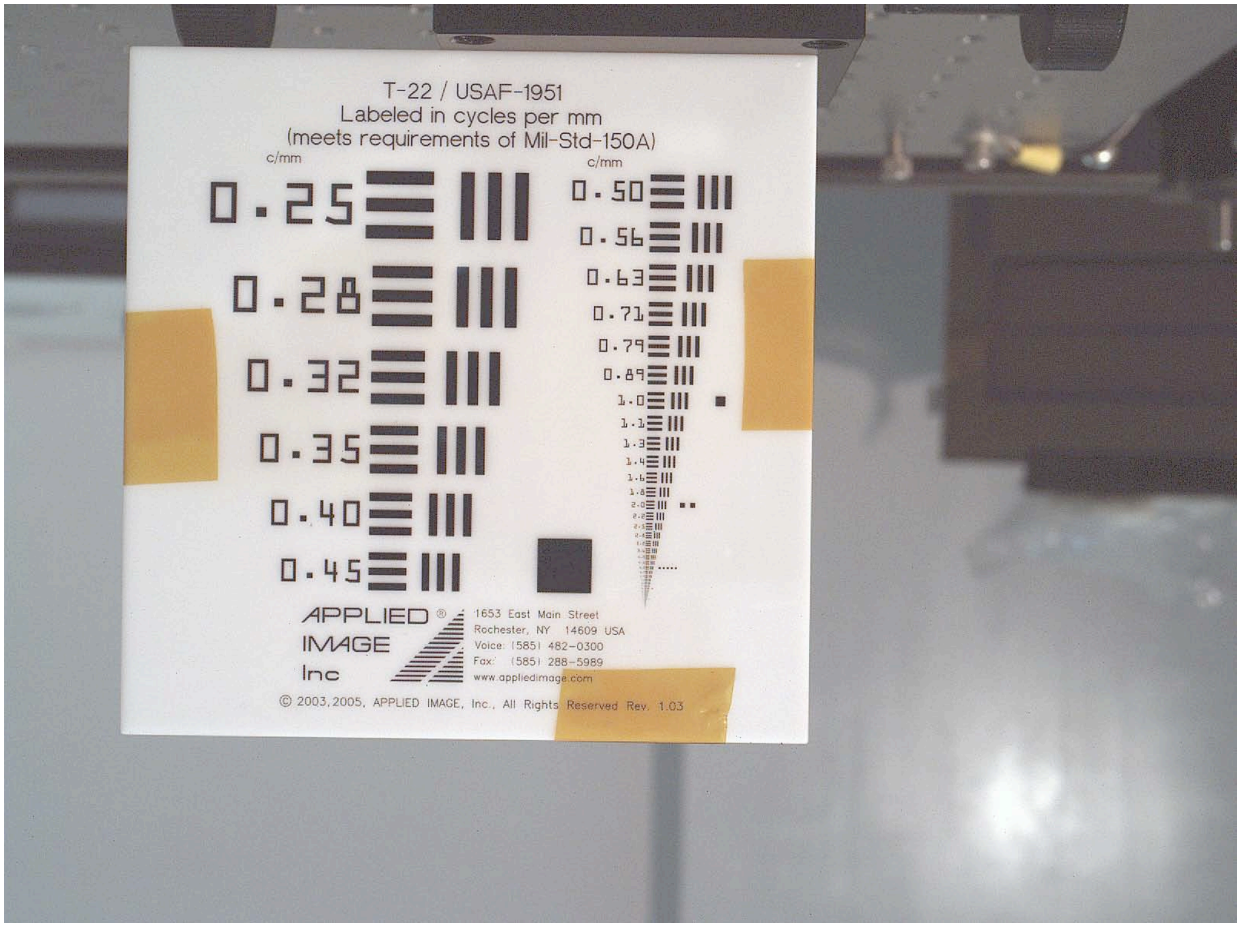

Figure 8. Example MAHLI image of bar target (CAL_MH0809420040000416B00), based on the USAF-1951 target, used for determining range and scale during ground testing in September 2008. In this case, the target was at a working distance of 29.8 cm. Bars are labeled in cycles per millimeter. The target is composed of white opal glass with blue chrome printing.

4.2.3 Dust cover open, infinity focus position

To understand the relation between motor count, working distance, and image scale, it is important not only to understand the minimum image scale and working distance (above), but to also to determine the focus position at the other end of the range, infinity. In this case, we sought a m_{open} that indicates the camera is focused at infinity when the dust cover is open, per nominal Mars surface operations.

We were challenged to determine the infinity m_{open} before launch because of limitations in the size of the clean room facilities in which the camera was tested. Before MAHLI was delivered to JPL-Caltech, the maximum measured distance between the camera and a target of dimensions designed for calibration was about 286 cm. On 18 September 2008, we acquired a total of 73 images of a grid target (at 286 cm d_w) with 2.54 cm spacing using m_{open} in 25 step increments between 12200 and 14000 (images CAL_MH0809660040000743B00 through CAL_MH0809660760000815B00). We cropped these to sub-frames of 1008 pixels (columns) by 688 pixels (rows) with the starting pixel at column 144, row 384 (relative to pixel 0, 0, at the upper left of the CCD), to ensure that only the grid target was in view. Then we JPEG-compressed these images and fit a parabola to the file size, as a function of d_w, based on the

largest file size. This yielded m_{open} = 12562 as the position at which the grid target would be in best focus. The images acquired nearest to m_{open} = 12562, indeed, exhibited the best focus as interpretable to our eyes; these are images CAL_MH08096606100008O0B00 and CAL_MH08096606200008O1B00, at m_{open} = 12575 and 12550, respectively.

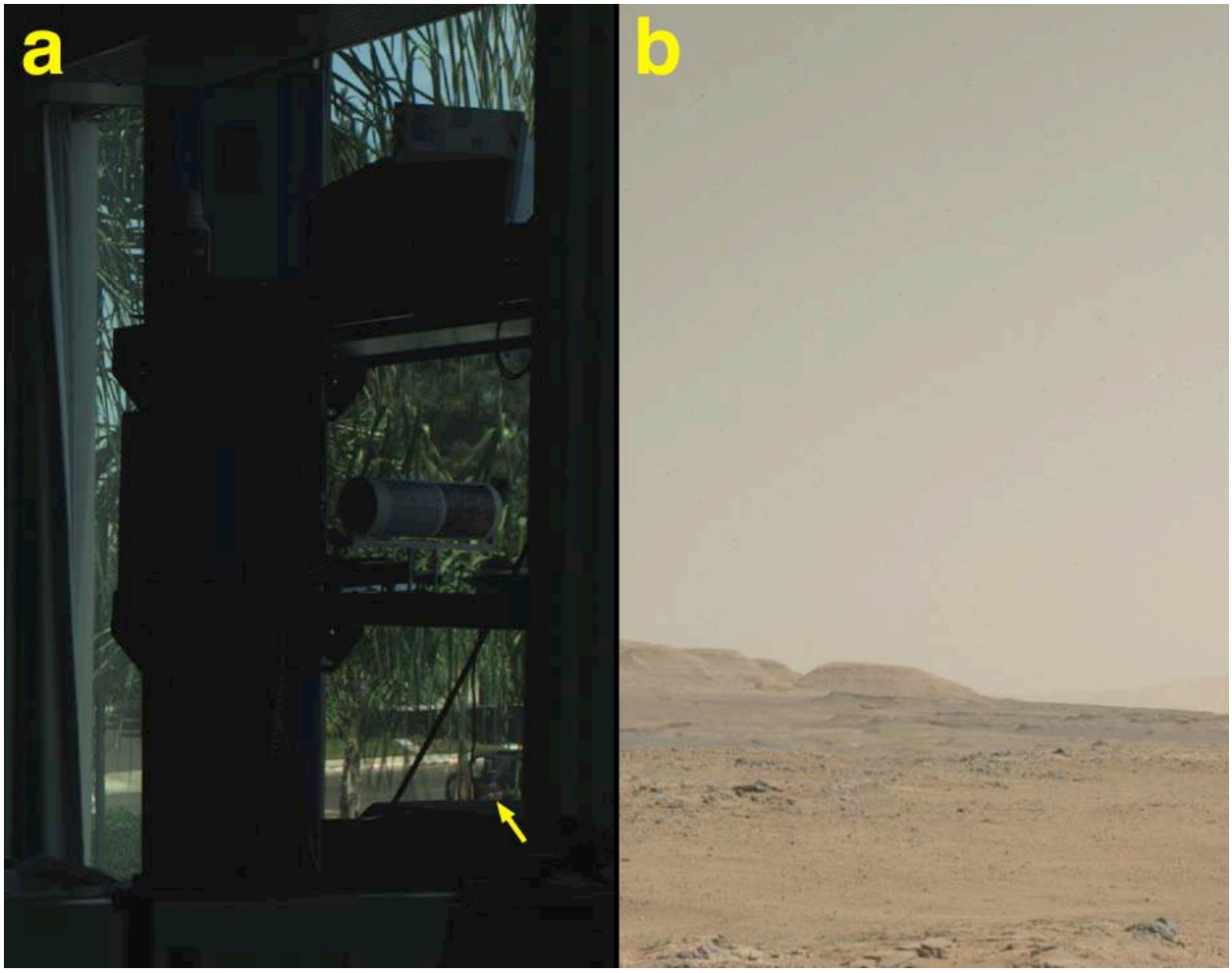

Figure 9. Comparison of colors in natural sunlight in unprocessed (except Bayer color interpolation) MAHLI images acquired on Earth and Mars. **(a)** View of blue sky, green palm fronds, and a vehicle (arrow) as imaged by MAHLI from a clean room through windows on Earth on 19 September 2008; this is a portion of MAHLI image CAL_MH0809780140001207B00. **(b)** View of landscape and sky southwest of the Curiosity rover on Sol 563 (07 March 2014); this is a portion of MAHLI image 0563MH0003250050201792E01.

However, we were unclear as to whether this grid target was a large enough d_w to be considered a determination of the infinity focus position. Therefore, we acquired another group of data before MAHLI was delivered to JPL-Caltech. On 19 September 2008, we pointed the MAHLI camera head such that it had a view from a cleanroom environment through two windows to the outside sky, vegetation, paved surfaces, and a vehicle (**Figure 9a**). Like the grid target images, we obtained a suite of full size images, then we cropped them to cover the portion of the image at greatest distance (features outside the window). The sub-frames (starting column 544, starting row 528; 352 columns by 672 rows) were then JPEG-compressed and we fit a parabola based on the largest file sizes as a function of motor count. The data, images CAL_MH0809780060001199B00 – CAL_MH0809780260001219B00, were acquired between m_{open} = 12250 and 12750 in 25 step increments. We found the best focus position to

occur at m_{open} = 12554. Indeed, our human eye inspection of the features outside the window indicates they are in best focus between m_{open} = 12525 and 12575.

Based on the analysis of the 19 September 2008 MAHLI window images, and because the Aeroflex 10 mm stepper motor count position is only commandable in increments of six counts (steps), the manual focus position we adopted for infinity focus is a m_{open} divisible by six, 12552. During ATLO, we had one more opportunity to explore whether m_{open} 12552 is appropriate for infinity focus. On 27 May 2011, the rover was > 3 m from some of the cleanroom facility features within the MAHLI field of view; we acquired an image (ATL_MH1105060040001333B00) manually focused at 12552, then, moments later, we autofocused on the same scene (ATL_MH1105060050001334B00). The autofocus case yielded a focus position within one motor count (m_{open} = 12551) of the presumed infinity position.

We subsequently explored the infinity motor count position in a test performed on Mars on Sol 274 (14 May 2013). Specifically, with the robotic arm stowed, the we performed three tests which imaged the same landscape at different focus positions: first, we acquired a focus stack of 16 images with m_{open} between 12444 and 12714 at 18 step increments between them (images 0274MH0002550000102936C00 – 0274MH0002550000102951C00); second, we obtained a single view using a full frame autofocus (0274MH0002550010102952C00); and, finally, we acquired a series of sub-frames and corresponding full-frames (images 0274MH0002550020102953C00 – 0274MH0002550130102964C00), with each sub-frame autofocused at a different part of the scene with increasing distance from the rover (**Figure 10**). All three tests were conducted within a 5-minute period, thus reducing the impact of temporally variable illumination or atmospheric conditions.

In all three Sol 274 tests, m_{open} = 12552 emerged as a reasonable position for commanding acquisition of an infinity-focused image. The first test showed best focus at 12552; features were mostly in focus in the image at m_{open} = 12534, as well, but distant features were out of focus in the image at m_{open} = 12570. The second test found focus at m_{open} = 12550, confirming the ATLO (image ATL_MH1105060050001334B00) result at 12551 as well as the general practice of focusing at 12552; indeed, the focus throughout the images obtained at m_{open} 12552 (0274MH0002550000102942C00) and 12550 (0274MH0002550010102952C00) are indistinguishable. The third test (**Figure 10**) showed that surfaces nearest the rover were in better focus at m_{open} 12559 and surfaces farther from the rover were in focus at m_{open} 12545 and even at m_{open} 12526. This latter result suggests that there is range between the 12520s and 12550s over which a landscape scene, such as this, can be in focus; this range likely corresponds with differences in near and far depths of field (**Section 4.4**) at infinity focus.

4.2.4 Dust cover open, motor count relation to working distance

We empirically determined the relation between motor count and working distance for ranges between infinity and the minimum before launch and supplemented this information, where needed, with observations acquired on Mars. We acquired most of the pre-launch data for d_w between 2.1 and 62.3 cm by imaging the bar target shown in **Figure 8**, oriented such that the target surface and CCD surface were plane-parallel. For these data, we determined the motor count position at which the target would be in best focus for a given distance using the JPEG file size parabola fit technique. Targets differing from the one shown in **Figure 8** were imaged at distances near 100, 200, 240, and 287 cm in the laboratory. Further, we supplemented these data with a few additional images obtained during ATLO testing. The images, sub-framing, and JPEG data compression quality used for this analysis are described in **Supplement S04**.

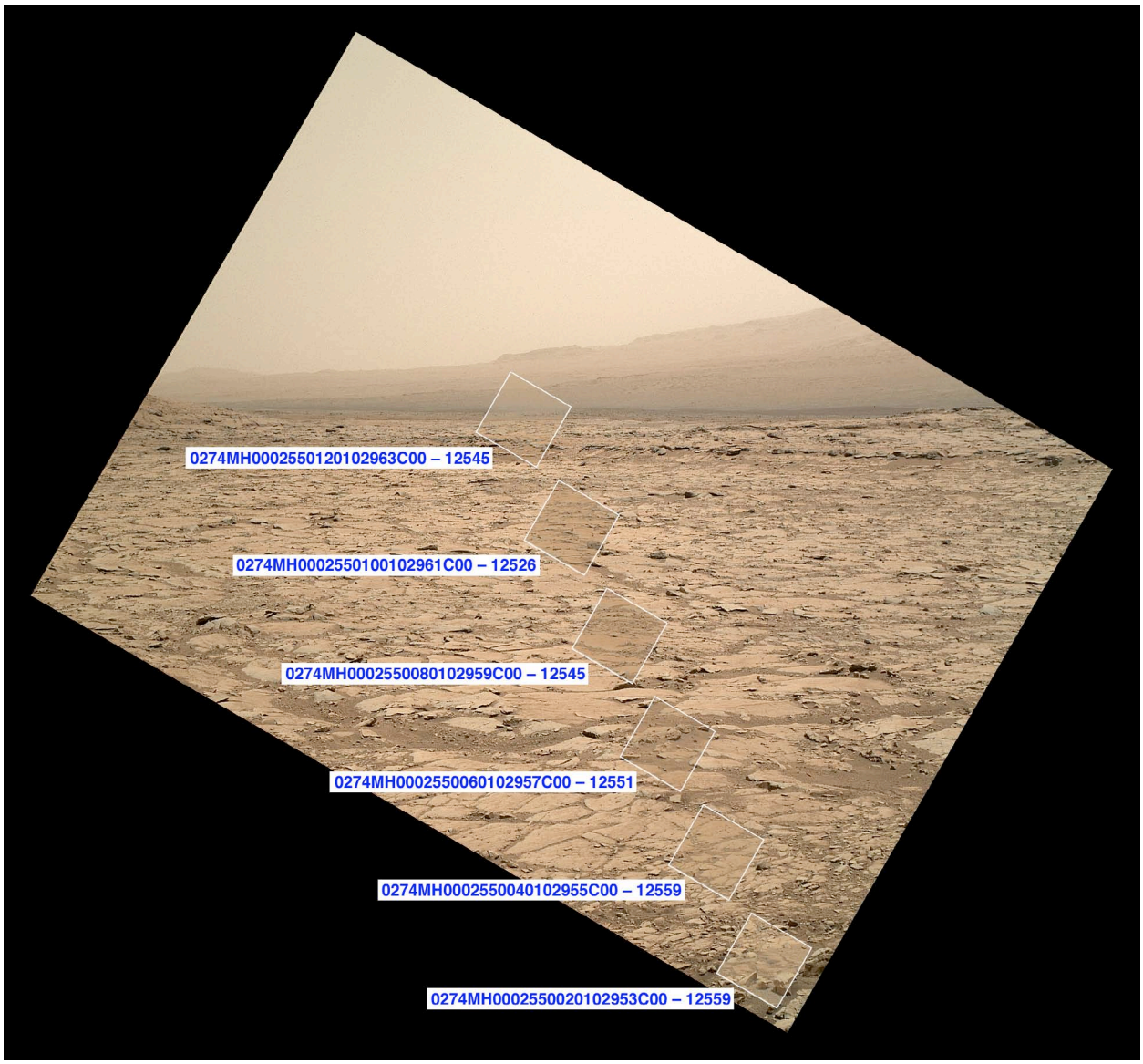

Figure 10. Example of infinity focus test performed on Mars. This illustrates the third of three tests performed within a 5-minute period on Sol 274 in which the robotic arm, turret, and MAHLI were stowed. The MAHLI dust cover was opened and a series of 29 images of the landscape was acquired. In this figure, full frame image 0274MH0002550000102942C00, focused at m_{open} 12552, covers the entire scene. The six insets are autofocus sub-frames designed to focus at increasing distances from the rover. The sub-frame image IDs and m_{open} positions are indicated in blue. When these data were obtained, Curiosity was parked at its Yellowknife Bay field site near the John Klein and Cumberland drill holes; the view is toward the southeast and the northeastern slope of Aeolis Mons (Mt. Sharp) is visible in the background.

The data we obtained before launch were sufficient to determine the relation between d_w and working distance for the dust cover open case (m_{open}) for targets in the 2.04 to ~40 cm range. This is the range that matters most in terms of hand lens scale imaging of geologic materials. However, the pre-launch data in the d_w 40 to 200 cm range were less adequate to understanding the relation to m_{open}; thus we acquired a suite of nested images on Mars on Sol 179 (6 February 2013) to further explore the relationship over this range. Called the MAHLI

distance focus test, the robotic arm positioned the camera above a relatively flat rock surface (which the MSL science team named Fort Confidence) and we acquired a suite of autofocused images, each nested within the previous, from robotic arm standoff positions of 200, 170, 150, 100, 70, 40, 5, and 2 cm (add 1.9 cm for d_w). Because, by this time, the relationship between d_w, m_{open}, and p was well understood for images acquired at $d_w < 40$ cm, the 5 and 2 cm standoff images were obtained to serve as indicators of scale in the lower-resolution images. Effectively, this is like placing a target of known scale (*e.g.*, a ruler or a coin) on the target viewed by the camera. Thus, we used the 5 cm standoff image (0179MH0001220010102490E01) as an indicator of scale to refine our knowledge of d_w for the 200, 170, 150, 100, 70, and 40 cm standoff images (see **Supplement S04**).

As shown in **Figure 11**, the result of combining our pre-launch observations regarding d_w and m_{open}, and our results from the Sol 179 Fort Confidence test, is an equation that describes the empirical relationship between m_{open} and d_w (in centimeters):

$$d_w = (a m_{open}^{-1} + b + c m_{open} + d m_{open}^{2} + e m_{open}^{3})^{-1}, \quad (3)$$

in which $a = 0.576786$, $b = -11.8479$, $c = 2.80153\times10^{-3}$, $d = -2.266488\times10^{-7}$, and $e = 6.26666\times10^{-12}$. **Equation 3** applies only to the MAHLI aboard Curiosity, only when the dust cover is open, and only when the m_{open} is between ~12600 and 15595. We recommend that the equation only be used only for cases in which d_w is in the 2.04 to ~230 cm range. Targets closer or farther from this range cannot be so well determined from motor count; m_{open} from ~15595 to 16100 indicate the minimum working distance of 2.04 cm; m_{open} of ~12600 to 12552 asymptotically approach infinity and thus an uncertainty of 1 motor step yields a large uncertainty in the knowledge of d_w.

4.2.5 Dust cover closed, motor count relation to working distance

We intended to operate MAHLI with its dust cover open. We did not have time to characterize the relationship between d_w and motor count for the dust cover closed case (m_{closed}) before the October 2008 delivery of the camera head. Using the limited suite of dust cover closed images acquired before launch, and adding test cases we acquired on Mars on Sols 33 and 905, we found that m_{closed} for an in-focus image at a given d_w is related to the corresponding m_{open} at the same d_w in the following manner:

$$m_{closed} = 17075 - m_{open}. \quad (4)$$

We determined this relationship by examining the images described in **Supplement S05**. The first of these are two sets of dust cover closed images, acquired before delivery to JPL-Caltech, showing rocks with features of known scale on them (images CAL_MH0809870080001423B00 through CAL_MH0809870140001429B00 and CAL_MH0809890100001453B00 through CAL_MH0809890250001468B00). We also examined pairs of cover open/closed images of the same target, at the same distance, acquired in ATLO and on Mars (images ATL_MH1011020020000023B00 and ATL_MH1011020030000024B00; 0033MH0000690000100005E01, 0033MH0000700000100006C00, and 0033MH0000690000100007E01; 0905MH0004710010302819C00 and 0905MH0001900010302821C00; 0905MH0004710010302855C00 and 0905MH0004240010302857C00). For each, **Equation 4** provides a result within 10 motor counts of the observed cover closed case.

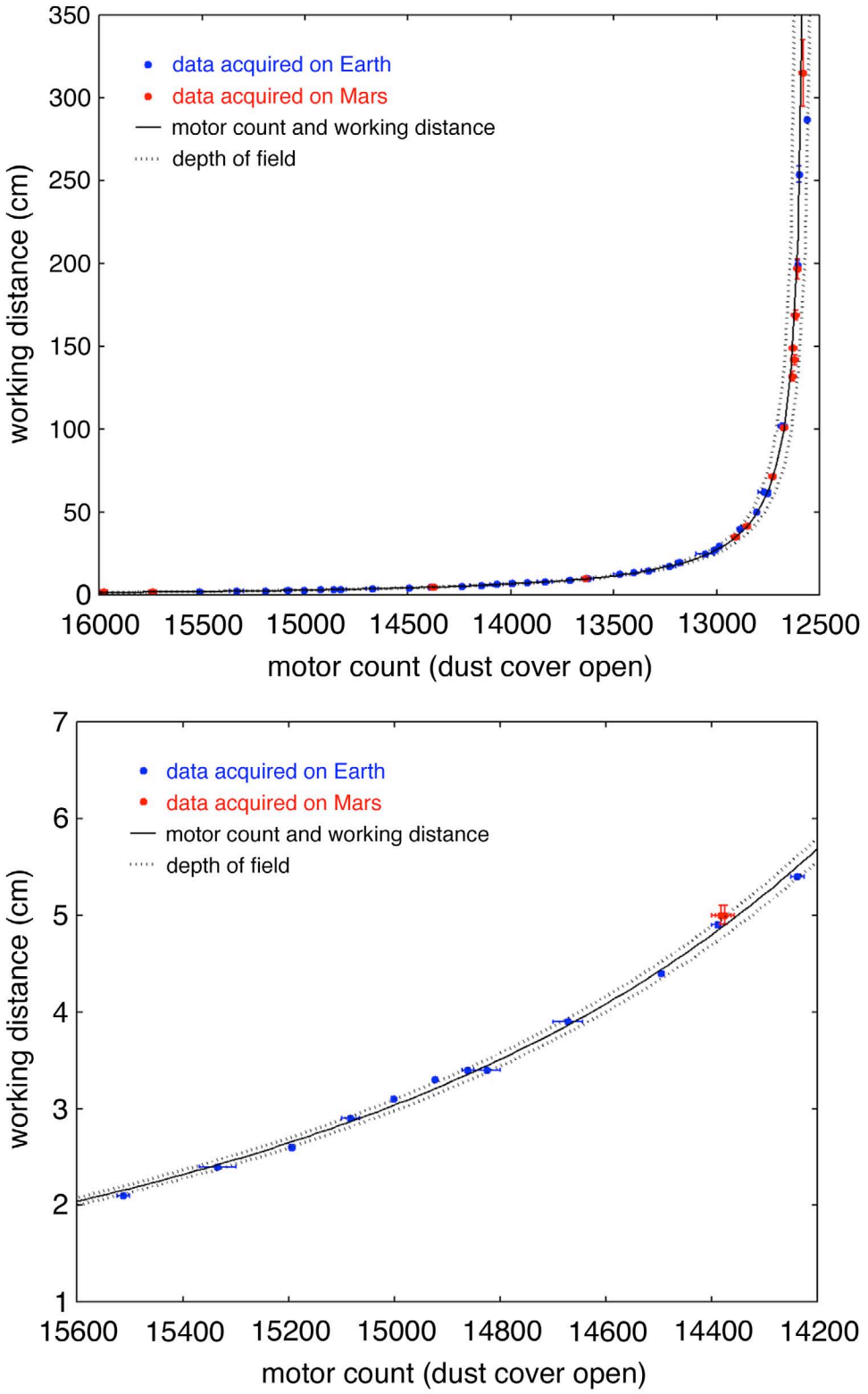

Figure 11. Relationship (**Equation 3**) between working distance, motor count (m_{open}), and depth of field (**Equation 6**). The top plot shows the entire focus range, the one on the bottom shows details over the very highest resolution imaging range. The data acquired on Earth and Mars are listed in **Supplement S04**.

Regarding infinity focus when the dust cover is closed, MAHLI images of a grid target in focus at 275 ± 5 cm working distance in images CAL_MH08098601300014l4B00 and CAL_MH0809870070001422B00 indicate that infinity focus is near m_{closed} 4500 ± 30. Applying **Equation 4** to the m_{open} infinity focus position, 12552, yields a m_{closed} of 4523.

4.3 Image resolution and contrast

Section 4.2 dealt with scale in terms of pixel size as related to the surface area of a target detected by that pixel in an image. Resolution, the smallest extent of an areal feature that can be identified and measured accurately and with certainty, is a related matter. Determination of a camera's modulation transfer function (MTF) provides a measure of resolution and contrast capability. MTF, in turn, can be used to estimate depth of field (DOF; **Section 4.4**). That is, DOF can be referenced to the range, relative to best focus for a given distance, over which the MTF is ≥ 50% of its value at the instrument's Nyquist frequency. Given its 7.4 µm by 7.4 µm square pixels, MAHLI's Nyquist frequency is 68 cycles per millimeter.

4.3.1 Lens MTF

By design, MAHLI polychromatic MTF is optimized at the system Nyquist frequency. We investigated lens MTF during its acceptance testing before integration with the camera body. Ghaemi (2009) described the prescription and the as-built lens MTF performance; MTF at Nyquist was determined on-axis and off-axis via wavefront analysis with the lens focused past infinity. The performance at Nyquist was excellent, with an MTF of 0.5 on the optic axis, 0.4 at +7.42 mm off-axis, and 0.5 at –7.17 mm off-axis.

4.3.2 System MTF

System MTF refers to the contrast and resolution performance of the fully built camera head. We explored various options for determining system MTF using images of the white opal glass bar target in **Figure 8** (MAHLI images DEV_MH0808130030000449B00, CAL_MH0809500000000477B00 through CAL_MH0809500290000506B00, CAL_MH0809790040001224B00 through CAL_MH0809790130001233B00, CAL_MH0809790140001234B00 through CAL_MH0809790220001242B00, CAL_MH0809790230001243B00 through CAL_MH0809790330001253B00, CAL_MH0809790340001254B00 through CAL_MH0809790460001266B00, and CAL_MH0809790470001267B00 through CAL_MH0809790620001282B00), duplicates of this target used in ATLO testing (MAHLI images ATL_MH10120100100000160J00, ATL_MH1012010040000170B00, and ATL_MH1012010070000181J00), and the similar bar target element on the flight MAHLI Calibration Target (**Figures 4 and 12**).

However, these images of opal glass bar targets were less than ideal for MTF determination. The dark targets were printed with blue chrome and the edge of the printed matter is raised relative to the glass surface. Factors that might impact the quality of MTF measurements made using the opal glass bar targets include non-uniform illumination, specular reflection of an illumination source off the target surface, self-shadowing or reflection at the raised edges between blue chrome and white glass, and target orientation. For example, **Figure 12** shows that MAHLI's white light LEDs can highlight, via specular reflection, the miniscule raised relief of the printed blue chrome; this raised relief also impacts the apparent sharpness of the edges observed in MAHLI images.

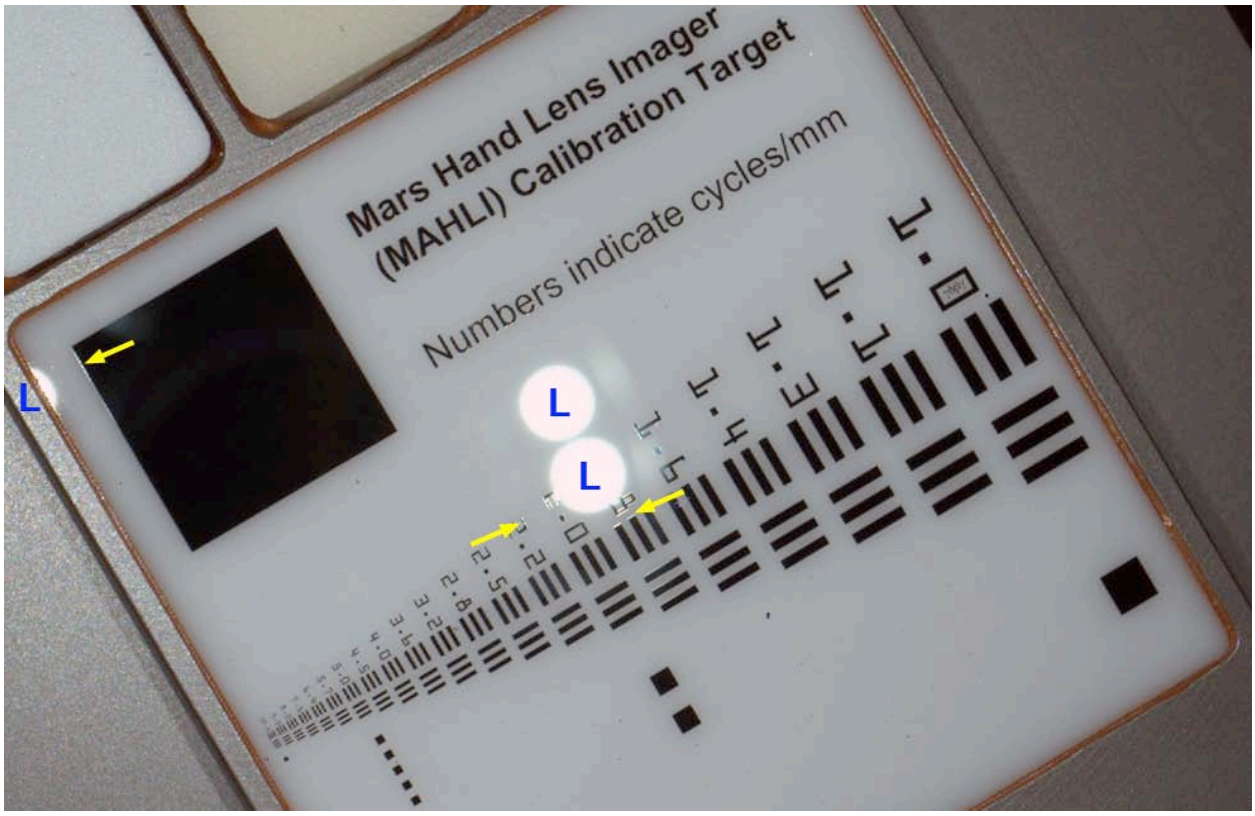

Figure 12. Extreme example of the impact of non-uniform illumination on white opal glass bar targets used for some of the MAHLI calibration and characterization effort (also see **Figure 8**). We determined that this target was not ideal for MTF observations. This figure illustrates specular reflection of MAHLI's white light LEDs (L) off of the opal glass and attendant reflections, including specular reflections at the raised edge between the blue chrome (appearing black in the figure) printing and the white opal glass (yellow arrows). This is a portion of MAHLI image ATL_MH0080050020000561B00, acquired on 14 March 2011, during rover system environment chamber testing. The image shows a portion of the flight MAHLI Calibration Target, mounted on the rover, Curiosity, which was in the darkened chamber at the time.

Another concern regarding determination of system MTF centers on the impact of our use of a Bayer pattern filtered detector and the implementation of a specific color interpolation scheme (**Section 6.1**). Determination of MTF of a Bayer pattern filtered camera system can be described as a research project unto itself (*e.g.*, Yotam *et al.*, 2007).

Our exploration of methods to determine system MTF finally settled upon use of a commercial software package, Imatest Master (version 4.1.6) to investigate slanted edges in a MAHLI image focused on a target near infinity (d_w = ~2.54 m). The Imatest Master tools are based on the approach described by Reichenbach *et al.* (1991) with improvements by Imatest's Peter Burns to implement the ISO 12233 standard. Shown in **Figure 13**, we selected three slanted edge regions of interest (ROIs) for analysis. We examined the image after nominal Bayer pattern color interpolation. The average output MTF for the three ROIs (**Figure 13**), at the camera's Nyquist frequency, is 0.179. This is consistent with our expectation, based the system design and lens performance, that the system MTF performance would be near 0.200 at the Nyquist frequency.

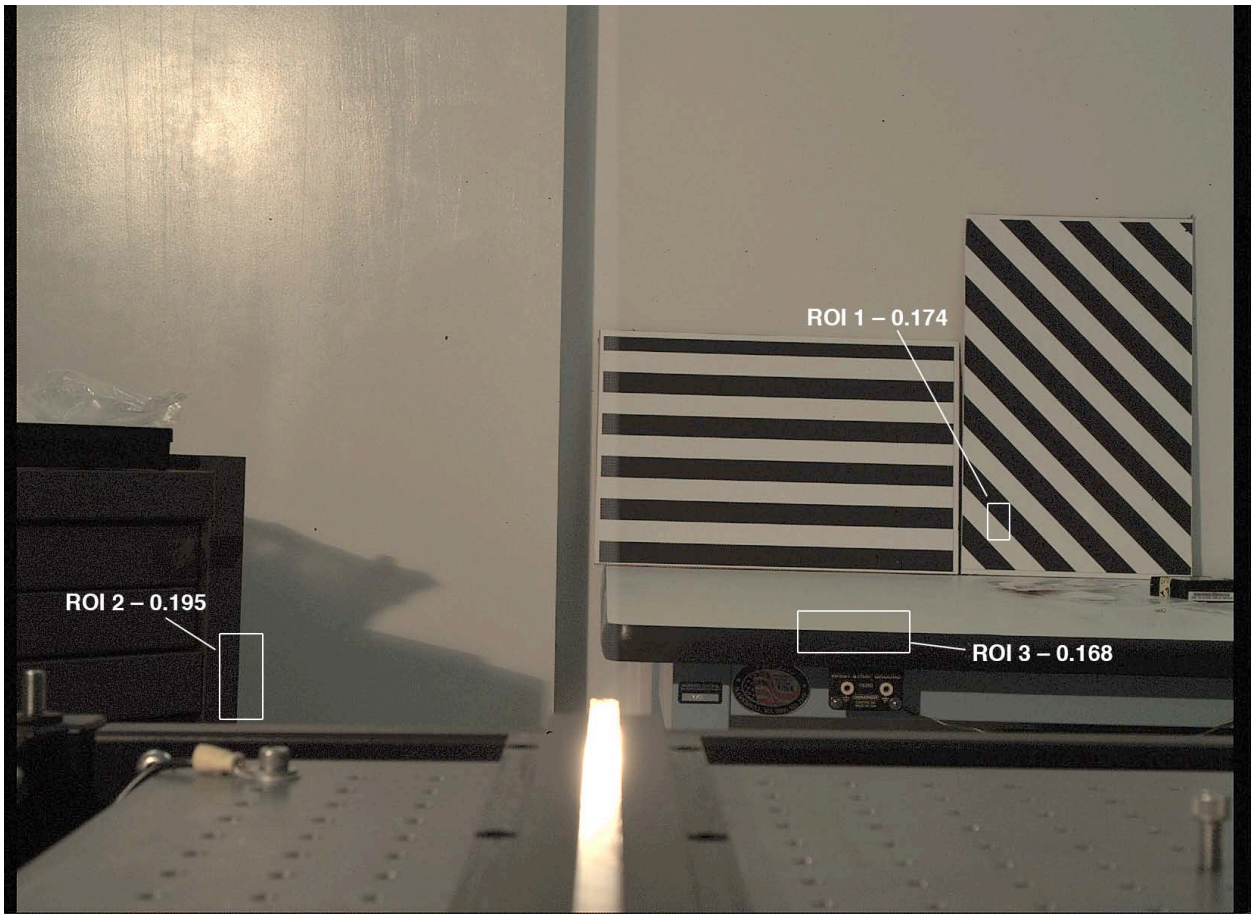

Figure 13. MAHLI calibration image CAL_MH0809480070000463B00, acquired during instrument stand-alone testing at MSSS on 16 September 2008. Following Bayer pattern color interpolation, MTF performance was investigated at the slanted edge targets within the three regions of interest (ROI), illustrated here, using Imatest Master (version 4.1.6). The resulting MTF at the camera's Nyquist frequency (68 cycles per millimeter) for each ROI is shown. Their average yields an estimated system MTF of 0.179 for the flight MAHLI instrument.

4.3.3 Assessment of resolution from Mars data

MAHLI was designed largely to image geologic materials at small working distances. Thus, we assessed that capability using data acquired on Mars. Fortunately, the majority of MAHLI close-up images have been downlinked in lossless compressed form, eliminating the potential impacts of both the onboard Bayer pattern interpolation algorithm and JPEG compression on the ability to resolve fine details.

A critical requirement on MAHLI design was for it to have the ability to resolve grains that distinguish very fine sand from silt. The boundary between these occurs at particles of 62.5 μm size. This boundary is not arbitrary but based on the nature of general fluvial and eolian sedimentary processes—in modest fluvial and eolian conditions on Earth and Mars, sand will largely travel by saltation and silt in suspension. The ability to distinguish bodies of rock formed of sand from those formed of particles smaller than sand (silt- and clay-sized grains) contributes to the ability to distinguish sandstones from loessites and mudstones. For Mars, finding examples of mudstone is of particular interest because of their potential for biosignature preservation (NASA, 1995; Schieber, 2001; Summons *et al*., 2011).

Thus, the ultimate test of MAHLI resolution centers on the ability to distinguish silt- from sand-sized grains in images from Mars. Here we consider two examples: dark grains in a light gray rock brushed by Curiosity's DRT and imaged in full shadow; and fine grains observed in sunlight in the very highest resolution MAHLI image returned during the Primary Mission.

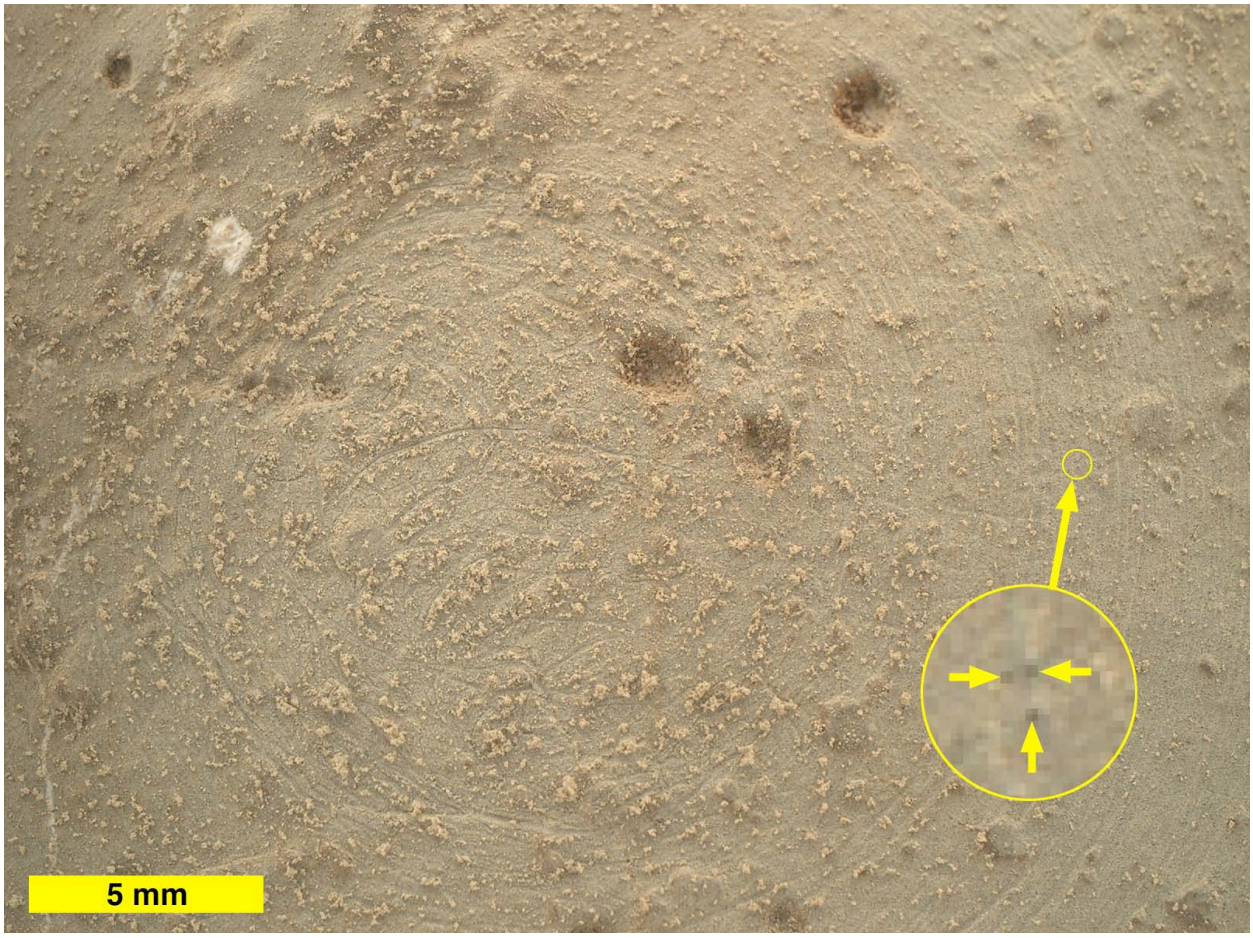

Figure 14. MAHLI view (image 0169MH0002090010102223C00) of an in-place rock surface brushed by Curiosity's DRT on Sol 169 (26 January 2013), shortly after brushing occurred. Clumps of loose dust are present. The target was named Wernecke; the body of rock is the Sheepbed member of the Yellowknife Bay formation (Grotzinger *et al.*, 2014). Although acquired during the day, in sunlight, this 16.6 µm/pixel view was completely shadowed by the robotic arm turret. The inset shows an expanded view of a portion of the brushed rock surface. Three dark gray squares are evident (arrows), indicating grains no larger than ~34 µm in size.

The first example comes from a 16.6 µm/pixel image (0169MH0002090010102223C00) of the surface of a rock. Shown in **Figure 14**, the rock was brushed by the rover's DRT. When viewed in sunlight, we observed that the bare rock is light to medium gray (see image 0169MH0002050010102201C00). The target was completely shadowed by the robotic arm and turret when the high resolution view was acquired (**Figure 14**). The inset in **Figure 14** shows three of many examples of small, dark spots that are part of the rock. In this case, these are 2 by 2 pixels in size. We interpret these and similar dark patches to be silt grains in the rock. Because they are dark gray or black, they stand out relative to the lighter-gray grains that make up the bulk of the rock at this location. Assuming each of these is a grain (a reasonable assumption, given the detection by Vaniman *et al.* (2014) of dark opaque minerals, such as magnetite, in the rock), we infer that each is no larger than ~34 µm. This detection far exceeds our requirement for MAHLI to be able to distinguish very fine sand from silt.

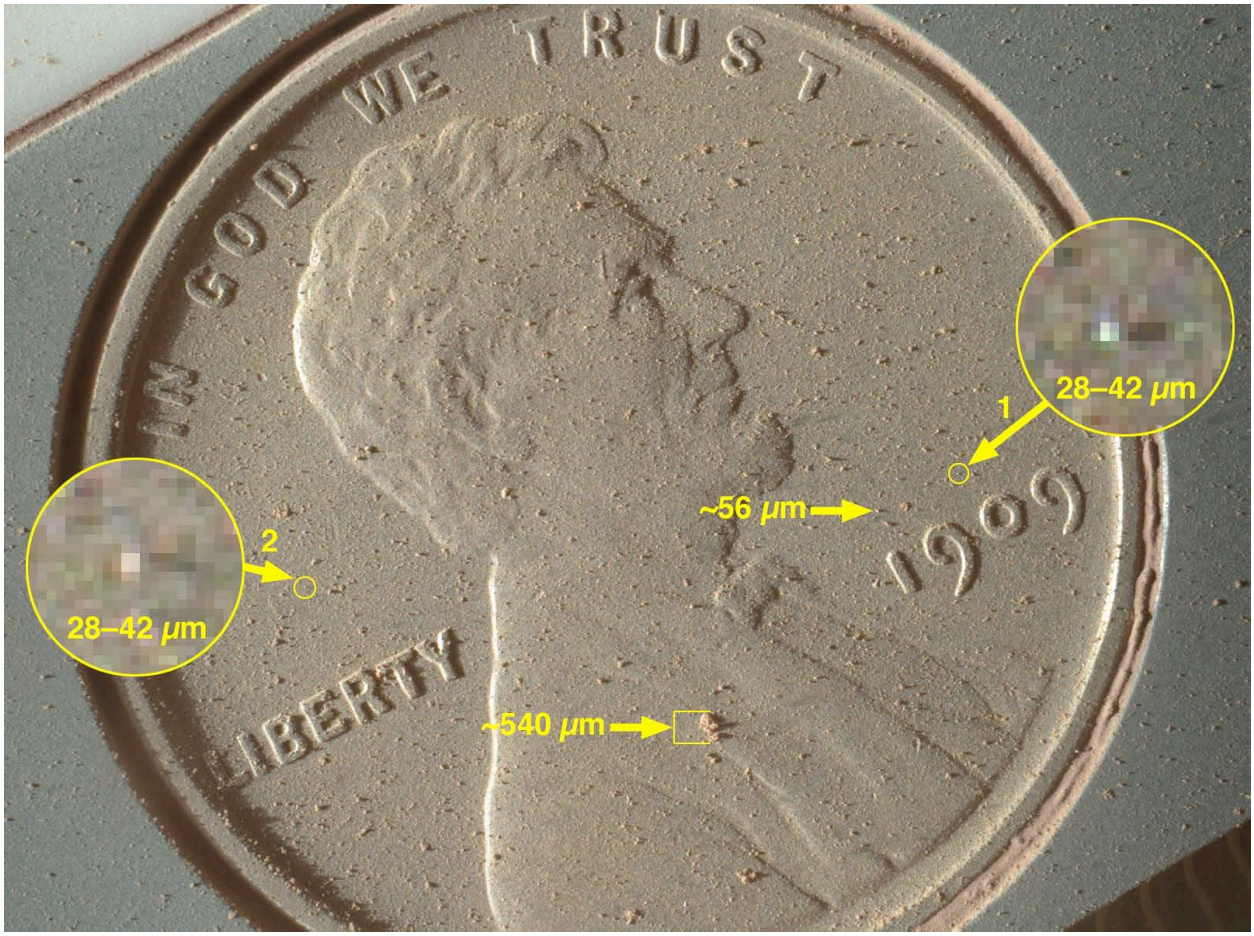

Figure 15. MAHLI 13.9 μm/pixel image of dust and dust aggregates on the U.S. cent on the MAHLI calibration target, as seen on Sol 411 (02 October 2013). Particles smaller than the coarse silt (grain labeled ~56 μm) are evident in this high contrast view. Insets 1 and 2 show individual silt grains of 28–42 μm size; their size was measured both from their 2D pixel coverage and from their shadow length. The solar incidence angle, here, was 71.3°. The cent diameter is 19 mm. This is image 0411MH0003240010200021C00, illuminated by the sun from the left.

The second example comes from examination of the highest resolution image acquired during the Primary Mission, image 0411MH0003240010200021C00. There is less risk to the instrument in having the robotic arm place the camera at the minimum working distance in front of the MAHLI calibration target relative to doing so at geologic surfaces. Thus, on Sol 411, we acquired an image of the dust-coated cent target (**Figure 15**). The solar incidence angle was about 71.3°; this opportunity allowed us to compare our two-dimensional (2D) pixel measurement with a third dimension using shadows cast by the grains. **Figure 15** shows that some grains or grain aggregates were sand-sized (> 62.5 μm), while others were silt-sized (< 62.5 μm). The magnified insets indicate two examples of the smallest grains detectable in **Figure 15**. These grains are no more than 2–3 pixels in size, corresponding to particles of no more than 28–42 μm size. Our shadow measurements yield similar results; the grains protrude no more than 28–38 μm above the cent surface. Like the observations shown in **Figure 14**, the observations in **Figure 15** show that when the d_w is small enough (< ~3.7 cm) and a grain is distinct from its surroundings, MAHLI can indeed provide information about silt-sized grains on Mars. Not only can MAHLI distinguish silt from very fine sand, it can, when positioned close enough to a target, provide constraints on silt particle size.

4.4 Depth of field

Depth of field (DOF) is the distance between the nearest and farthest in-focus feature in a given image. DOF is somewhat subjective, as items that might appear to be in focus to one observer might seem somewhat blurry to another. MAHLI's DOF increases with working distance (Ghaemi, 2009). Knowledge of MAHLI DOF is important for commanding the acquisition of focus stacks, so as to capture the target surface relief seamlessly, without blurred areas between focus-merged images. DOF is also important in accounting for uncertainty in estimating working distance from motor count, particularly when distance and, thus DOF, are large (*e.g.*, 20 cm to infinity). Further, as a matter of MAHLI tactical operations planning, DOF is taken into account when the team has to consider the trade-space between acquisition of focus stack images of a limited number of targets versus imaging a larger number of targets *sans* focus stacks (*i.e.*, for the latter, the camera might image the targets from a greater standoff distance to take advantage of the larger DOF).

As illustrated by Ghaemi (2009), MAHLI depth of field at small working distances (< 12 cm) was defined as the range over which the lens MTF is at > 50% of its peak in-focus value. For targets at greater range (> 12 cm), we estimated DOF using the hyperfocal distance (d_h) equation,

$$d_h = (f_e^2 / f_n\, c_c) + f_e \quad (5)$$

in which f_e is the lens effective focal length, c_c is the circle of confusion, and f_n is the focal ratio (f/number). For MAHLI, f_e and f_n change as a function of focus position (Ghaemi, 2009; Edgett *et al.*, 2012). We assume c_c is a diameter equivalent to two pixel dimensions, (*i.e.*, 14.8 µm at the detector surface); this provides the best match to the 50% MTF fall-off method at 11.25 cm and is consistent with our observations of blurring of near and far objects in MAHLI portraits of the Curiosity rover (*e.g.*, Minitti *et al.*, 2013) acquired on Sols 84, 85, 177, 613, and 868—in those images, we observe two pixels of blur at 1.6 m and two pixels of blur at 14.6 m.

Table 5 lists MAHLI depth of field estimates obtained by these methods. We also incorporated MAHLI DOF estimates into **Figure 11**. When the dust cover is open, the relationship between motor count (m_{open}) and the range, in centimeters, to the near (d_{near}) and far (d_{far}) depth of field, also in centimeters, can be expressed as:

$$d_{near} \text{ or } d_{far} = (a m_{open}^{-1} + b + c m_{open} + d m_{open}^{2} + e m_{open}^{3})^{-1}, \quad (6)$$

in which, for d_{near}, a = 1.03565, b = –11.9083, c = 2.82403×10^{-3}, d = -2.29003×10^{-7}, and e = 6.34332×10^{-12}; and, for d_{far}, a = 1.03438, b = –11.4118, c = 2.69297×10^{-3}, d = -2.17752×10^{-7}, and e = 6.02494×10^{-12}.

During ground testing in September 2008, we acquired 63 MAHLI images to verify knowledge of MAHLI DOF (images CAL_MH0809790000001220B00 – CAL_MH0809790620001282B00). This imaging consisted of five tests in which we incrementally moved a bar target (**Figure 8**), its surface a plane parallel to the MAHLI CCD, away from the camera. In each case, we manually focused MAHLI at a specific m_{open} and held it fixed while moving the target away from the lens such that passed it through the range at which the target would be in focus for that given motor count. Only the last two of these tests, with the camera at m_{open} of 13800 and 13200, acquired more than one image within the range of the depth of field for that focus setting.

Indeed, the latter test had four images within the depth of field (images CAL_MH0809790470001267B00 through CAL_MH0809790620001282B00). At m_{open} 13200,

the camera should be in focus when the target is at a d_w of 18.5 cm. This occurred in image CAL_MH0809790570001277B00; our measurement of features on the target verified that the image scale is 72 µm/pixel and the d_w was 18.5 cm. Visual inspection shows that the next two nearest images (CAL_MH0809790550001275B00 and CAL_MH0809790560001276B00, at d_w of 18.0 and 18.3 cm) were in focus. The next farther images, CAL_MH0809790540001274B00 at 17.8 cm and CAL_MH0809790580001278B00 at 19.3 cm, are just slightly out of focus. Application of **Equation 6** shows that the depth of field should be over the range 17.6–19.4 cm; the slight blurring suggests the DOF estimated from **Equation 6**, in this case, might be generous by about 1–2 mm (d_{near} and d_{far}).

Table 5. MAHLI depth of field estimates over the 2 to 300 cm range

working distance (cm)	depth of field (cm)		effective focal length (mm)	focal ratio (f/number)
	near	far		
2.250	–0.041	0.045	18.39	9.80
2.813	–0.052	0.054	18.69	9.52
3.750	–0.071	0.074	19.06	9.22
5.625	–0.124	0.121	19.55	8.91
11.25	–0.390	0.315	20.25	8.63
20	–1.02	1.13	20.59	8.54
40	–3.96	4.94	20.87	8.50
50	–6.06	8.00	20.93	8.49
100	–21.7	38.4	21.09	8.48
150	–44.0	107	21.16	8.47
200	–71.3	248	21.20	8.47
250	–102	561	21.23	8.47
300	–136	1460	21.25	8.47

4.5 Scale of features observed in MAHLI images

All of the preceding information regarding motor count, working distance, pixel scale and DOF inform the data user of options to determine or estimate the scale of features observed in MAHLI images.

4.5.1 Scale from objects of known size or features at known distance

One way to estimate the scale of features observed in a MAHLI image is to identify an object of known size or located at a known distance. The object can be rover hardware; a landmark at a known distance from the camera; or a rock, regolith surface, or eolian deposit with which rover hardware has interacted. **Figures 5 and 16** and Figure 28 of Edgett *et al*. (2012) show examples. The scale information extractable from interaction of rover hardware with surfaces is approximate, as the interaction does not always form precisely cut or imprinted features. One can determine the distances to landmarks from knowledge of rover position, camera pointing, and identification of landforms observed in both the MAHLI image and in maps made from images and altimetry measurements acquired by orbiting instruments.

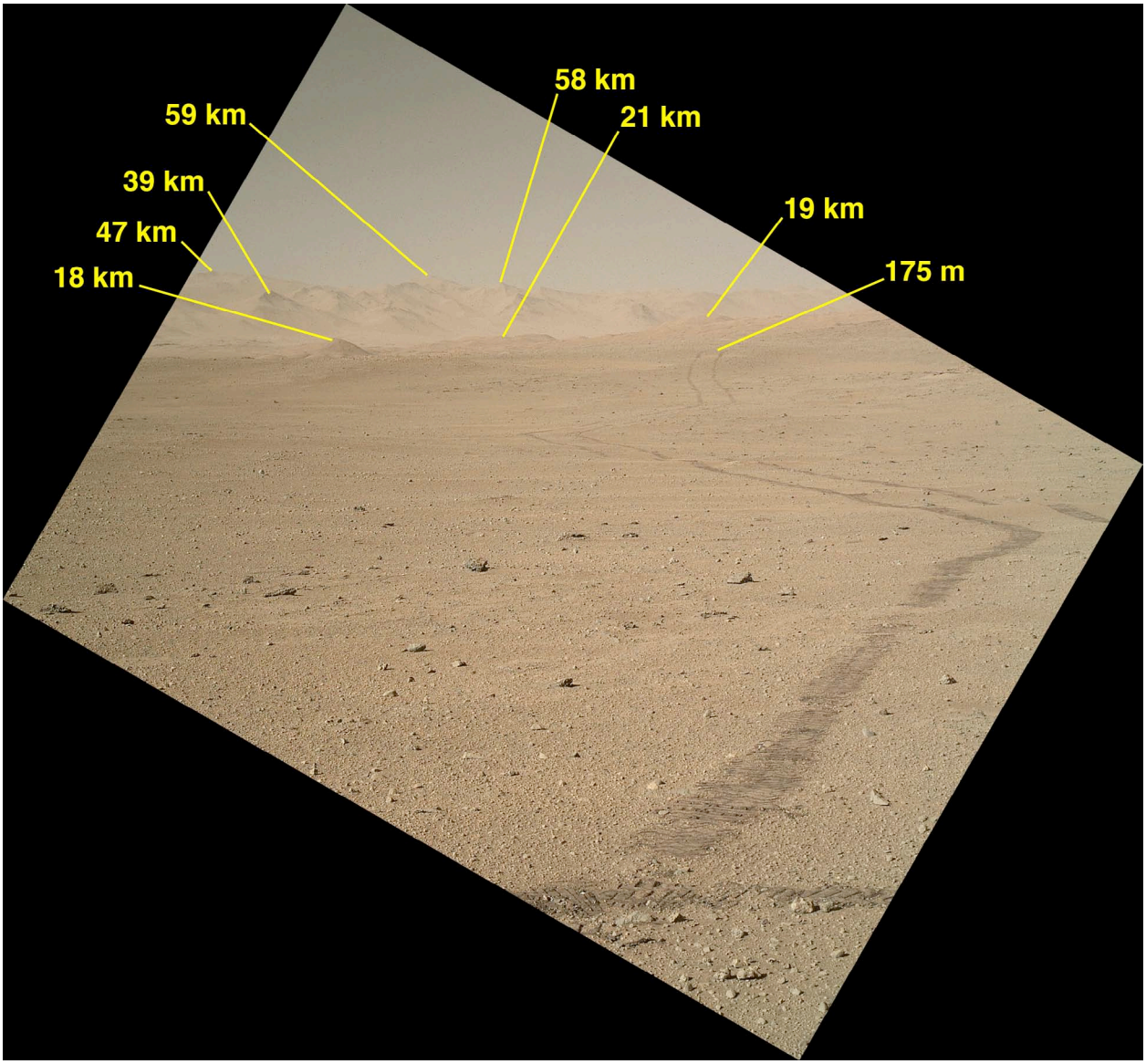

Figure 16. MAHLI view of the landscape east of Curiosity in northern Gale on Sol 644 (29 May 2014; image 0644MH0003250050203801E01). The rover wheel tracks provide an indicator of scale out to 175 m from the rover, where they disappear over a hill crest; each rover wheel is 40 cm wide and the distance between their outside edges is 280 cm (Heverly *et al*., 2013). The ranges between the rover and landforms in the middle (18–21 km) and far (39–58 km) distances are indicated to the nearest km. The distant slopes are the east wall and rim of Gale crater. Using **Equation 2**, the scale at 175 m is ~6 cm/pixel and the scale at 59 km is ~21 m/pixel.

4.5.2 Range and scale from motor count and nested imaging

The alternative method to estimate the scale of features in MAHLI images, at least for in-focus elements in images of targets roughly 2.1 to 210 cm from the front lens element, is to use **Equation 3** to determine working distance from motor count, then use **Equation 2** to determine pixel scale from working distance. The range of uncertainty in these values is estimated by considering the depth of field (**Equation 6**). Some motor count positions cannot be used to determine scale, especially when the camera was focused at infinity or at the minimum d_w.

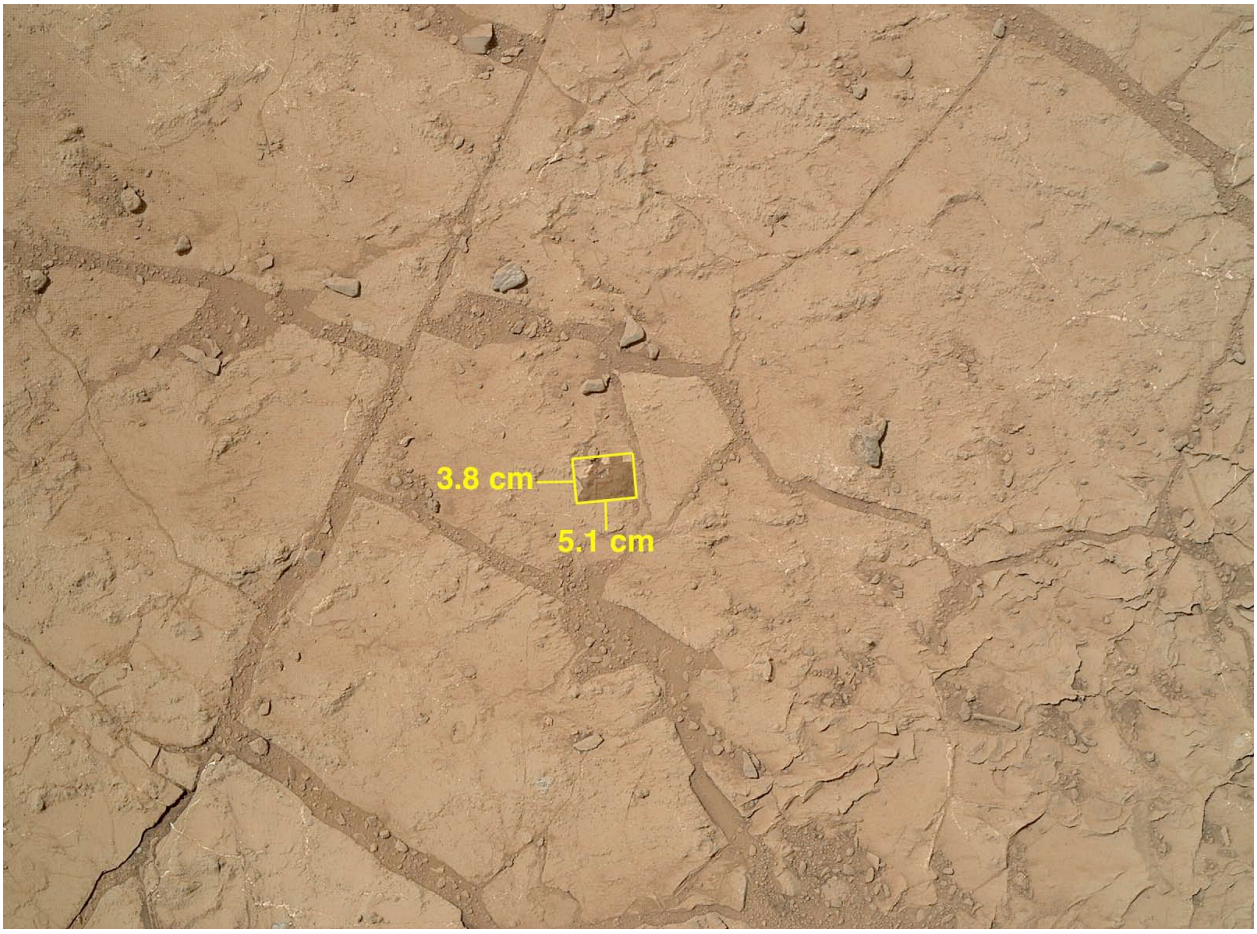

Figure 17. Example use of a nested high resolution MAHLI image to determine the scale of a lower resolution MAHLI image of the same target. The lower resolution image (0179MH0002180010102478C00) was acquired at a standoff (MAHLI toolframe +X) distance of ~200 cm and the nested image at the center (0179MH0001220010102490E01) was acquired from a 5 cm standoff. The lower-resolution image was focused at m_{open} 12608 using a centered 480 x 480 pixel autofocus sub-frame (0179MH0002180000102477E01). Using **Equations 2 and 3** and m_{open} 12608 yields a scale of ~720 µm/pixel. The 5 cm standoff image, also acquired as a full-frame via a centered, autofocus sub-frame (0179MH0001220000102489E01), was focused at m_{open} 13969, indicating a 31.7 µm/pixel scale and an area of 5.1 by 3.8 cm. Nesting the higher resolution in the lower resolution image yielded more accurate scale information, in this case indicating that the lower resolution image has a scale of ~690 µm/pixel and covers an area ~111 by ~83 cm.

For targets at d_w < 21 cm, the uncertainty of both distance and pixel scale is small and the uncertainty decreases with decreasing d_w. For targets at greater d_w, for example 21–210 cm, we usually nest a higher resolution image of the same target within the lower resolution image(s). This higher-resolution, nested image provides a semi-independent measure of scale for the lower resolution image. That is, the scale determined from the motor count of the higher resolution image, especially if acquired in the d_w 2.1–10 cm range, is more accurate than that of an image acquired from a d_w of, say, 50–210 cm. As **Figure 17** illustrates, one can determine the scale of the higher resolution image, and hence the dimensions of the area it covers, then re-size that image to fit its location within the lower-resolution image; effectively, the higher-resolution image provides scale information for the lower-resolution picture that is more accurate than determined from the lower-resolution image motor count.

We use motor count routinely to determine working distance and pixel scale for the in-focus elements of high resolution MAHLI images. The approach has been confirmed, on Mars, by

comparing the results of using the motor count with measurements of objects of known scale. For example, MAHLI image 0034MH0000450010100035C00 shows the U.S. cent on the MAHLI calibration target. The machined hole into which the cent was inserted has a diameter of 19558 µm. The diameter of this hole, as measured from the image, is 797±2 pixels. This measurement yields a scale of 24.5 ± 0.1 µm/pixel. The motor count, established via a centered, autofocus sub-frame, is 14376. Using **Equations 3 and 6**, this m_{open} corresponds to a d_w of 4.9 ± 0.1 cm. Using **Equation 2**, this yields an image scale of 24.1 ± 0.3 µm/pixel.

We have put the capabilities to determine scale and working distance from motor count to good use during the MSL mission, not just to make geological interpretations but also to use the instrument as a range finder for subsequent instrument or tool placement. For example, Minitti *et al.* (2013) described how MAHLI was used as a range finder for scoop placement during the Rocknest sample extraction campaign in October–November 2012, and Robinson *et al.* (2013a) illustrated the utility of MAHLI images in positioning Curiosity's drill for sample extraction.

5 Camera head positioning and stability characterization

MAHLI can acquire in-focus images of any illuminated scene for which d_w exceeds 2.04 cm. The camera can also acquire images of the Martian landscape when the robotic arm is stowed or unstowed. Most MAHLI imaging, of course, requires the robotic arm and turret to position the camera at a desired distance relative to a given target. Once positioned, there is a period during which arm, turret, and camera head motion dampens before images are acquired. Then, to prevent image blur, the MAHLI camera head should not move while an image is being acquired. Further, camera head motion should be minimal while acquiring a focus stack. In addition, it is further desirable that the arm is able to position MAHLI at a given target more than once; for example, this permits "before and after" imaging of surfaces drilled, scooped or brushed by Curiosity's tools.

5.1 Pre-launch tests regarding camera motion during image acquisition

Camera head motion is minimized during nominal MAHLI operations on Mars simply by not operating other instruments and rover mechanisms while imaging. However, the rover's thermal management system includes a mechanically pumped fluid loop subsystem (Bhandari *et al.*, 2013) that can be operating when MAHLI is acquiring data. Curiosity has a redundant pair of these Rover Integrated Pump Assemblies— *i.e.*, RIPA-A and RIPA-B.

To determine whether RIPA operation would impact MAHLI image quality or cause the camera to move during focus stack acquisition, we conducted two tests during ATLO on 02 December 2010. In the first test, the robotic arm positioned MAHLI at a d_w of 4.9 cm from the bar target at the center of the flight MAHLI calibration target. Then, with the RIPA-B pump operating, we acquired an in-focus, 8-frame video (images ATL_MH10120100100000153J00 through ATL_MH10120100100000160J00) at a rate of 1 per ~3 seconds. Then we turned off the pump and repeated the 8-frame video sequence (images ATL_MH10120100200000161J00 through ATL_MH10120100200000168J00). We compared the images; quality (*e.g.*, blur) was unaffected

although the position of the camera was offset very slightly (≤ 1 pixel) following the shut down of RIPA-B.

In the second test, we placed a duplicate of the planar bar target shown in **Figure 8** on a stand in front of the rover on the near side of the robotic arm workspace (Robinson *et al*., 2013b). Then the arm positioned MAHLI at a d_w of 2.8 cm above the target. Again we acquired an in-focus,
8-frame video (images ATL_MH10120100600000172J00 – ATL_MH10120100600000179J00) at a rate of 1 per ~3 seconds with the RIPA-B pump on. The video was then repeated with the pump off (images ATL_MH10120100700000180J00 through ATL_MH10120100700000187J00). As with the preceding test, operation of MAHLI with the pump on had no impact on image quality nor motion; turning the pump off changed the camera position slightly, about 1–2 pixels, but again had no effect on quality (*e.g*., blur).

We conducted an additional test on 02 December 2010 to examine whether the motion of MAHLI's lens mechanism might induce motion in the robotic arm. Using a laser tracking system (Robinson *et al*., 2013b), the arm and turret were monitored while the MAHLI lens mechanism autofocused on a three-dimensional target, located ~31 cm below the camera in the arm work volume (image ATL_MH10120100800000188B00). We observed no motion.

5.2 Motion damping before image acquisition

Knowledge of the duration of motion damping, after the robotic arm positions MAHLI for imaging, is vital for scheduling the rover's activities on Mars. If the motion damping duration is long, waiting for the camera head to stop moving can reduce the number of positions at which the arm can place MAHLI, APXS, or other tools on the turret on a given sol.

5.2.1 Duration determined before launch and best practice for Mars operation

We examined the duration of motion damping after robotic arm positioning of the MAHLI camera head before launch using a laser tracking system (Robinson *et al*., 2013b). No MAHLI images were acquired during the test, which repeatedly placed the camera head in the robotic arm work volume. We observed that motion damped to < ± 10 µm oscillations (toolframe Y and Z dimensions) and < ± 25 µm oscillations (toolframe X dimension) within 40 seconds; characterization at smaller oscillation values was not possible.

Given the pre-launch knowledge, our best practice for acquisition of most high resolution MAHLI imaging on Mars is to wait 90 seconds for motion damping. However, we do desire to learn whether this period can be shortened, as 90-second wait periods can add up when the camera is positioned at multiple targets during a robotic arm contact science session. One case became particularly important in late 2013, when the rover team became concerned about damage to Curiosity's wheels.

5.2.2 Duration determined on Mars for wheel inspection imaging

In November 2013, Curiosity's engineering team began a regular program to monitor how the wheels were changing as the rover traversed across the rugged landscape of northern Gale crater. When the rover drives, its robotic arm, turret, and the MAHLI camera head are stowed. Part of the wheel monitoring effort involves unstowing the robotic arm and pointing MAHLI at the

wheels—from the same vantage point every time this is performed—to acquire an image of each wheel. Sometimes we would image only the portion of each wheel that was in view at the end of a given drive; and sometimes we would document the entire circumference of each wheel. The latter involves unstowing the arm, imaging the wheels, stowing the arm, driving the rover a small distance to reveal another portion of each wheel, unstow the arm, image the wheels with MAHLI, re-stow the arm, drive another small increment, and repeat until it has been performed 5–6 times to cover ≥ 360° on each wheel. On a given sol, this process reduces the amount of time available to perform other activities (*e.g.*, drive to a new location, acquire science data), in part because of the 90-second motion damping wait periods for each wheel.

Thus, on Sol 472 (04 December 2013), we conducted a motion damping test specifically designed to determine the minimum wait time for imaging the wheels. The nearest wheel is viewed from a d_w of ~137 cm; the farthest is ~320 cm away, thus the sensitivity to motion and blur is less than is the case for very high resolution images acquired over the d_w 2.1–30 cm range. Furthermore, the wheel images were focused manually because their distance from the wheel inspection viewing positions was previously determined via autofocus sub-frames obtained on Sol 177 (04 February 2013). Thus, motion damping would not impact autofocus efforts should the duration be shortened.

For the Sol 472 test, the arm and turret positioned MAHLI to view each wheel, as usual for these inspections. Then, with no imposed wait period, we acquired five full-frame images at the following intervals after the camera arrived in position for each wheel: 17, 27, 52, 77, and 102 seconds. The images are listed in **Supplement S06**. For each wheel, we, and the rover mobility (wheel) engineers, compared the images and concluded that all were sufficiently in focus to meet wheel inspection objectives. The wait time for motion damping for wheel imaging was thereafter set at 15 seconds—in addition to the 17 seconds for camera preparation—for an effective 32 seconds between camera arrival and image acquisition.

5.3 Camera motion during image acquisition as observed on Mars

While wait periods can be and usually are inserted into MAHLI imaging plans to accommodate motion damping after the robotic arm moves the camera head into position, occasionally the images returned from Mars do show evidence for motion during image acquisition. The cases have been unusual enough that they have not received deep investigation as to the cause, but we suspect these motions are induced by wind.

We observed one example by comparing images 0093MH0000860000101065C00 and 0093MH0000860010101066C00, obtained on Sol 93 (09 November 2012). The first picture is an autofocus sub-frame used to determine focus for the second, full-frame image. Acquired ~12 seconds apart, they show sand and silt on Curiosity's observation tray. Where the two images overlap, a change in camera position of about one pixel toward the upper right (relative to pixel 0, 0 at the upper left of the CCD) is observed; the inferred camera head motion is about the same as the pixel size, 7.4 µm.

Additional examples of camera motion during image acquisition were observed on Sol 883 (30 January 2015) during night imaging with LED illumination. In one case, an autofocus sub-frame (image 0883MH0004320040302613C00), focused 9.1 cm away on cuttings inside a drill hole created on Sol 882 (named Mojave_2), was in sharper focus than the subsequent full-frame image (0883MH0004320050302614C00) acquired ~10 seconds later. These observations

suggest that the camera was moving, ever so slightly, during the 5052.6 millisecond full-frame image exposure, such that it is blurred relative to the sub-frame.

In the other Sol 883 case, a series of images of drill cuttings acquired from a ~3.6 cm working distance (outside Mojave_2 drill hole), were all somewhat blurred. The autofocus sub-frame, 0883MH0004090000302627C00, was not as sharply focused as nominal autofocus sub-frames. Neither were the corresponding full frame images in sharp focus, such as image 0883MH0004090020302629C00. Further, the area covered by both of these frames was offset by more than one pixel (but less than three pixels). In this case, camera head motion might have prevented a sharp autofocus solution and camera head motion continued throughout acquisition of the subsequent series of eight images (various permutations of white light LED, UV LED, and dark frame acquisitions).

Night images of drill cuttings acquired on Sol 910 (27 February 2015), illuminated by MAHLI's LEDs, again showed similar evidence for motion (*e.g.*, images 0910MH0004730000303033C00 and 0910MH0004730020303035C00). The observations from Sols 93, 883, and 910 show that we have indeed observed camera head motion during image acquisition on Mars but it has rarely occurred to a degree that it impacts the science or engineering utility of the data. During daylight imaging, the short exposure durations minimize the effect. In cases for which the science or engineering objective of a given image or image suite is not met because of camera head motion, the science team can consider re-imaging the target; thus far, no situation has occurred in which this was necessary.

5.4 Camera head positioning and repeatability

The ability of the MSL robotic arm to position the MAHLI camera head to within millimeters of a desired location in the robotic arm workspace was well understood from testbed activities such as the observation of a U.S. cent, placed on a rock, described by Edgett *et al.* (2012). Further, before launch, the robotic arm engineers established reference "teach" points at which the arm could return MAHLI to specific locations for rover hardware inspection (Robinson *et al*., 2013; Collins and Robinson, 2013) and the pre-launch repeated arm positioning and MAHLI imaging of these targets was superb (Edgett *et al*., 2012). The teach points were re-imaged on Mars by MAHLI on Sols 34, 36, and 37 (10, 12, 13 September 2012) and the slight differences between the locations as viewed on Earth and Mars were used to validate adjustments for arm operation under Martian conditions (Robinson *et al*., 2013b).

The first opportunity to perform repeated positioning of MAHLI at a geologic target occurred on Sols 46 and 47 (22 and 23 September 2012) at a boulder—visible in images even acquired from orbit (*e.g*., HiRISE ESP_028612_1755)—that the MSL science team named Jake Matijevic (Collins and Robinson, 2013). **Figure 18** shows that the MAHLI camera head was placed at the same surface on this boulder on Sol 46 and again on Sol 47. Each time, MAHLI was placed at standoff distances near 25, 5, and 2.5 cm. The 25 cm standoff distance images, 0046MH0000090010100121C00 on the first sol and 0047MH0000130010100174C00 on the second, found focus, via autofocus, at m_{open} of 13018 and 13016, respectively. This difference of only 2 motor counts is negligible and indicates ≤ 1 mm of difference in the working distance from one sol to the next. The placement at 5 cm standoff and 2.5 cm standoff yield a similar result; ≤ 1 mm difference in working distance. As for the difference relative to planes parallel to the CCD, **Figure 18** illustrates the offset between the two images acquired from 2.5 cm standoff; the offset was < 1 mm in both directions (pixel rows and columns).

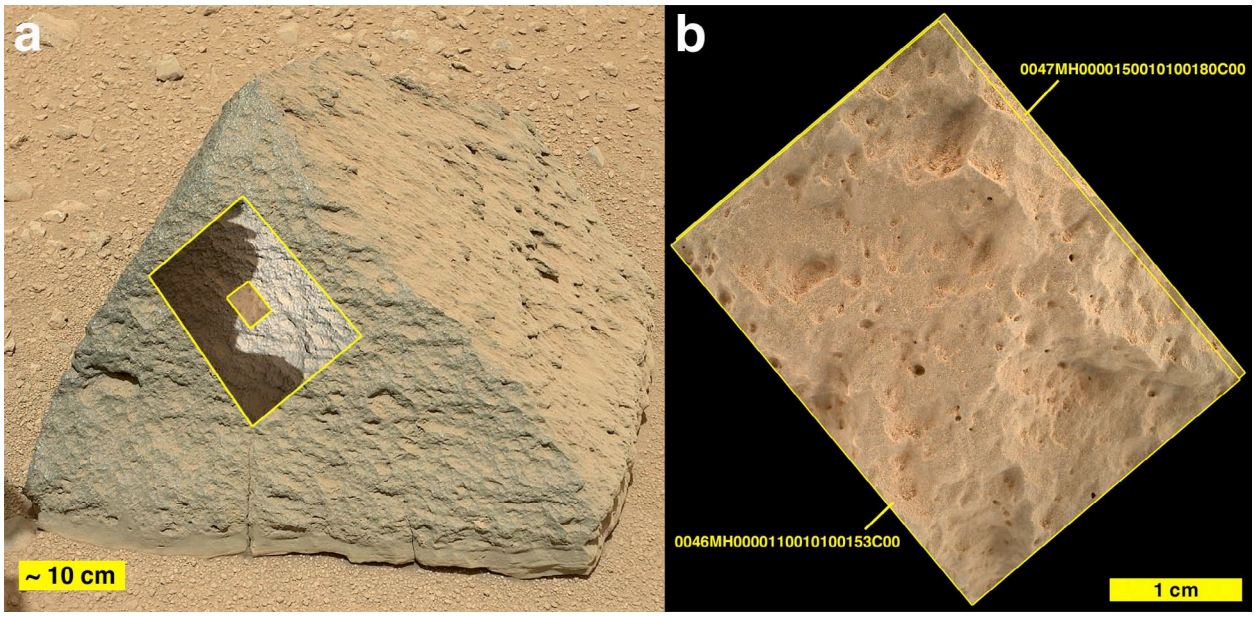

Figure 18. Illustration of Sol 46 and 47 robotic arm and MAHLI positioning repeatability test results. **(a)** Mastcam-34 image 0046ML0002120000102098E01 showing the boulder named Jake Matijevic. The inset shows the locations of MAHLI Sol 46 25 cm standoff (toolframe +X) context image 0046MH0000090010100121C00 and 2.5 cm standoff image 0046MH0000110010100153C00. **(b)** MAHLI 2.5 cm standoff images acquired on Sols 46 (0046MH0000110010100153C00) and 47 (0047MH0000150010100180C00), illustrating their excellent overlap. The offsets were 30 pixels (0.66 mm) toward the upper right and 6 pixels (0.15 mm) toward the upper left; m_{open} of 14528 and 14513, respectively, show that the difference in the optic axis direction (working distance) was ≤ 1 mm. The rock surface appears to be brownish-orange in the images on the right in part because of the presence of Martian dust but also because they were shadowed at the time of acquisition.

5.5 Imaging with incremental turret rotation

We usually obtain MAHLI image mosaics by having the entire robotic arm move the camera head from one position to the next, with suitable overlap between images for each case. Stereo pairs are usually acquired by translating MAHLI in the same plane (parallel to the CCD) from a stereo-1 position (with optic axis normal to the target) to a stereo-2 position; sometimes pairs are acquired by rotating the camera, relative to the plane of the stereo-1 image, such that the target is viewed off-normal and the stereo-2 image more completely overlaps the stereo-1 image.

Turret rotation provides another option for acquisition of stereo pairs and mosaics without full motion of Curiosity's robotic arm. This option has not often been exercised. We performed a test on Sol 322 (02 July 2013) by imaging the U.S. cent on the MAHLI calibration target. The cent was fully shadowed, causing a brownish-orange cast, but this did not impact the results. **Figure 19** shows a mosaic of the six MAHLI frames acquired during the test; the data can also be used to make stereo products (*e.g.*, anaglyphs; quantitative relief models).

The cent was first imaged, with the camera centered on the coin and the optic axis normal to the target, at a d_w of 4.9 ± 0.1 cm. Then, the turret rotated the smallest possible increment, ~5 mrad, and we obtained a second image. This was followed by two more 5 mrad turret rotations, then a 16 mrad rotation and a 25 mrad rotation. As shown in **Table 6**, the first rotation did not move the camera head as far as expected; we attribute this to backlash in the turret movement.

Thereafter, each movement of the turret was as expected and the motion, as registered by the MAHLI images, was about 13.2 pixels per mrad of turret rotation.

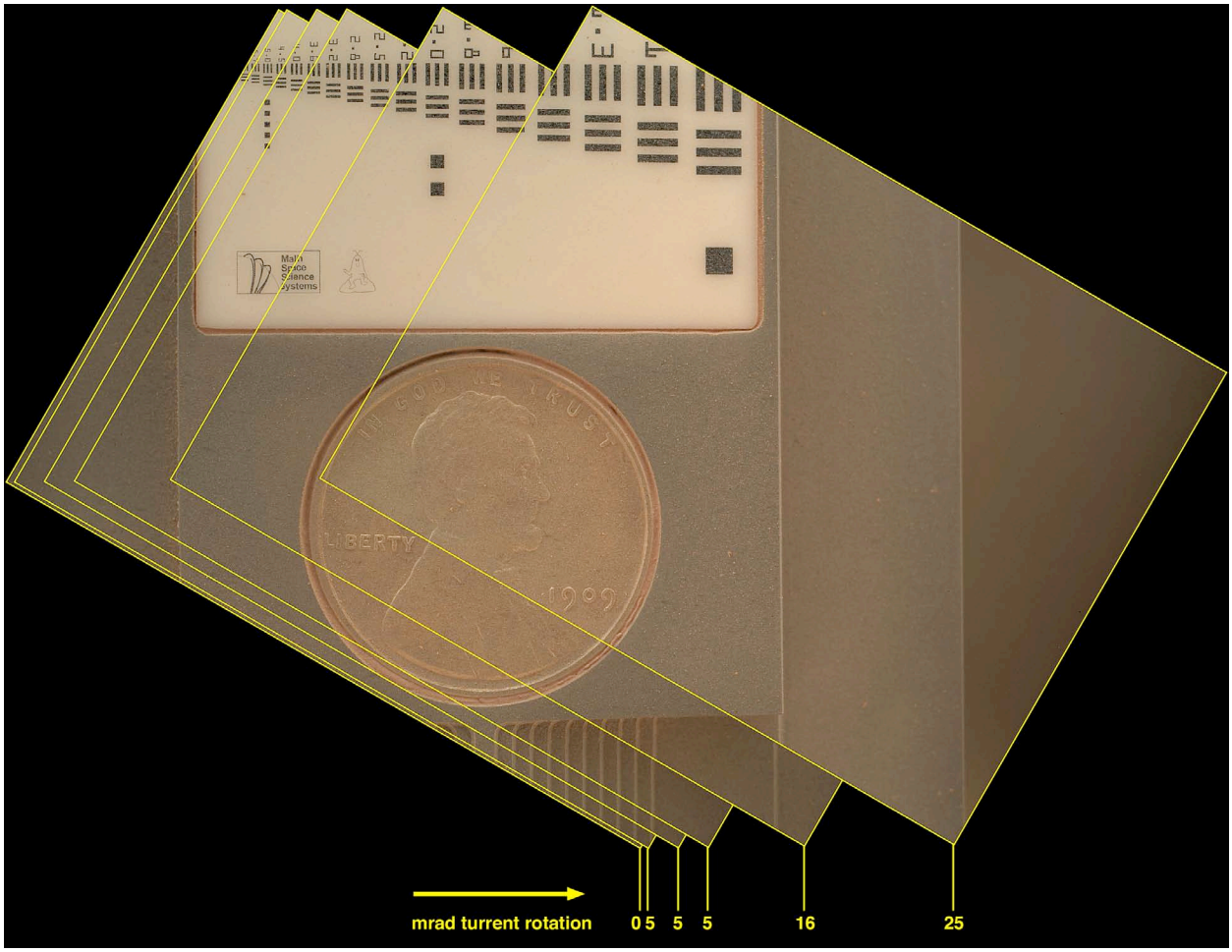

Figure 19. MAHLI turret rotation image mosaic test conducted on Sol 322 (02 July 2013) while viewing the 19-mm-diameter U.S. cent on the MAHLI calibration target. The commanded turret rotations are indicated in milliradians (mrad); the first increment, from 0 to 5 mrad, did not move as far as expected; this is thought to indicate backlash motion after the rotation occurred. Subsequent rotations of 5, 5, 16, and 25 mrad are also indicated. The 5 mrad rotation is the smallest increment possible. Turret rotation over small increments offers an additional method to acquire MAHLI mosaics and stereo pairs. These images are 0322MH0002150010103933C00 through 0322MH0003010000103938C00 and were acquired at a time that the calibration target was fully shadowed, hence the brownish-orange cast.

Table 6. Sol 322 test of MAHLI imaging via incremental rotation of Curiosity's robotic arm turret; cent target at 4.9 ± 0.1 cm working distance; see Figure 19

Image ID	Com-manded rotation (mrad)	Tracked pixel location			Linear delta (change; pixels)	Measured Rotation (pixels per mrad)
		Column (x)	Row (y)	Distance Moved (pixels)		
0322MH0002150010103933C00	0	1127	35	0	0	0
0322MH0003010000103934C00	5	1112	45	18.03	18.03	3.61
0322MH0003010000103935C00	5	1054	79	85.23	67.21	13.44
0322MH0003010000103936C00	5	998	113	150.75	65.51	13.10
0322MH0003010000103937C00	16	816	222	362.89	212.14	13.26
0322MH0003010000103938C00	25	534	389	690.63	327.74	13.11

6 Onboard image products characterization

6.1 Data compression and color interpolation

MAHLI and the three other MSL cameras that share its electronics design—Mastcam-34, Mastcam-100, and MARDI—can each produce a range of compressed and uncompressed data products (Edgett *et al*., 2012) which are transferred to the rover's computers for transmission to Earth. Transmission is relayed from the rover to Earth through one or more Mars-orbiting spacecraft (Edwards *et al*., 2013).

Table 7 lists the MAHLI data product types that can be produced by the instrument. These include uncompressed, losslessly compressed, and lossy compressed images; video frames and groups of pictures (GOPs); and thumbnail images. The products also include best focus, range map, and corresponding thumbnail images produced by onboard focus merges. The lossy compressed products are in JPEG form; the products of an onboard focus merge can only be JPEGs (Edgett *et al*., 2012).

Table 7. MAHLI, Mastcam, MARDI image type product characterization

type	product format	earliest acquired example received from Mars		
		Sol	camera	image ID
A	raster 16-bit image	270	MAHLI	0270MH0002490050200001A00
B	raster 8-bit image	17	Mastcam-34	0017ML0000500100100223B00
C	lossless compressed image	0	MARDI	0000MD0000000000100027C00
D	JPEG grayscale image	3	Mastcam-34	0003ML0000001410100003D01
E	JPEG 4:2:2 color image	0	MARDI	0000MD0000000000100001E01
F	JPEG 4:4:4 color image	20	Mastcam-100	0020MR0000110020100256F01
G	raster thumbnail of parent image	159	MAHLI	0159MH0000720050101726G01
H	JPEG gray thumbnail of parent image	147	Mastcam-34	0147ML0000835003010442OH01
I	JPEG 4:4:4 thumbnail of parent image	0	MARDI	0000MD0000000000100001I01
J	raster 8-bit video frame	165	MAHLI	0165MH0001880180102010J00
K	lossless compressed video frame	37	Mastcam-34	0037ML0000990110101095K00
L	JPEG grayscale video frame	37	Mastcam-34	0037ML0000990110100922L01
M	JPEG 4:2:2 color video frame	61	Mastcam-34	0061ML0003150000102377M00
N	JPEG 4:4:4 color video frame	165	MAHLI	0165MH0001880210102042N01
O	raster 8-bit thumbnail of video frame	165	MAHLI	0165MH0001880180102010O01
P	JPEG gray thumbnail of video frame	165	MAHLI	0165MH0001880200102026P01
Q	JPEG 4:4:4 thumbnail of video frame	35	Mastcam-34	0035ML0001440120100885Q01
R	focus merge best focus image product	36	MAHLI	0036MH0000550000100066R00
S	focus merge range map product	36	MAHLI	0036MH0000550000100067S00
T	focus merge best focus thumbnail	36	MAHLI	0036MH0000550000100066T01
U	focus merge range map thumbnail	36	MAHLI	0036MH0000550000100067U01

Types R and T are JPEG 4:4:4; S and U are JPEG grayscale products.

Also as described by Edgett *et al.* (2012), the Bayer pattern color interpolation implemented onboard MAHLI is based on the method described by Malvar *et al*. (2004). The onboard lossy (JPEG) capability includes $Y{:}C_R{:}C_B$ subsampling (in which Y is luminance and C_R and C_B are red and blue chrominance components). The options for JPEG color compression (**Table 7**) are 4:4:4 (no color subsampling) or 4:2:2 (chrominance subsampling by a factor of 2); grayscale (colorless) JPEGs can also be produced.

Data returned from MAHLI in uncompressed or losslessly compressed form are not demosaicked; that is, no color interpolation is performed onboard the instrument. Receipt of these images provides the data user with the option to apply alternative Bayer demosaicking algorithms (*e.g.*, reviews by Li *et al.* (2008) and Getreuer (2011)).

6.2 Product type identification, creation, and receipt on Earth

The product types produced onboard the instrument are indicated by an alphabetical letter from A through U (**Table 7**). This letter is the 23rd character in the image ID for every MAHLI, Mastcam, and MARDI product archived with the NASA PDS. Many of these A–U product types were not produced by the instrument before launch. Thus, **Table 7** indicates the earliest acquired example of each product type received from Mars. This documentation is important because it constitutes part of the MAHLI instrument characterization effort; their onboard production, on Mars, was required by the PDS so that the archivists had an example of each type for review and documentation purposes.

Because of the NASA PDS requirement, MAHLI was specifically commanded on Sols 159, 165 and 270 to produce and return examples of product types A, G, J, N, O, and P (**Table 7**). The majority of MAHLI images returned from Mars have been of types C (losslessly compressed images), E (JPEG 4:2:2 color images), I (JPEG 4:4:4 color thumbnail products), and the four focus merge product types R, S, T, and U. Most of the pre-launch MAHLI data were of types B (uncompressed 8-bit images) and A (uncompressed 16-bit images).

6.3 Onboard focus merge product creation and assessment

6.3.1 Capability and options

A macro lens focused on a target at a small working distance has a limited depth of field. Thus, some parts of a subject photographed will be in focus while other parts, if the relief exceeds the depth of field, will not. This effect can be used to a photographer's artistic advantage, but sometimes an image will have a more technical purpose for which there is value in seeing all or most parts of the scene in focus. One can acquire a focus stack (also known as a *z*-stack, in reference to the common practice of denoting the camera's optic axis as *z*) to resolve the latter concern.

To obtain images for a focus stack, a series of pictures is acquired by changing focus between each image so as to capture in-focus views of different elements at different distances in the scene. Ideally, the change in focus position between images does not exceed the depth of field. Preferably, as is the case for MAHLI, the camera is not moved so that d_w remains constant; an alternative, for a fixed-focus system, is to move the camera toward or away from the subject (this is, for example, how the Mars Exploration Rover (MER) Microscopic Imager (MI) acquires focus stacks (Herkenhoff *et al*., 2006)).

Edgett *et al.* (2012) described the MAHLI focus stack capability. After acquisition, onboard software identifies the parts of each image in the focus stack that are in best focus and merges them into a single best-focus image product. A by-product of this processing is creation of a range (also known as depth) map that provides an approximate view of the target's relief. MAHLI can perform focus merges of up to eight consecutively acquired focus stack images.

Doing so inside the instrument provides a form of data compression, turning as many as eight uncompressed images into two, a color JPEG best focus image and a grayscale JPEG range map, for downlink to Earth. An example from Mars is shown in **Figure 20**.

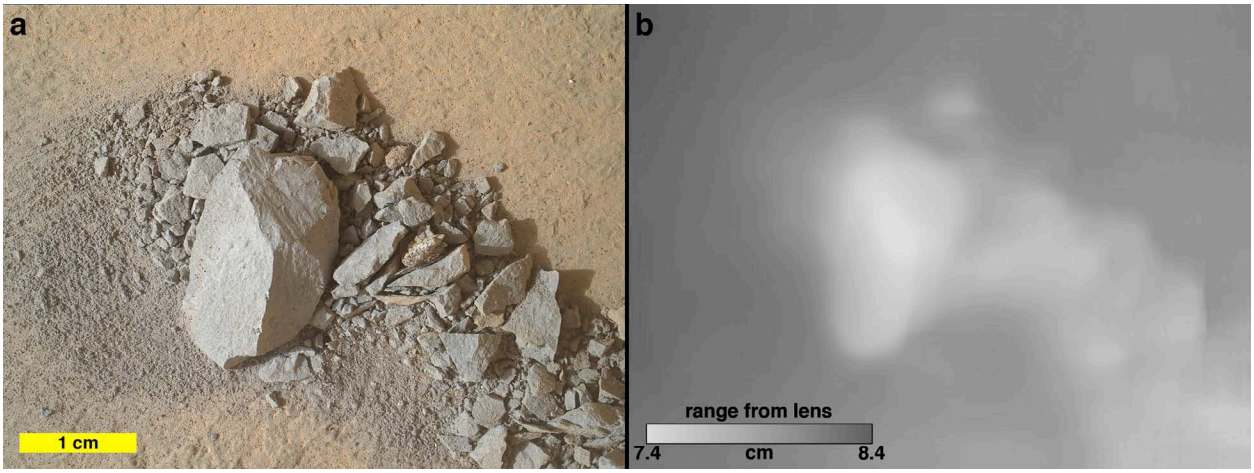

Figure 20. Example MAHLI focus merge products and estimation of micro-relief used by robotic arm engineers to determine placement for another instrument, the APXS, on a subsequent sol. **(a)** Best focus image product 0869MH0004610000302276R00, created by a basic merge onboard MAHLI conducted on Sol 869. Sunlight illuminates the scene from the left/lower left. **(b)** Range map product 0869MH0004610000302277S00 with scale indicating distance from MAHLI's front lens element to the surface indicated. This product determined the range to within ± 0.1 cm. It has been altered from the original downlinked product by inverting DN values (0 changed to 255, 255 to 0) so that nearer surfaces are lighter in tone. The merge was performed on the focus stack of eight parent images, acquired on Sol 869 (16 January 2015), that are listed in **Table 10**.

The onboard focus merge capability includes options for merge-only, merge + registration, merge + blending, or merge + registration + blending (Edgett *et al*., 2012). Registration and blending are more computationally intensive capabilities that can be employed in cases in which the camera might have moved, slightly, during acquisition of the focus stack. Operation on Mars during Curiosity's first 911 sols usually exercised the computationally faster merge-only option; the alternative options were only exercised once during this period—as a characterization test—on Sol 853, as reported in **Section 6.3.5**.

Table 8 summarizes the default onboard focus merge parameters. The Kanade-Lucas-Tomasi (KLT) feature tracking capability is based on the work of Lucas and Kanade (1981) and Shi and Tomasi (1994). Harris corner detection identifies feature points and tracks them between image pairs in the focus stack; this is based on the work of Harris and Stephens (1988). The blending option combines the images using multi-resolution spline-based image blending based on the work of Burt and Adelson (1983).

6.3.2 Focus stack acquisition and reporting

MAHLI focus stacks are acquired while the rover's robotic arm holds the camera in a fixed position. The lens mechanism moves the lens focus group according to a commanded number of motor count steps to perform a commanded number of image acquisitions. As the instrument can only merge up to 8 consecutive focus stack images onboard, we acquire most focus stacks with just 8 images, each with an equal number of motor counts separating them. On some occasions, the target might have considerable surface relief relative to the depth of field and thus we will obtain a 16-image stack (it is possible to acquire even more than this). In such a

case, we select the best candidate 8 consecutive images, of the 16, to merge onboard. Alternatively, we might downlink some or all of the 16 images and perform a merge using software available on Earth; an example of this occurred on Sol 828, 05 December 2014, to acquire five 16-image focus stacks covering an outcrop informally named Chinle.

Table 8. MAHLI default onboard focus merge parameters

Focus measure parameters	
find translations between images	1
blend the focus image	0
focus measure step size	5
focus measure window size	101 x 101
focus measure threshold	0.01
Harris corner detection parameters	
threshold (factor of maximum threshold value)	0.01
Harris criterion constant (Kappa)	0.04
pixel quality window size	3
tile size	64 x 64
maximum number of corners for each tile	200
minimum separation of corners inside of a tile	10
excluded border pixels	16
Kanade-Lucas-Tomasi (KLT) tracker parameters	
search window size	9 x 9
maximum iterations for search	10
number of resolution levels (pyramids) for search	3
regenerate points for each frame	1
minimum distance for search iteration	0.1
maximum residue (average intensity difference)	5.0

The maximum focus stack image size that can be processed onboard the instrument is 1600 by 1200 pixels and the output focus merge products have the same number of pixels (rows and columns) as the individual input frames. We usually acquire focus stack images of dimensions 1584 pixel columns by 1184 pixel rows, with the starting pixel at column 32, row 16, so as to trim the dark pixel columns from left and right sides of each image. We also usually obtain a 1632 by 1200 image with dark column pixels on the left side of the frame just before the focus stack acquisition; this image is usually focused via a preceding, centered autofocus sub-frame. Its purpose is to show the entire target as best as can be obtained simply by autofocus, so that the data user can evaluate the manner in which a focus merge product represents the scene; and to obtain the dark pixel columns that can be used to document dark current in a focus merge product or in the individual focus stack frames.

Focus stack acquisitions can be based on a *relative* or an *absolute* starting focus position. A relative stack is one in which a previously determined focus position (*i.e.*, motor count) is assumed to be one of the positions in the focus stack and the other focus stack image are acquired at focus positions relative to that one. The most typical manner in which MAHLI focus stacks are acquired on Mars is to use this relative mode via following steps:

1 Acquire an autofocus sub-frame view of part of the target (usually at the CCD center) to establish focus.

2 Obtain a 1632 by 1200 pixels image of the target using the focus position determined by the preceding autofocus sub-frame.

3 Acquire a relative focus stack with images consisting of 1584 by 1184 pixels.

For an 8-image stack, the fifth image in a relative stack has the same motor count as was determined by the previous autofocus; for a 16-image stack, it is the ninth image.

An absolute focus stack is one in which we manually command the focus motor count positions. We employ this approach when d_w is known well enough prior to commanding, and the surface relief (range from lens to various elements near and far from the lens in the same field of view) can be captured sufficiently using *a priori* knowledge gleaned from MAHLI, Navcam, Hazcam, and/or Mastcam images acquired on a preceding sol.

We record, manually, whether a given focus stack was acquired by relative or absolute commanding in the PDS archived image RATIONALE_DESC field in the label (.LBL) of the focus stack parent images (and their thumbnails). The RATIONALE_DESC also notes the position of each image in the stack, such as, "image 5 in 8-image relative focus stack." Individual focus stack images are not all nor always returned to Earth, but their 1/8th-size thumbnail images are returned.

6.3.3 Focus merge product reportage and traceability

All MAHLI focus merge products created onboard the instrument are readily recognized in the NASA PDS archives by their file names (**Table 7**). Best focus images are product type R (*e.g.*, the capital R in the following file name: 0036MH0000550000100066R00), range map products are type S (*e.g.*, S in 0036MH0000550000100067S00); their thumbnail image filenames contain T and U, respectively. The motor count position reported in the label (.LBL file) for each archived focus merge product, the MSL:FOCUS_POSITION_COUNT, is equal to the motor count of the first parent image in the merged focus stack.

We manually track and report the individual focus stack images that were combined onboard to create a merged product; this information is captured in the .LBL file parameter, RATIONALE_DESC. The focus merge RATIONALE_DESC states the sol that the focus stack parent images were acquired and MSL:CAMERA_PRODUCT_ID identifiers of the images that were merged. The combination of sol and MSL:CAMERA_PRODUCT_ID uniquely trace the focus merge product back to the parent data.

Note that an onboard focus merge can be performed at any time after the focus stack is acquired until the parent images are deleted from the instrument's onboard storage. This means that a focus merge can occur on the same or a later sol than acquisition. An extreme example of this occurred on Sol 192 (19 February 2013), when onboard focus merges of four 8-image focus stacks acquired on Sol 60 (06 October 2012) were performed.

We also report the type of focus merge (merge only, merge + registration, merge + blending, or merge + registration + blending) and the number of images merged in the PDS archive .LBL file. This information is in the items listed under ZSTACK_REQUEST_PARMS. Parameter MSL:ZSTACK_IMAGE_DEPTH states the number of images commanded to be merged (which

should be 2–8 and should equal the number of MSL:CAMERA_PRODUCT_IDs in the range stated in the RATIONALE_DESC). The MSL:IMAGE_BLENDING_FLAG states whether the blending algorithm was applied (true or false), and the MSL:IMAGE_REGISTRATION_FLAG states whether the registration algorithm was applied (true or false).

6.3.4 Range information in range map products

Focus merge range map products produced by MAHLI are returned as grayscale JPEG compressed images. The pixel values (DN) range from 0 to 255. These are assigned by the onboard software on the basis of commanded focus stack depth (.LBL parameter MSL:ZSTACK_IMAGE_DEPTH). **Table 9** shows the relationship between each image commanded to participate in a focus merge and its corresponding grayscale DN value in a MAHLI range map product. In other words, if the instrument is commanded to merge eight images, DN values are assigned according to the second column in **Table 9**; if commanded to merge only four images, the corresponding DN values are those in the sixth column. DN values between those within a given column in **Table 9** are derived by linear interpolation during the focus merge process.

Table 9. Relation between commanded image participant in an onboard MAHLI focus merge and range map grayscale data value (DN)

image commanded to be merged	DN for 8-image merge	DN for 7-image merge	DN for 6-image merge	DN for 5-image merge	DN for 4-image merge	DN for 3-image merge	DN for 2-image merge
1st	255	255	255	255	255	255	255
2nd	223	218	212	204	191	170	127
3rd	191	182	170	153	127	84	—
4th	159	145	127	102	63	—	—
5th	127	109	84	51	—	—	—
6th	95	72	42	—	—	—	—
7th	63	36	—	—	—	—	—
8th	31	—	—	—	—	—	—

Each image we command to participate in an onboard focus merge is acquired with the lens focus group at a specific position, reported by as a motor count. The motor count position for each image is, in turn, related to range by **Equation 3** (note that one substitutes the term *range* for *working distance*; when a MAHLI focus stack is acquired, working distance does not change, but the range to each in-focus element of the target's relief does). Thus, the DN for each pixel in a MAHLI range map product is related to range through motor count.

Table 10 and **Figure 20** show an example for a focus stack of eight MAHLI images we acquired on Sol 869 (16 January 2015). To acquire the stack, the MAHLI camera head was positioned at a d_w of ~6.9 cm above the target; the camera acquired an autofocus sub-frame, followed by a full-frame image at that focus position, then a focus stack of 8 images relative to that autofocus position. The range map product, 0869MH0004610000302277S00, consists of pixels with DN values of 107 to 172. Consulting **Table 9**, for a commanded 8-image focus stack, these pixel values indicate that the first, second, seventh and eighth images had no in-focus pixels and were not participants in the final merge product. In other words, only portions of the middle four of the eight images were merged.

The utility of an onboard focus merge range map as a measure of surface relief is only as good as the input. This input is a function of the number of images planned to be acquired and merged, the range (distance) to in-focus elements in the scene captured by each image, whether the depth of field exceeds the distance between in-focus features in each image, and whether the images capture the full range to relief elements within the camera field of view. If the camera is commanded such that only one or two images in a given focus stack has in-focus features, then the range map will provide very limited information about surface relief; good examples of this occur in the Sol 58 (04 October 2012) range maps 0058MH0000320000100508S00 and 0058MH0000320000100510S00 (*i.e.*, the lower left quarter of the latter). In other words, range map products can serve as a rudimentary, quantitative map of micro-relief, but the vertical measurements are limited by the nature of the input focus stack.

Table 10. Example MAHLI onboard focus merge range map relation between pixel DN and range (see also Figure 20)

the images were acquired:	Sol 869	16 January 2015 UTC
the images were merged onboard:	Sol 869	16 January 2015 UTC
best focus image product ID:	0869MH0004610000302276R00	
range map product ID:	0869MH0004610000302277S00	

thumbnail image ID	merge participant?	motor count	range (cm)	DN in range map
0869MH0002770020302256I01	no	13659	9.8 ± 0.2	255
0869MH0002770020302257I01	no	13719	9.1 ± 0.2	223
0869MH0002770020302258I01	yes	13779	8.6 ± 0.2	191
0869MH0002770020302259I01	yes	13839	8.0 ± 0.1	159
0869MH0002770020302260I01	yes	13899	7.6 ± 0.1	127
0869MH0002770020302261I01	yes	13959	7.1 ± 0.1	85
0869MH0002770020302262I01	no	14019	6.7 ± 0.1	63
0869MH0002770020302263I01	no	14079	6.4 ± 0.1	31

In this case, the relationship between range (d_r) and DN (DN_r) is: $d_r = (5.8106 + 0.015135DN_r) \pm 0.1$ cm.

The merge products in **Figure 20** provide an example for which we actually used a focus merge product to estimate surface relief in service of the Curiosity's science objectives. That is, we used the range map to determine the distance between MAHLI and the top of the largest stone in the scene because this stone was to be a target for placement of the APXS instrument on a subsequent sol. Thus we used the range map to determine the position and shape of the stone so that the robotic arm operators could position the APXS.

6.3.5 Merge options characterization

As noted by Edgett *et al.* (2012), operations using the full-fidelity MAHLI aboard the testbed MSL rover at JPL-Caltech suggested that it is almost never necessary to exercise the options for focus merges that use the blending, registration, or blending + registration options. These operations take longer to perform onboard the instrument (**Table 11**). We required and implemented these options early in the MAHLI design period because there was considerable uncertainty as to whether the camera head might move during focus stack acquisition.

Thus our nominal approach on Mars has been to perform only the basic (merge only) option. Thus far, these basic focus merges have been as expected and they have satisfied the MSL science team's needs and requirements regarding the science and/or engineering content and utility of the products. However, to confirm this view, and to perform the blending, registration,

and blending + registration options for the very first time on the flight unit MAHLI, we exercised these on Mars on Sol 853 (30 December 2014).

Table 11. Summary of MAHLI onboard focus merge test of Sol 853

focus merge option	time to perform operation
basic (merge only)	5–6 minutes
merge + blending	12–13 minutes
merge + registration	8–9 minutes
merge + blending + registration	15–16 minutes

low surface relief example — Sol 819 rock target named Mescal — working distance ~ 6.6 cm

focus stack thumbnail images	focus merge option	focus merge image product	range map product	result relative to basic merge product
0819MH0003080020301504I01 0819MH0003080020301505I01	basic (merge only)	0819MH0002270000301562R00	0819MH0002270000301563S00	baseline
0819MH0003080020301506I01 0819MH0003080020301507I01	merge + blending	0853MH0004570000301966R00	0853MH0004570000301967S00	fewer seams
0819MH0003080020301508I01 0819MH0003080020301509I01	merge + registration	0853MH0004570000301968R00	0853MH0004570000301969S00	no difference
0819MH0003080020301510I01 0819MH0003080020301511I01	merge + blending + registration	0853MH0004570000301970R00	0853MH0004570000301971S00	fewer seams

high surface relief example — Sol 815 rock target named Jail Canyon — working distance ~ 7.1 cm

focus stack thumbnail images	focus merge option	focus merge image product	range map product	result relative to basic merge product
0815MH0002970020301387I01 0815MH0002970020301388I01	basic (merge only)	0815MH0003690000301493R00	0815MH0003690000301494S00	baseline
0815MH0002970020301389I01 0815MH0002970020301390I01	merge + blending	0853MH0004570000301972R00	0853MH0004570000301973S00	fewer seams
0815MH0002970020301391I01 0815MH0002970020301392I01	merge + registration	0853MH0004570000301974R00	0853MH0004570000301975S00	no difference
0815MH0002970020301393I01 0815MH0002970020301394I01	merge + blending + registration	0853MH0004570000301976R00	0853MH0004570000301977S00	fewer seams

For this test, we selected two previously-acquired focus stacks that capture the range of typical Mars geologic cases: a target of low surface relief and a target of high surface relief relative to the depth of field at a given working distance. The low surface relief example was an 8-image focus stack acquired on Sol 819 (25 November 2014) of a rock target named Mescal (**Table 11**). When the basic (merge only) focus merge was performed on Sol 819, the range map product had a narrow DN range (123–155), reflecting its low surface relief. That is, only 3 of the 8 images in the stack were actually merged. The high surface relief example was an 8-image stack acquired on Sol 815 (21 November 2014) of a rock target named Jail Canyon (**Table 11**). When the basic (merge only) focus merge was performed on Sol 815, the range map had a wide DN range (26–255), as all 8 of the focus stack images were merged.

In both cases, our Sol 853 test performed three additional merges on the same two sets of eight images (**Table 11**): merge + blending, merge + registration, and merge + registration + blending. The result, for both the low and high surface relief cases, was that performing image registration had no effect on the outcome relative to the basic (merge only) option, and blending resulted in products that were somewhat more seamless (**Figure 21**). While blending produces a slightly, aesthetically better product than the basic (merge only) case, the operation takes

twice the time (and power) of the basic merge. The trade between doubling the onboard computation time and the scientific return of the blended relative to basic product is one that the MSL Science Team will consider for future onboard focus merges, but, generally, the basic (merge only) option will continue to be favored because the difference in scientific utility of the merged products are negligible.

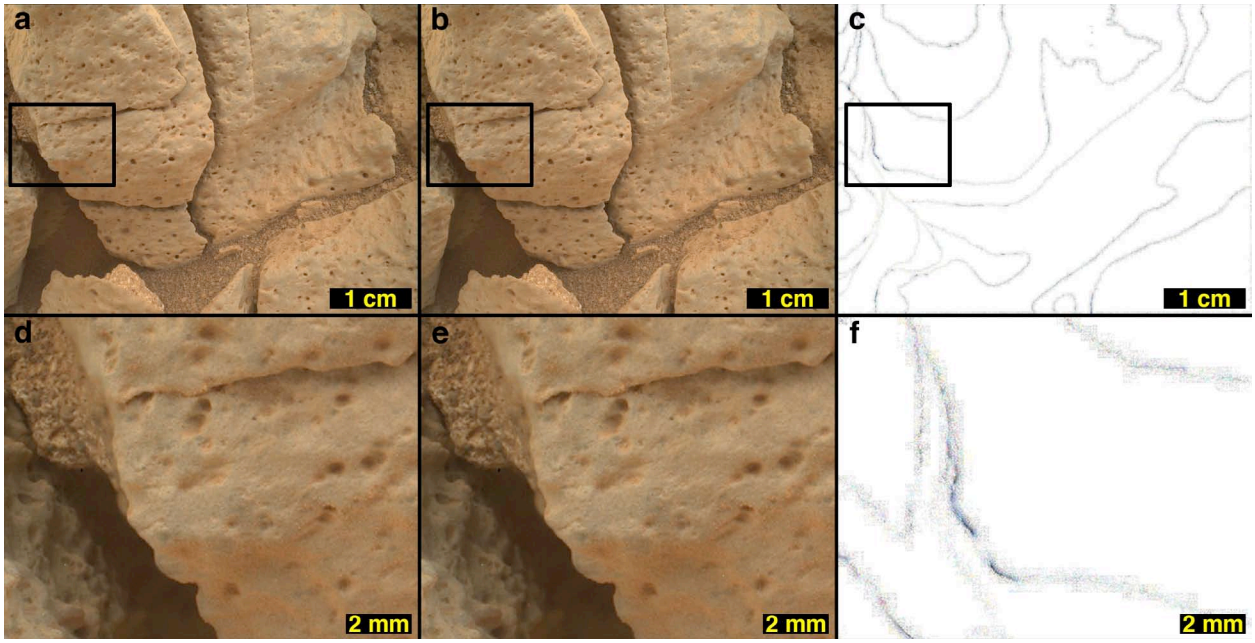

Figure 21. Example results from Sol 853 focus merge test for the high surface relief target, Jail Canyon, for which the focus stack was acquired on Sol 815. **(a)** Basic (merge only) focus merge product 0815MH0003690000301493R00; **(b)** merge + blending image product 0853MH0004570000301972R00; **(c)** dark spots indicate locations in which the basic and blended products differ. The black rectangle indicates the location of the sub-frame magnified 4x in the bottom row; **(d)** basic (merge only) focus merge image product; **(e)** merge + blending image product; **(f)** dark spots indicate locations in which the basic and blended products differ.

6.3.6 Individual focus stack images received on Earth

Downlink of the individual images of a given focus stack acquired by MAHLI provide the data user with options to calibrate each individual image before performing a focus merge and apply any desired focus merge algorithm available now or in the future. If the individual frames are returned in uncompressed or lossless compressed form, then the user also has the option to apply any desired Bayer color interpolation software.

In most cases for which individual focus stack images have been received on Earth, we carefully selected them using the information contained in the range map as to which images were actually merged. Owing to previously unanticipated downlink data volume availability, for the period from Sol 46 to 487, we were able to downlink all of the individual images, in lossless or uncompressed form, that participated in each focus merge. After that time, since January 2014, receipt of individual focus stack images has been extremely limited, owing to competition for downlink data volume with other mission science goals and priorities.

7 Geometric characterization

We required and designed the MAHLI lens such that the images exhibit almost no distortion (Ghaemi, 2009). One can observe the undistorted nature by examining MAHLI images of grid targets like those acquired on 17 September 2008 (images CAL_MH0809620000000631B00 – CAL_MH0809620050000636B00). These data show that the grid spacing and shape does not change anywhere in the field of view. A more sophisticated approach to geometric characterization involves determination of the instrument's camera model.

A geometric camera model is a set of equations that transform a 3D point in space to a 2D position in an image (pixel location). The model can also be inverted to transform a pixel in the image to a set of points in space that would map to that pixel. The model contains the camera position and pointing vector, it also models lens distortion and the interior geometry of the instrument. A camera model facilitates accurate monoscopic and stereoscopic measurement of points in an image or images, precise mosaicking of images, and creation of linearized (*i.e.*, geometrically corrected) products for which lens distortion has been removed (**Section 10.5**).

Our team developed two camera models for MAHLI. We describe the first in detail, the second briefly. The first is a four vector photogrammetric model produced at MSSS that we routinely apply to create MAHLI geometrically corrected archival data products (**Section 10.5.2**). The second is a six-vector CAHVOR model produced at JPL-Caltech to support rover operations; the CAHVOR parameters are reported with all of the MAHLI images archived with the PDS *except* the geometrically corrected products (**Section 10.5.1**). Mathematically, the two models are equivalent. The CAHVOR acronym refers to the vectors which permit transformation from object to image coordinates: the C is the camera center vector, A the axis, H the horizontal, V the vertical, O the optical, and R the radial distortion vector (Yakimovsky and Cunningham, 1978; Gennery, 2001; Di and Li, 2004).

7.1 MSSS-produced camera model

7.1.1 Data

To fit a photogrammetric camera model to the MSL MAHLI, we acquired a suite of images that have known object space (3D) coordinates for a set of points captured in the images. The 2D image space coordinates corresponding to the points were measured as accurately as possible and we used a nonlinear weighted least squares algorithm to determine the set of parameters that minimize the difference between the 3D points projected into the image using the camera model and the points measured from the image.

The data we examined were acquired during ATLO testing on 7 December 2010. For this activity, we had Curiosity's robotic arm point MAHLI downward at a stand on which were placed a succession of planar dot targets located at increasing working distances between 2.5 and 100 cm. The images, distances, and target details are in **Table 12**. We found that images acquired at five of the six positions over the 2.5–100 cm range were useful for geometric calibration; the sixth had too few dots in the image.

7.1.2 Analysis and outputs

We determined and correlated the center pixel location for each dot in the five dot target images (**Table 12**) with the position of that point in the rover reference frame (determined by JPL-Caltech engineers who surveyed the location of the four corners of each target). Following the procedure described by Mikhail *et al.* (2001), we imported these data into a universal nonlinear least squares (NLS) algorithm to determine, by NLS fit, the exterior parameters (target positions and orientations), interior parameters (focal length and detector geometry), and lens distortion coefficients. As part of the NLS calibration, we added additional parameters to adjust the position and orientation for each of the targets. The position for the farthest target was not adjusted so as to fix the scale of the system. We ran a single optimization that used data from all five calibration images (**Table 12**) to model the effect of focus motor count where needed. Further description and the outputs of the NLS program are in **Supplement S07**.

Table 12. MAHLI geometric calibration images and targets

images used for the MSSS camera model analysis (image ID)	intended working distance (cm)	dot target properties				image motor count	working distance via[1] target (cm)	notes[2]
		dot	back-ground	diameter (cm)	pitch (cm)			
ATL_MH1012030020000215B00	~2.5	black	white	0.01	0.10	15347	2.4	position inferred
ATL_MH1012030040000217B00	~5.0	black	white	0.01	0.10	14407	4.9	position measured
ATL_MH1012030060000219B00	~10	white	black	1.27	2.54	13673	10.1	insufficient dots, not analyzed
ATL_MH1012030090000222B00	~25	white	black	1.27	2.54	13054	25.2	position measured
ATL_MH1012030110000224B00	~50	white	black	1.27	2.54	12846	48.0	position inferred
ATL_MH1012030130000226B00	~100	white	black	2.54	5.08	12643	98.0	position measured

Images used for JPL-Caltech CAHVOR analysis, in addition to the six above	
ATL_MH1012020060000195B00	ATL_MH1012020150000204B00
ATL_MH1012020090000198B00	ATL_MH1012020200000209B00
ATL_MH1012020120000201B00	ATL_MH1012020230000212B00

[1]Working distance computed from pixel scale measured from image of the dot target.
[2]Target position was known (measured) or inferred by interpolation between measurements; one target had too few dots in the field of view.

7.1.3 Results

In this section, we use the term *focal length* to refer to the value of a theoretical, ideal camera without distortion; this differs from the physical, effective focal length (f_e) determined by lens design. Focal length, here, is modeled as a linear function dependent on the focus motor count (f_m). The linear effect of motor count on focal length is referred to as the focus factor (f_f) and has units of millimeters of focal length per focus motor count. The function is:

$$f_m = f_{13000} + f_f\,(m_{open} - 13000), \qquad (7)$$

in which f_{13000} is the focal length at $m_{open} = 13000$. The value of 13000 is arbitrary; we selected it because it is between the minimum and maximum m_{open}. The values we derived from the NLS procedure for f_{13000} and f_f are 20.0174 and –0.0019263, respectively.

As there are no intentional fiducial markers in MAHLI images, we define the image focal plane coordinate system (x, y) as having its origin at the principal point; that is, the location at which the optical axis intersects the focal plane. This is defined in terms of millimeters with the x direction to the right (increasing columns) and the y direction up (decreasing rows). The boresight is the same point as defined in pixels (i, j). Relative to the upper left MAHLI CCD pixel, defined as pixel 0, 0, the MAHLI boresight is located at pixel i_0 = 835.9687 (column), j_0 = 611.7417 (row).

Radial distortion is measured in the focal plane relative to a point in the focal plane called the *center of distortion*. Here we assumed that the center of distortion is equal to the principal point. Given r, the distance in millimeters of a point (x, y) in the focal plane from the principal point (x_0, y_0) for an ideal camera with no distortion,

$$r = ((x–x_0)^2 + (y–y_0)^2)^{0.5}, \quad (8)$$

then the radius for the actual camera with distortion is:

$$r' = r\,(1 + k_1r^2 + k_2r^4 + k_3r^6). \quad (9)$$

We found the following values for the distortion coefficients: k_1 = 8.72826e^{-5}, k_2 = –1.021e^{-6}, and k_3 0 (the value of k_3 is not statistically significant and thus is taken to be 0).

The mapping of points from the focal plane coordinate system (x, y), in millimeters, to the image coordinate system (i, j), in pixels, is defined as an affine transformation in which:

$$i = i_0 + a_{11}x + a_{12}y, \text{ and} \quad (10)$$

$$j = j_0 – a_{12}x – a_{22}y, \quad (11)$$

for which (i_0, j_0) is the boresight pixel. The affine coefficients (in pixels per millimeter) determined by our analysis are: a_{11} = 135.1351, a_{12} = –0.03292, a_{21} = –0.03288, and a_{22} = 135.15268. As the focal length is confounded with pixel pitch, the value of a_{11} is set to the number of pixels on the array per millimeter and was not adjusted during the analysis. Note that this indicates that the pixels may be slightly non-square or that there may be a slight misalignment with the focal plane. This is something to be expected with any camera.

7.1.4 Summary and limitations

Table 13 summarizes the calibrated coefficients for MAHLI lens distortion and interior orientation. **Section 10.5.2** describes how this model is applied to geometrically corrected MAHLI archival products. This camera model currently has the following limitations:

1 The movement of the principal point and the camera center due to focus motor count have not been modeled.

2 The center of distortion might be offset from the principal point.

3 The change in lens distortion parameters due to motor count/working distance has not been investigated nor modeled.

4 The effect of Martian environment temperatures on camera model parameters has not been investigated.

5 How well the linear model applies to focal length at minimum working distance and at infinity has not been investigated.

Table 13. MAHLI MSSS-produced camera model coefficients

lens distortion coefficients					
k_1		k_2		k_3	
$8.72826e^{-5}$		$-1.021e^{-6}$		0	
interior orientation coefficients					
boresight (pixel location)		**affine coefficients (pixels per mm)**			
i_0 (column)	j_0 (row)	a_{11}	a_{12}	a_{21}	a_{22}
835.9687	611.7417	135.1351	–0.03292	–0.03288	135.15268

7.2 JPL-produced camera model

As with the MSL Navcam and Hazcam instruments (Maki *et al*., 2012), a CAHVOR camera model was produced for MAHLI at JPL-Caltech to support Curiosity rover operations. The calibration effort followed the procedure described by Yakimovsky and Cunningham (1978) as modified by Gennery (2001, 2006) and used the same targets that were set up in December 2010 for the MSL Navcam and Hazcam calibration effort (Maki *et al*., 2012). The data analyzed include the five MAHLI images acquired on 7 December 2010 examined for the MSSS-produced model, above, as well as six additional images of other targets listed in **Table 12**. The derived model coefficients were not made available to us, however the CAHVOR parameters for each image accompany each of the archived MAHLI data products, except for the geometrically corrected product, as described in **Section 10.5**.

8 Image detection characterization

8.1 Detector and system-level image detection

8.1.1 Detector selection

MAHLI was one of several camera systems MSSS developed in 2004–2011 for the MSL project. In addition to the aforementioned MAHLI, MARDI, and fixed focal length Mastcam-34 and Mastcam-100, MSSS built a pair of zoom lens Mast Cameras (which are not aboard MSL), a MAHLI mechanism life test unit (later refurbished to become the testbed-MAHLI used by Curiosity's testbed rover at JPL-Caltech), and attendant engineering model cameras (Malin *et al*., 2009; Ghaemi, 2009; Malin *et al*., 2010; Edgett *et al*., 2012).

We selected 16 KAI-2020CM CCDs from a lot purchased for the MSL effort to be candidates for integration with the flight unit cameras. Our selection was based on manufacturer-provided data describing the voltage requirements and the fact that each had minimal defective pixels. We subjected these 16 detectors to bench-level, ambient and 160 hours at 125°C testing to qualify

them for spaceflight and rank them, in a relative sense, with regard to their performance. Ultimately, the detector we selected for the flight MAHLI was one called k7026. It exhibited only three poorly performing pixels (see **Supplement S08**).

8.1.2 System gain, full well, read noise, linearity, and signal processing

We characterized the gain (electrons, e^-, per DN), read noise (e^-), and full well capacity (e^-) of the MAHLI signal chain by imaging a diffuse illuminated integrating sphere target, with the instrument dust cover open, and by subsequent analysis of photon transfer curves using the technique described by Janesick *et al.* (1987). The uncompressed (16-bit) image data were acquired at room temperature in a cleanroom laboratory setting on 19 September 2008. We obtained pairs of images at exposure durations of 0, 5, 10, 20, and 50 milliseconds at each lamp current of 0.5 amp increments between 0.0 (dark) and 8.0 amps. The photon transfer curve is shown in **Figure 22a**. Note that these results (gain 16.18 e^- per DN, read noise 17.91 e^-, full well 27948 e^-, linearity r^2 goodness of fit 0.9996) are revised relative to the reporting by Edgett *et al.* (2012). **Figure 22b** demonstrates the linear response of the MAHLI detector; these are from MAHLI images (dust cover open) of a diffuse illuminated integrating sphere target acquired at room temperature in a cleanroom laboratory setting on 15 September 2008.

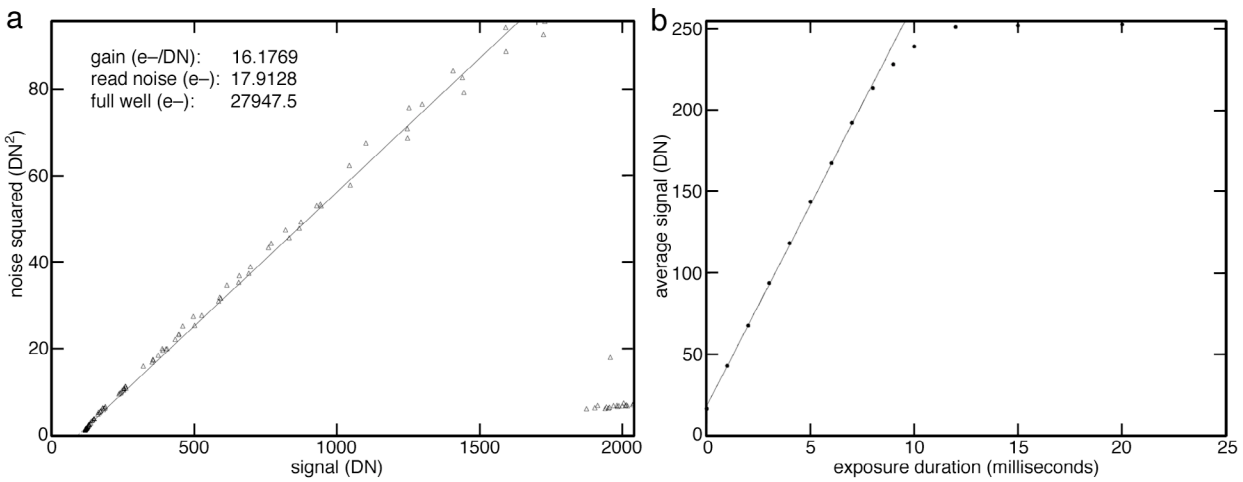

Figure 22. (a) MAHLI photon transfer curve and derived gain, read noise, and full well parameters from analysis of images CAL_MH0809740140000944A00 through CAL_MH0809741940001124A00. **(b)** Demonstration of MAHLI detector linearity, r^2 goodness of fit 0.9996, derived from 8-bit companded raw images, of exposure durations 0–20 milliseconds from images CAL_MH0809180010000002B00 through CAL_MH0809180150000016B00. The plotted data are in **Supplement S09**.

8.1.3 Dark current and bias

Dark current is the accumulation of charge within the detector from non-photoelectric phenomena, mostly thermally generated electrons. We planned that typical MAHLI camera head operations on Mars would occur at temperatures in the –40°C to +40°C range (Edgett *et al*., 2012). Indeed, between Sols 1 and 842 (> 1 Mars year), the camera head operated at temperatures between –34°C and +31°C. Under these conditions, MAHLI exhibits negligible dark current for < 100 millisecond exposures (**Figure 23**). Note that the dark bias is a noiseless DC offset in the signal level; based on the plot in **Figure 23a** it was taken to be a 12-bit DN value of ~120. We remove this bias onboard the instrument during companding; the value (commonly 120) is reported in the image header.

Figure 23a was derived from data collected during instrument thermal vacuum testing, starting with image TVC_MH0809170050000237B00 (10 September 2008, 17:17:51 UTC) and ending with TVC_MH0809170060001122B00 (11 September 2008, 15:44:00 UTC). During this period, the camera acquired 1-second exposure dark images over a temperature range between –60° and +60°C (see **Supplement S09**).

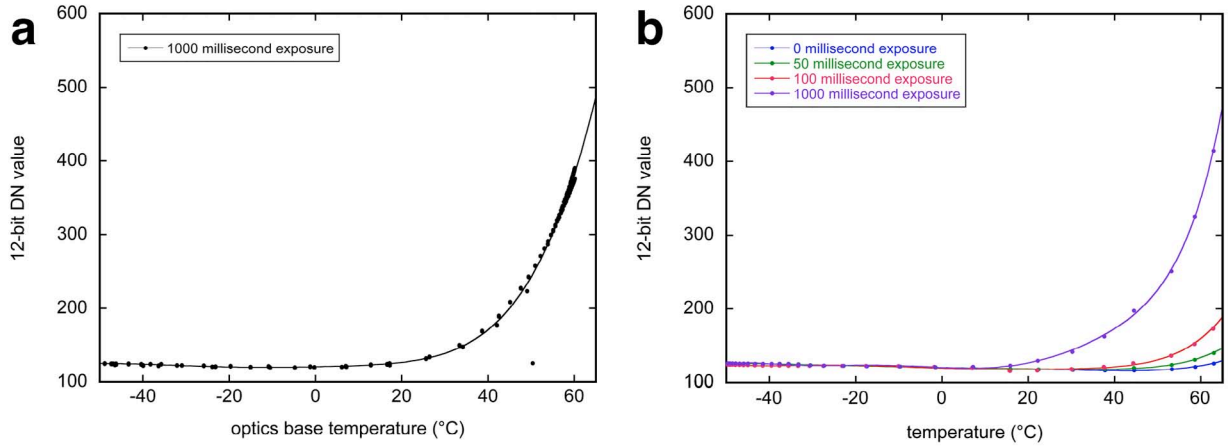

Figure 23. (a) 1000 millisecond exposure MAHLI dark current expressed as normalized signal level as a function of temperature. Note that this has a noiseless DC offset component and a dark current component, with the latter much more significant. The signal level was measured in a 500 by 500 pixel window with upper left corner at column 100, row 100 using the September 2008 thermal vacuum test 1-second exposure dark images between TVC_MH0809170050000237B00 and TVC_MH0809170060001122B00. **(b)** MAHLI dark current of 0–1000 millisecond exposures expressed as averages of dark pixels in columns 9–16 for September 2008 thermal vacuum test images TVC_MH0809150000000073A00 through TVC_MH0809150040000227B00. The temperatures and plotted data are available in **Supplements S10 and S11**.

Figure 23b shows the basis of our dark current mitigation approach described in **Section 10.3.3**. We developed a method that uses the masked dark pixels in columns 9–16 of the CCD (in which the pixel at the upper left of the CCD is at row 0, column 0) to estimate and remove dark current effects from the images. These pixels accumulate the same dark current as the photoactive pixels in a given image and thus provide a measure of dark current, as translated to image DN, for any full-frame or sub-framed MAHLI image that includes them. To determine the relationships in **Figure 23b**, we examined 155 consecutive images obtained on 09 September 2008 during thermal vacuum testing (images TVC_MH0809150000000073A00 – TVC_MH0809150040000227B00). The first images were acquired at a temperature of +60° and the last were obtained at –53°C (see **Supplement S09**). Between these extremes, the temperature fell as the camera acquired 31 sets of five images: 16-bit dark frames at 0, 50, and 1000 millisecond exposure, one 8-bit image at 100 millisecond exposure with the white LEDs on, followed by a 100 millisecond 8-bit dark frame. Because we only examined the dark column pixels, the fact that the LEDs were on for 31 of the images is irrelevant. The 8-bit images were decompanded to 16-bit. For each of the 155 images, the dark pixels in columns 9–16 were averaged to yield a single 16-bit image DN.

From the above analyses, **Figure 24** shows the average change in 16-bit DN per second exposure duration (DN_{exp}) versus temperature, T (in °C). For T between –60°C and +60°C, this relationship can be expressed as:

$$DN_{exp} = a + bT + cT^2 + dT^3 + eT^4 + fT^5 + gT^6, \quad (12)$$

in which a = 3.0968×10^{-3}, b = 1.6438×10^{-4}, c = 2.6854×10^{-6}, d = 2.2087×10^{-7}, e = 7.8154×10^{-9}, f = 5.5034×10^{-11}, and g = -2.6914×10^{-13}.

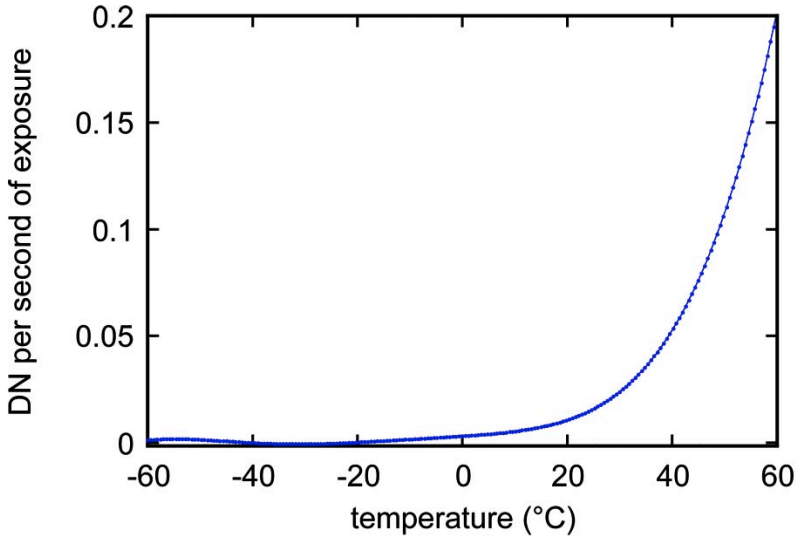

Figure 24. Dark current expressed as 16-bit DN per second of image exposure, as a function of temperature, derived from the data examined in **Figure 23**. The plotted data are available in **Supplement S12**.

8.1.4 Particulates on the detector

MAHLI images exhibit dark spots that result from the presence of tiny particles on the CCD (**Figure 25a**). They were accidentally introduced during camera head assembly. Initially, a few relatively large, opaque flakes appeared in images acquired on 20 August 2008 during camera development (*e.g.*, image DEV_MH0808050000000336B00). This occurred after we opened the camera head to adjust the lens to improve focus at infinity. We opened the camera head again on 25 August 2008 and painstakingly removed these particles. However, a few small flakes remained (*e.g.*, image DEV_MH0808120000000444B00).

Images acquired on 03 September 2008, after the camera head underwent random vibration testing, showed that many more, very small, opaque to transparent particles were deposited on the CCD (*e.g.*, image DEV_MH0809010150000506B00). A few additional particles appeared after delivery to JPL-Caltech (*e.g.*, image DEL_MH0810040000000007B00), but no new particles appeared, nor did any previous particles move, after more than two years of storage, installation on the rover (*e.g.*, see image ATL_MH1011020010000022B00), rover ATLO activities which included vibration and environment chamber testing (*e.g.*, see ATL_MH0080040010000737B00), transport from California to Florida (*e.g.*, see ATL_MH0090060010001367E01), drill and CHIMRA testing, launch, interplanetary cruise, landing on Mars (*e.g.*, image 0001MH0000000020100002C00), and hundreds of sols of surface operations, including driving, drilling, and CHIMRA operations (*e.g.*, see 0828MH0004530000301722C00).

The locations of the dark spots can be seen in NASA PDS archived flat field products (*e.g.*, FLAT_MH_0.IMG). We also show their generalized (albeit imperfect) locations in **Supplement S13**. Since early 2014, we have been using the **Supplement S13** product as a reference for quick, manual removal of the spots from MAHLI images.

The particles on the CCD do not negatively impact the scientific utility and interpretability of the images and they are readily removed by image processing. We actually have found the larger

dark spots to be useful as unintended fiducial or reseau marks. That is, for repeated images of the same target observed from the same working distance on different occasions, we have used them to measure the offset, relative to planes parallel to that of the CCD, of the repeatedly imaged target. An example of this is the robotic arm repeatability test conducted at the rock named Jake Matijevic on Sols 46 and 47 described in **Section 5.4**.

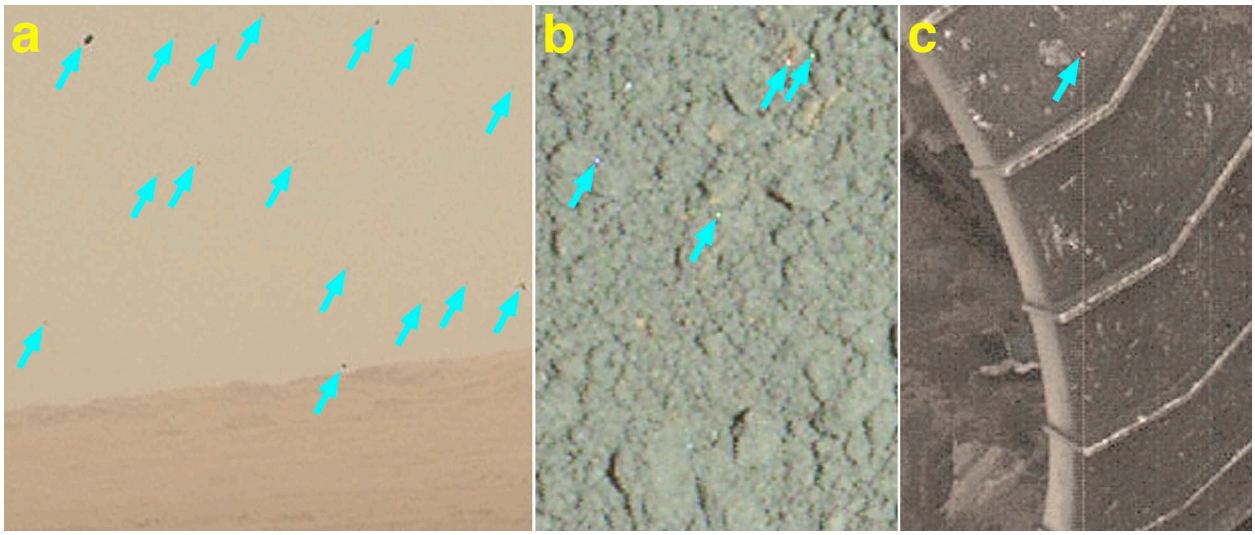

Figure 25. Example blemishes in MAHLI images received from Mars. **(a)** Dark spots (arrows) occur in all MAHLI images acquired since 20 August 2008 and are the result of tiny particles present on the CCD. These were introduced during camera head assembly; the image is a sub-frame of 0356MH0003050000104168E02 acquired on Sol 356 (06 August 2013). **(b)** Stuck, hot, or abnormally sensitive pixels (arrows) are brighter than the majority of pixels and are especially evident at > 0°C temperatures and/or as exposure duration increases; this is a sub-frame of image 0628MH0004080020203617C00 acquired at night to show drill hole cuttings with the group 2 white LEDs on. **(c)** Abnormally bright pixels in MAHLI images can lighten the pixels in the same column (bright spot at arrow and bright line below it) at rows greater than the row in which the bright pixel occurs; this is a CCD read-out effect. The example is a sub-frame of 0529MH0002630000201146E01 (Sol 529, 31 January 2014); it shows a portion of the rover's left center wheel.

8.1.5 Defective or damaged pixels

In addition to the particulates on the detector, the MAHLI CCD exhibits other defects that are manifest as a function of temperature and/or exposure duration. In particular, and using the definitions of Ghosh *et al.* (2008), stuck, hot, and abnormally sensitive pixels can be observed in MAHLI images (**Figure 25b**). Some of these can brighten the pixel column with increasing row—this is an artifact of CCD read-out of the hot pixel (**Figure 25c**). At installation, the MAHLI CCD had only 3 off-nominal pixels (**Section 8.1.1**); the pixels rendered defective since installation might result from radiation damage, including the effects of the radiation environment during spacecraft cruise to Mars, radiation that reaches the surface of Mars, plus there are two onboard energetic particle sources, the Multi-Mission Radioisotope Thermoelectric Generator (MMRTG) and the DAN instrument. The MMRTG is a constant source of low flux neutrons (Carr *et al*., 2012), and the DAN includes an active, pulsed neutron generator (Mitrofanov *et al*., 2012). Some of the problem pixels can self-heal, while others can persist indefinitely. Depending on the severity of problem pixels, investigators can perform adjustments during image processing on Earth. One way to be certain that a given pixel is damaged is to compare multiple MAHLI images of different targets acquired on the same or neighboring sols; those pixels which are persistently abnormal are those that are stuck, hot, abnormally sensitive, or obscured (or partially obscured) by particulate debris.

8.1.6 Imaging the sun

As a matter of conservative best practice, we do not intentionally image the sun with MAHLI. The KAI-2020CM interline transfer CCD can be vulnerable to damage when imaging a bright source such as the sun (Truesense, 2013). Owing to MAHLI's relatively slow focal ratio (f/8.5 at infinity focus), the likelihood of damage is low. Our testing showed no damage to KAI-2020CM detectors at f/4, detectable damage (visible in dark current frames but no affect on image quality) at f/2.8, and significant damage (visible artifacts in images) at f/1.4. Conservatively, considering f/4 to be the threshold at which damage begins to occur, MAHLI at infinity focus has at least a 4.5x margin against damage when imaging the sun from Mars.

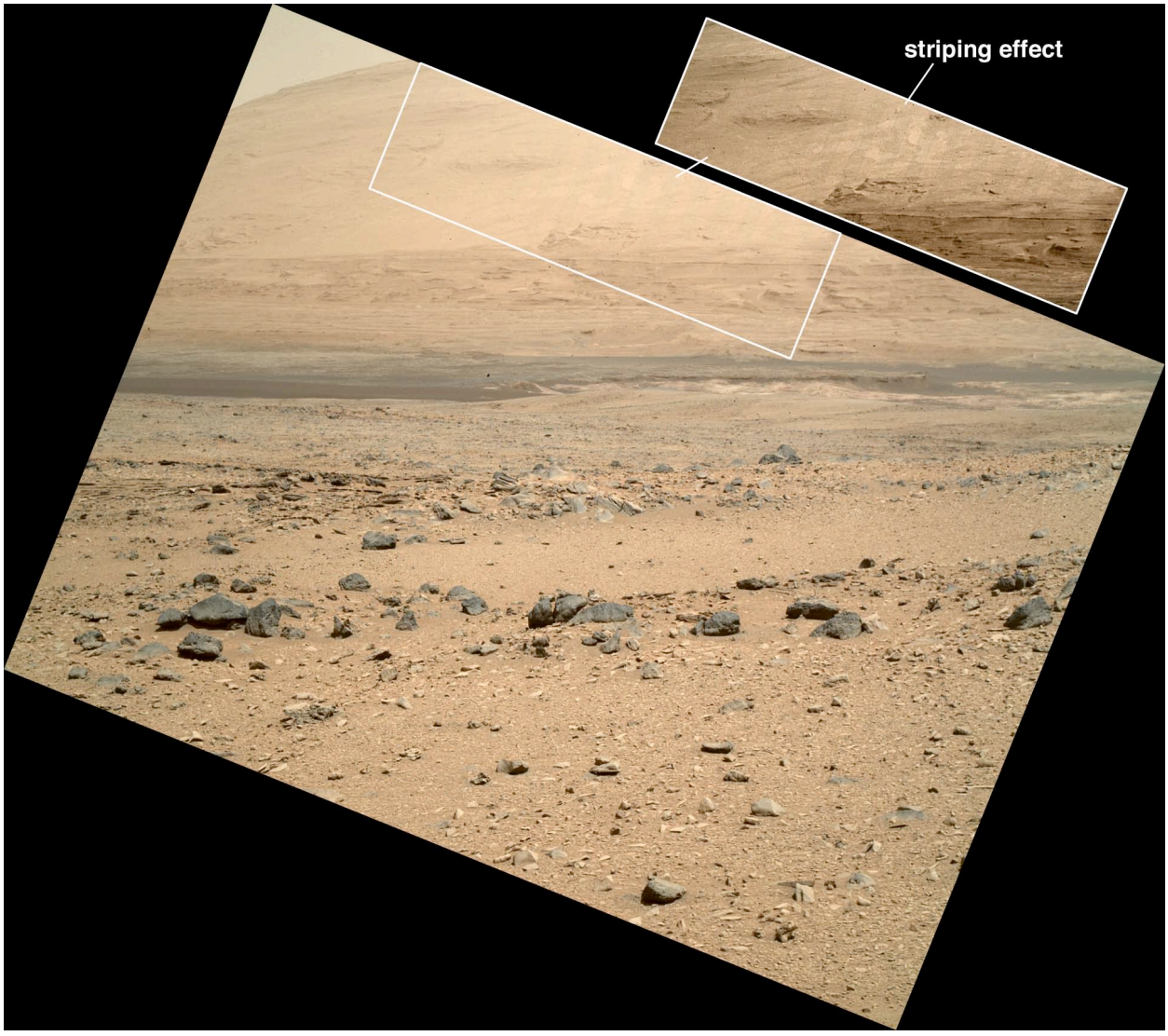

Figure 26. Example of vertical striping effect that occurs in some MAHLI images, particularly in portions of an image near saturation. Note that the image has been rotated 202° clockwise relative to the as-received product. This is MAHLI image 0327MH0003050000104151C00, a view looking southeastward at the north slope of Aeolis Mons (Mt. Sharp) on 08 July 2013.

8.1.7 Vertical striping effect

Figure 26 shows an example of an artifact that occurs in some MAHLI images in cases for which a portion of the image is at or near saturation. The CCD manufacturer described the problem, called *vertical striping*, as a matter of alignment of vertical clock pulses (ON Semiconductor, 2014). The effect is particularly pronounced in MAHLI images relative to data from the electronically identical MSL Mastcam and MARDI instruments, owing to MAHLI's lower data rate (5 megabits per second) between the camera head and DEA through the 12.7 meters-long cabling that connects them (see Edgett *et al*., 2012). We usually avoid introduction of these artifacts by acquiring images that are not at or near saturation.

8.2 Bandpass and spectral throughput

8.2.1 Lens and dust cover transmission

MAHLI lens transmission as a function of wavelength is the composite of light passing through the lens element glasses, antireflective coatings, and an infrared cutoff filter. Transmission is nearly flat and occurs between 394 and 670 nm (**Figure 27**). The Lexan™ dust cover window transmission is also flat (**Figure 27**); before it became coated with dust, it was transparent over the MAHLI spectral bandpass. The transparency of the clean dust cover is apparent in the photograph on the right side of **Figure 28**.

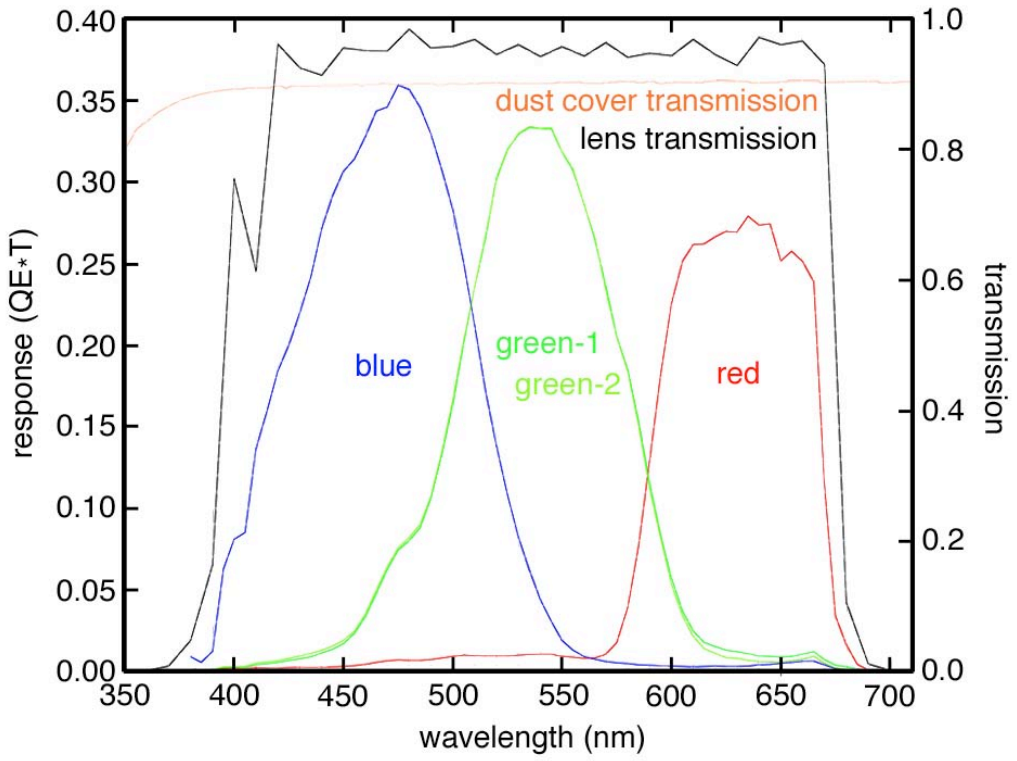

Figure 27. MAHLI lens transmission, dust cover Lexan™ transmission, and system-level red, green, and blue response (quantum efficiency, QE, times transmittance, T) as a function of wavelength. Dust cover transmission is from a witness sample. The data are in **Supplements S14–S16**.

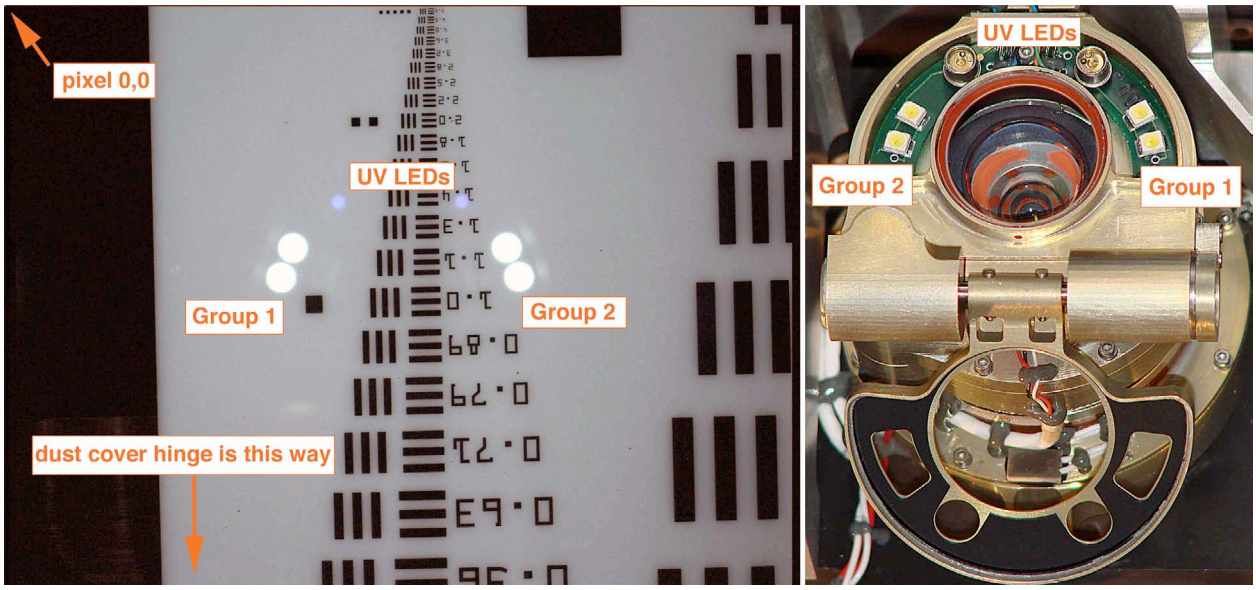

Figure 28. MAHLI image TVC_MH0809080020000032B00, left, shows the violet and white reflections of the UV and Group 1 and Group 2 white light LEDs, indicating their location in relation to the CCD's pixel at column 0, row 0. The photograph on the right shows the camera head with its dust cover open and LEDs labeled.

8.2.2 System spectral throughput

System spectral throughput, here, regards observation of the relative spectral response of the entire instrument. We only obtained measurements for the case in which the dust cover was open. The results, as a function of the CCD's four groups of micro-filters (red, green-1, green-2, and blue), are shown in **Figure 27**. To obtain the RGB measurements, we placed MAHLI before a monochromator output port, set focus at m_{open} 16000, and acquired 16-bit sub-frames (CAL_MH0809650140000659A00 – CAL_MH0809650930000738A00) that captured the monochromator output over the spectral range between 380 and 1000 nm. Each image covers a 5 nm step over the range 380–715 nm; between 750 and 1000 nm, the increments were 50 nm. We had to vary image exposure time as a function of wavelength to maintain good signal level and avoid saturation. We recorded the monochromator optical power meter (OPM) reading (in watts) at each setting (both the wavelength and power are recorded in the RATIONALE_DESC in each image .LBL (label file) in the NASA PDS archive).

From these data, we measured the average signal level in 12-bit DN for each Bayer channel (red, green-1, green-2, blue) and then computed the normalized response in DN per second per watt. However, we later found—too late to collect additional data—that the OPM values were not radiometrically relatable in an absolute sense to input flux at the camera. Thus we re-normalized the values to detector quantum efficiency (QE) from the manufacturer's data sheet (**Supplement S17**) and transmission from lens optics parts (**Supplement S14**), at the peaks of the Bayer filter bandpasses. The resulting plot (**Figure 27**) is useful to show the shape of the instrument spectral response, but it cannot be directly used for image calibration.

8.2.3 System performance

We confirmed that actual MAHLI performance meets the expectation based on lens transmission and CCD QE by imaging an integrating sphere and a calibrated Quartz Tungsten

Halogen (QTH) lamp traceable to National Institute of Standards and Technology (NIST) standards (**Supplement S18**). Using MAHLI image CAL_MH0809180170000018A00 of the integrating sphere and CAL_MH0809180180000019A00 for dark current subtraction, the observed signal level of the integrating sphere output is within 10% of prediction for all three Bayer filter bandpasses, with the actual levels slightly higher than predicted (**Table 14**).

Table 14. MAHLI signal (electrons, e–) performance as a function of Bayer red, green and blue relative to prediction (assumes lens at ~f/8.5)

band	predicted (e–)	measured (e–)	difference
red	18023	19430	-7.2%
green	13681	14181	-3.5%
blue	8431	8590	-1.8%

8.3 System flat field

Flat field products are used to account for the effects of the camera system on the image detected, including: (1) pixel-to-pixel variations in response; (2) the impact on image detection induced by the nature of the optics, focal plane assembly, and their housings; and (3) particulates in the optical path. For a spacecraft camera, it is ideal to create an initial flat field product from observations acquired before launch. In some cases, this might be the only flat field product that can ever be produced if it is difficult or impossible to obtain post-launch flat field observations. In other cases, there are methods for obtaining flat field observations in an in-flight or on the surface of a planetary body. For a camera on Mars, the latter can be performed through dedicated observations of the sky.

8.3.1 Pre-launch flat field product

The MAHLI system-level flat field product created from pre-launch data, archived with the NASA PDS as file FLAT_MH_0.IMG, was made using a single MAHLI image, CAL_MH0809770000001186B00. We acquired it on 19 September 2008 with a 50 ms exposure. **Figure 29a** provides a representation of this product. We derived it from an image of a Spectralon™ target acquired with m_{open} at 12750. Owing to the manner in which the target was illuminated by a halogen lamp, the product exhibits a horizontal gradient that is offset from the image center. In other words, the illumination was not uniform across the target but it was the best we could achieve at the time. We did not acquire additional flat field images of the Spectralon™ target at other focus (motor count) positions.

To create the product from CAL_MH0809770000001186B00, we decompanded the raw, uncompressed 8-bit parent image to 12 bits and removed dark current using the mean value for the dark columns on the left side of the image. Then we normalized the image—that is, the multiplicative array (the flat field) generated from the image was derived from the final flat field calibration image divided by the median. The CCD's red, green 1, green 2, and blue micro-filtered pixel arrays were treated independently. We applied no smoothing operators, filters, or spatial or local operators and we made no corrections to bad pixels or optical obstructions in the source image.

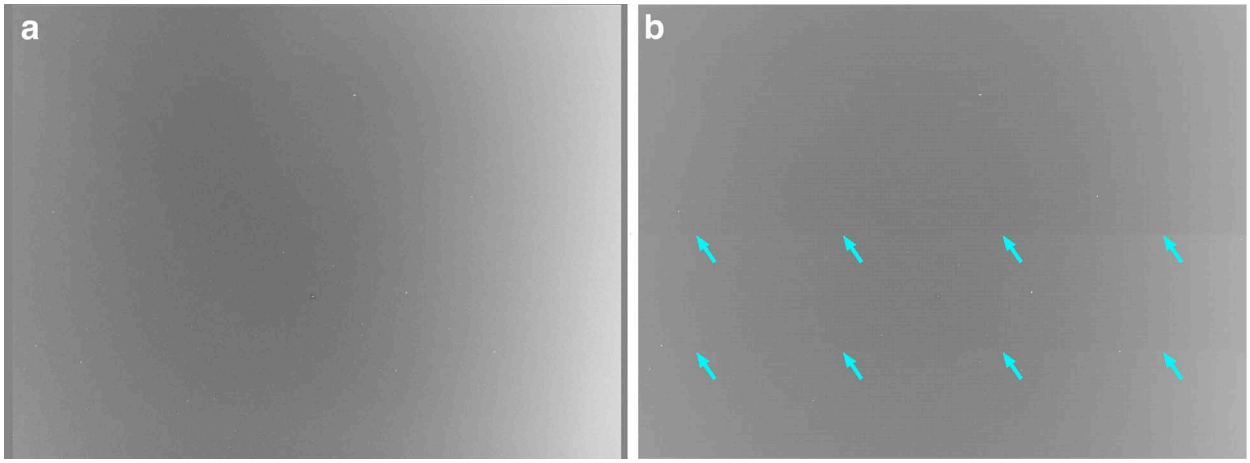

Figure 29. Example pre-launch MAHLI flat field products. **(a)** The best pre-launch product, although somewhat flawed by non-uniform illumination, was created from a single 8-bit image of a Spectralon™ target (image CAL_MH0809770000001186B00). In the NASA PDS archives, this is flat field product FLAT_MH_0.IMG. **(b)** Our attempt to create a flat field product from 16-bit sub-framed images of a uniform illumination source from an integrating sphere did not produce a viable product; the arrows indicate seams between the composited sub-frames from the data set acquired on 16 September 2008 (images CAL_MH0809220000000118B00 – CAL_MH0809220430000161A00). For illustration purposes, only, both of these figures have been contrast enhanced to show subtle details in flat field response.

Using an image of the Spectralon™ target was not our first choice for a pre-launch flat field product. Indeed, it was our backup plan. On 15 and 16 September 2008, we obtained two sets of MAHLI images of a uniform light source (emitted from an integrating sphere), images CAL_MH0809190000000033B00 through CAL_MH0809190440000077A00 and CAL_MH0809220000000118B00 through CAL_MH0809220430000161A00. The integrating sphere could not uniformly illuminate the entire MAHLI CCD, so we acquired 16-bit and 8-bit sub-frames in which we moved the camera field of view across the source until the entire detector had been illuminated, sub-frame by sub-frame, one section of pixels at time. **Figure 29b** shows the composite of the 16-bit data obtained on the second day. The results were not seamless. Compiling the 16-bit data from both days, 15 and 16 September 2008, did not improve the product and thus we abandoned the effort to produce a flat field from these data. Owing to schedule priorities, and the envisioned nominal operation of MAHLI on Mars in the dust cover open state, we did not acquire data before launch with which to create of a flat field product for the dust cover closed case.

8.3.2 Acquisition of flat field data on Mars

Given the dusty environment in which MAHLI would operate and the imperfection of the pre-launch flat field product, we were motivated to acquire data on Mars that could be used to create flat field products. Such data would improve our ability to apply flat fields to MAHLI images as a function of focus position and permit us to monitor the system for changes in the flat field, such as those that would result from accumulation of dust particles on the lens. If changes were observed, flat field products appropriate for a given period before and after the changes occurred could be applied to image calibration.

To these ends, we acquire images of the Martian sky approximately every 180 sols (**Table 4**). Applying the approach used for MER MI sky flat field observing (Herkenhoff *et al*., 2006), we work with the robotic arm operators to point the camera skyward at least 90° away from the sun

to avoid scattered/stray light in the images. Based on the model of Markiewicz *et al*. (1999), the sky brightness gradient is minimized at an azimuth 180° from the sun and about 30° above the horizon; this is the best portion of the sky to image for flat field calibration. To satisfy these requirements, sky flat images are acquired during daylight, either before 09:00 or after 15:00 local solar time. The images are obtained by pointing MAHLI in the appropriate direction, acquiring the images at each desired focus position, and then having the robotic arm move the camera to provide an effective 180° rotation about the camera optic axis (the arm cannot actually rotate MAHLI about its optic axis but the resulting camera position is as if it had been rotated). After the 180° positioning, the sky is imaged again at the same focus positions. The first set of images, then, is the 0° suite and the second set is the 180° suite; averaging the two images, 0° and 180° per focus position, effectively removes the gradient in sky brightness. The sky observations are downlinked in losslessly compressed format. In addition to the MAHLI images, we also acquire Mastcam-34 and Navcam left camera images of the same portion of the sky to confirm that no clouds are present.

Table 15. MAHLI sky flat field image focus positions

motor count	dust cover state	matching working distance	sols	notes
15996	open	2.04 cm	86, 322, 516, 653, 828	routine; matches minimum possible working distance
14664	open	3.9 cm	322, 516, 653, 828	routine; matches routine imaging at 2 cm standoff (MAHLI toolframe +X) distance
13998	open	6.9 cm	322, 516, 653, 828	routine; matches routine imaging at 5 cm standoff (MAHLI toolframe +X) distance
13320	open	15.2 cm	828	discontinued; should have been 12750
13014	open	26.9 cm	322, 516, 653, 828	routine; matches routine imaging at 25 cm standoff (MAHLI toolframe +X) distance
12972	open	29.5 cm	86	discontinued; 13014 is more representative of on-Mars camera use
12750	open	63.3 cm	future	future; to match pre-launch flat field product focus position, image CAL_MH0809770000001186B00
12600	open	230 cm	86	discontinued; 12552 is more representative of on-Mars camera use
12552	open	infinity	322, 516, 653, 828	routine; matches infinity-focused images of landscape
4488	closed	300 cm	86	indefinitely discontinued
0	closed	2.04 cm	86	indefinitely discontinued

We acquired sky flat images on Sols 86, 322, 516, 653, and 828. **Table 15** summarizes their focus positions and justification. The complete list of sky flat images and attendant camera and sun positions are listed in **Supplement S19**. Our nominal sky flat images are obtained with the dust cover open; we also acquired some with the dust cover closed on Sol 86. After our initial effort on Sol 86, we decided to change our m_{open} focus positions to match them more closely with the standard suite of geologic images we have been acquiring on Mars (**Table 15**). Most importantly, our analysis of the Sol 86 images showed us that we needed more flat field products at focus positions between the minimum working distance focus position (we use m_{open} 15996), and the mid-range position, m_{open} 12972, that we used on that Sol 86. Thus we decided to acquire sky flat images at m_{open} positions that correspond with our typical imaging at 2, 5, and 25 cm standoff (MAHLI toolframe) distances (**Table 15**). On Sol 828 we also acquired data at m_{open} of 13320, erroneously thinking that this was the focus position at which we acquired the

pre-launch Spectralon™ flat field image (it was at m_{open} 12750 and future sky flat images will use this position).

8.3.3 Mars sky flat field processing and evaluation

For a given sol's worth of sky flat images, our data processing began by confirming that there were no clouds visible in Navcam or Mastcam images, followed by decompanding the MAHLI images to 16-bit products, removal of dark current, and Bayer interpolation of the images. We then separated the interpolated, color products into red, green, and blue (RGB) images (*i.e.*, three images, one per band). Then we averaged each pair of 0° and 180° (**Supplement S19**) images to remove the sky brightness gradient. This approach assumes that the gradient is the same across the entire image; variations in sky brightness gradient (here called curvature) will introduce errors in the resulting flat field response measurements.

Figure 30 shows an example of our evaluation of variation across the detector as a function of RGB color band. We examined this profile for each averaged product from the Sols 86–828 data. In each case, and in the pre-launch flat field product, the shape of the red band profile is different than the other color bands, thus color dependence of sky brightness curvature is not the cause. Rather, the differences likely result from properties of the MAHLI optics and/or the CCD (*e.g.*, greater penetration of red light into the silicon).

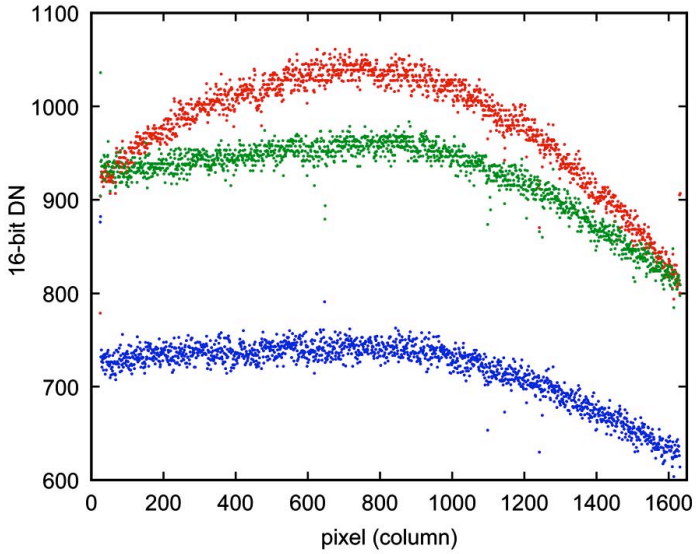

Figure 30. Example pixel value (DN) profiles across row 599 of the Sol 86 sky flat field product acquired at m_{open} 12600 (from images 0086MH0000920020101031C00 and 0086MH0000920020101036C00). Colors correspond to red, green, and blue color channels of Bayer interpolated products. These data are in **Supplement S20**.

We then evaluated flat field variation as a function of focus position for each sky flat field product. These were first normalized by dividing each by the average of the central 100 by 100 pixels in the product to allow comparison of flat field results with variable signal levels. We computed the ratios of the normalized Sol 86 dust cover open average flat fields at distant focus to the normalized averages at the other dust cover open focus positions. The flat field responses at intermediate and distant focus positions are very similar, and can therefore be easily interpolated. Similar processing of the data acquired on Sols 322, 516, and 653 yielded similar results, except near the lower left corner of each product around a circular feature (see **Section 8.3.5**). An example, from the Sol 653 sky flat data, is shown in **Figure 31**.

To seek potential changes in flat field response over the course of the mission (Sols 86–828), we compared the normalized average of sky flat products acquired on each of the sols (**Table 15**). However, differences in sky brightness curvature can also cause differences in these processed images. Thus, we estimated the magnitude of errors introduced by curvature in sky brightness by analyzing the differences between averaged sky flat products acquired on Sols 86–828 at the minimum focus position (m_{open} 15996). **Figure 32** shows that differences of a few percent are evident, and the spatial patterns in the difference images vary between sols.

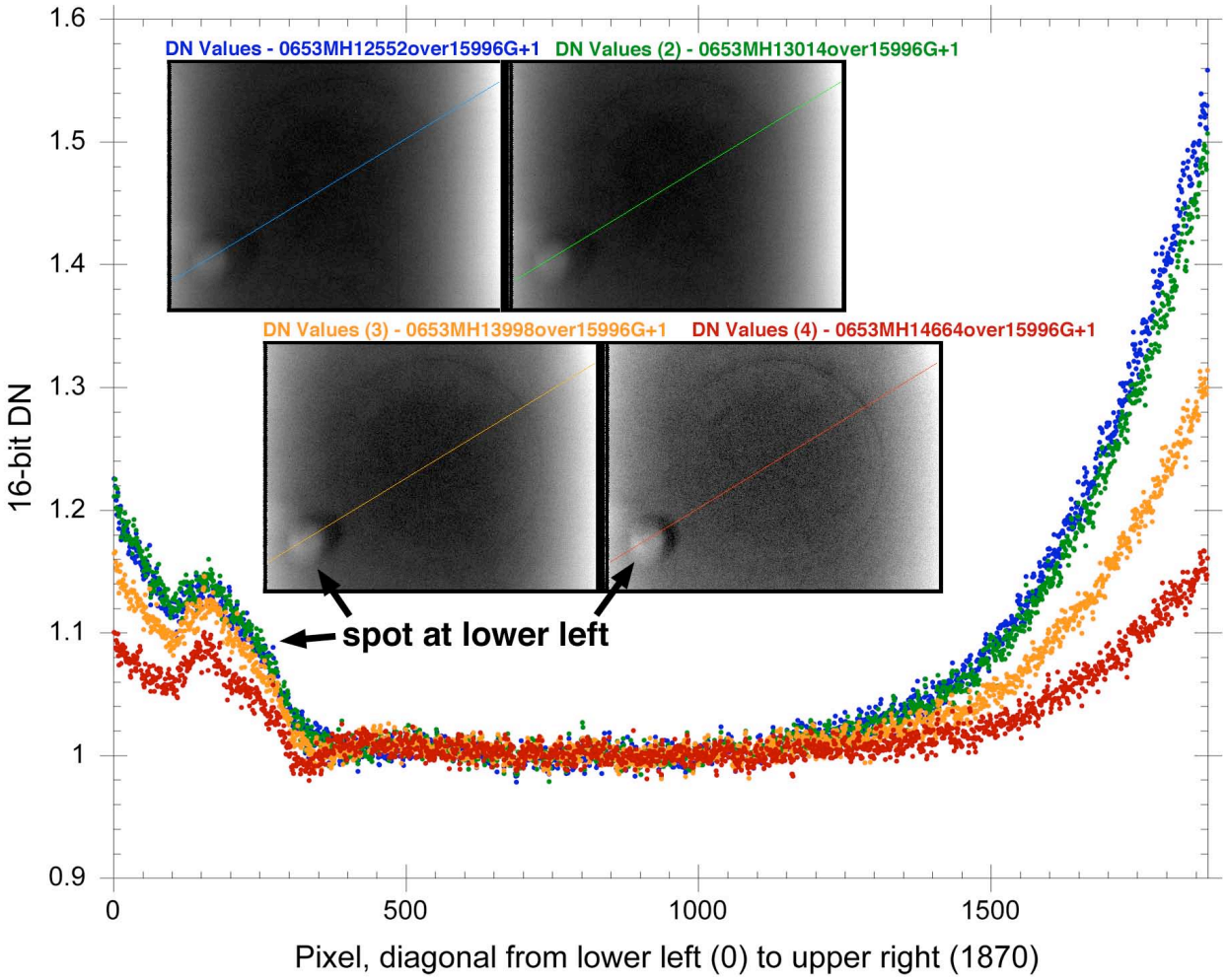

Figure 31. Example ratios of processed sky flat field products acquired at various focus positions, interpolated green band, from the Sol 653 data. Colors in the plot correspond to the colors of profiles (diagonal lines) across the ratio products. Spot at lower left is interpreted to be evidence of a grain or aggregate of dust grains on MAHLI's front lens element. The plotted data are in **Supplement S21**.

The apparent temporal variations in **Figure 32** might have been caused by changes in dust contamination on the MAHLI lens and/or changes in the curvature in sky brightness across the fields of view. From the low frequency pattern of the variations in the difference images, it seems likely that these result mainly from changes in sky brightness curvature, but we cannot completely eliminate the possibility of some dust contamination. We note that the sky flat images were not acquired in a precisely anti-sun direction (see delta azimuths in **Supplement S19**), at which the curvature in sky brightness is minimized, so some variation is expected. Indeed, differences of up to 6% are seen between sky flats acquired during the Sol 86 to 828

period (**Figure 32**), consistent with a sky brightness curvature of no more than 6% across the MAHLI field of view. Moreover, the variations in the spatial patterns in the difference images at the top of **Figure 32** are broadly consistent with the variations in pointing relative to the sun. For example, to acquire the Sol 322 and 828 sky images, MAHLI was pointed just south of the anti-sun azimuth, while for the Sol 516 and 653 sky images, the camera was pointed just north of the anti-sun azimuth. It is very unlikely that changes in dust contamination would counteract the effects of sky brightness curvature changes between these products; thus 6% is a reasonable estimate of the accuracy of this technique in measuring low-spatial-frequency flat field response variations. The effects of changes in dust contamination are not evident at this level of accuracy.

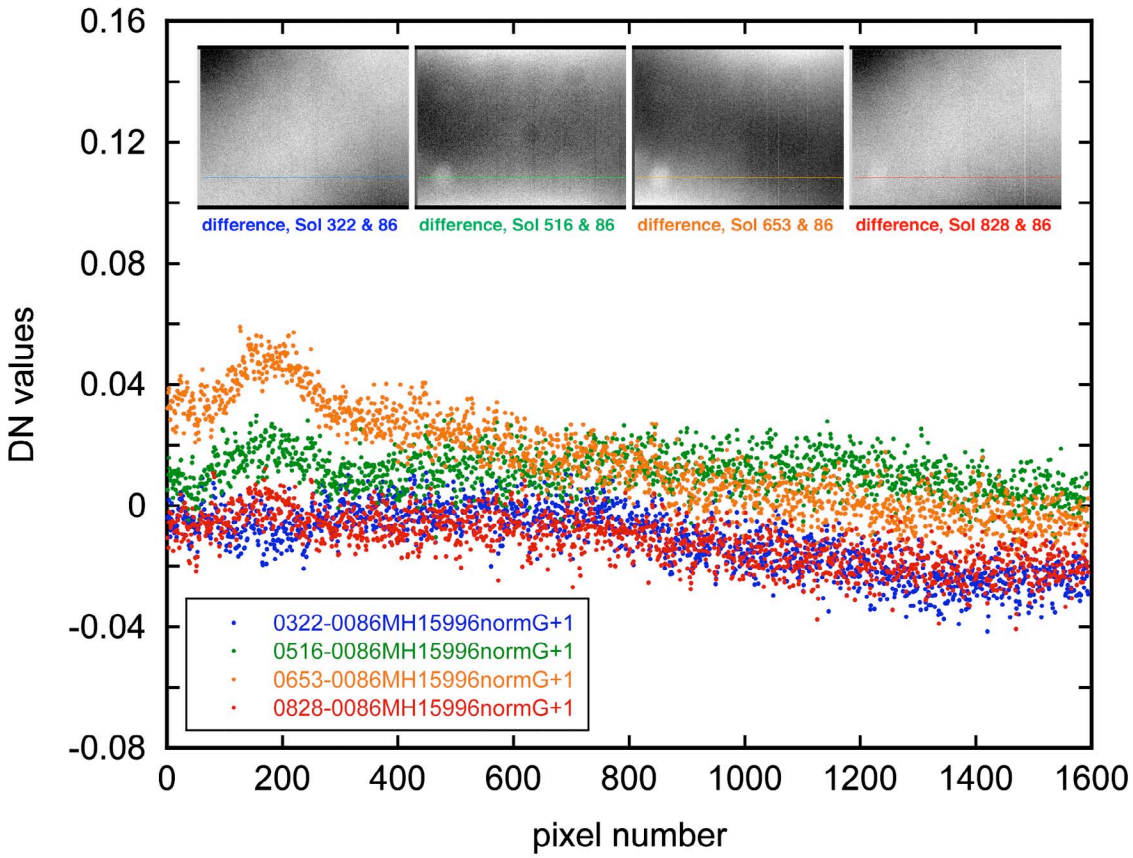

Figure 32. Example of differences between normalized MAHLI sky flat field products from images acquired on Sols 322, 516, 653 and 828 and the normalized products from Sol 86. This figure compares green band results for focus position (m_{open}) of 15996. The diffuse spot in the lower left of each image product probably results from the presence of a grain or dust grain aggregate in the optical path. The plot shows the differences along the lines drawn across each of the image products. The plotted data are in **Supplement S22**.

8.3.4 Mission (Sols 86–828) averaged sky flat field products

The sky flat products are similar from sol to sol, indicating that they can be averaged over the sols to yield higher precision ratios of flat field response at each focus position. The Sol 322, 516, 653, and 828 sky flat images were acquired at five common focus positions, m_{open} 15996, 14664, 13998, 13014, and 12552 (**Table 15**); sky flat field images were also obtained at m_{open} 15996 on Sol 86. Therefore, we averaged these flat field products across these sols to improve precision. **Figure 33** shows examples that bracket the m_{open} range between minimum working distance (m_{open} 15996) and infinity (m_{open} 12552).

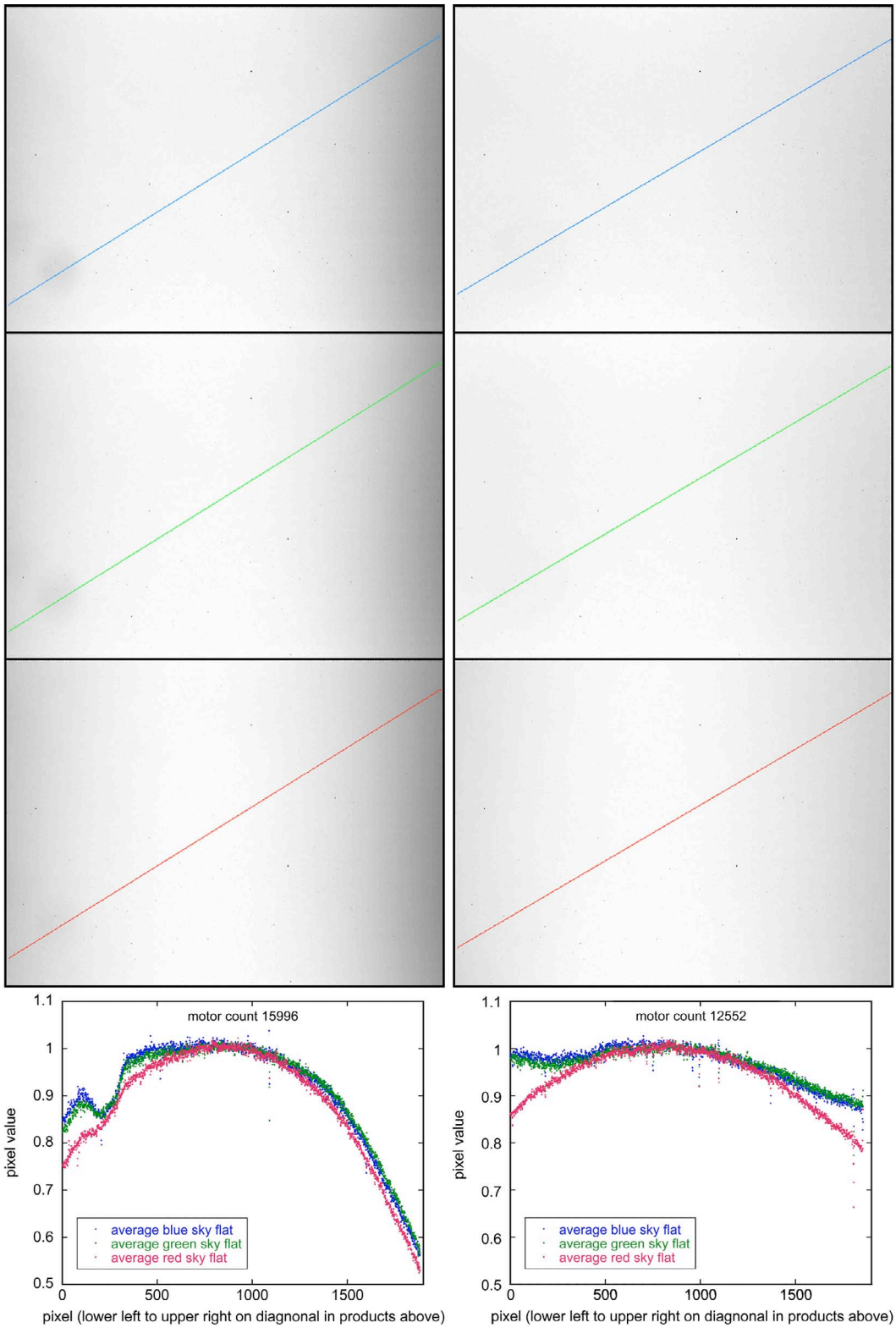

Figure 33. Averages of sky flat field red, green, and blue products acquired; the colors of the diagonal lines indicate RGB color band. **(left)** Averaged Sols 86, 322, 516, 653, and 828 products at m_{open} 15996, corresponding to a minimum working distance focus position. **(right)** Averaged Sols 322, 516, 653, and 828 products at m_{open} 12552; corresponding to an infinity focus position. The plotted data are in **Supplement S23**.

8.3.5 Persistent particulate on MAHLI lens

The sky flat field products exhibit a nearly circular feature near the lower left corner of each (**Figures 31–33**). The effect or apparent presence of this feature changes with focus position; it is more pronounced at focus positions corresponding to small working distances, and less obvious at positions corresponding to larger working distances (**Figure 33**). The feature was not present in the pre-launch flat field (**Figure 29**) and the front lens element was cleaned in August 2011, just before the rover was mated with its descent stage and placed inside the spacecraft aeroshell. The dust cover was not opened after that cleaning until Sol 33 (09 September 2012). Further, the feature is less visible in red band images and more obvious in blue and green (**Figure 33**).

All of these observations suggest that the feature observed is an object in the optical path. It absorbs more strongly at wavelengths shorter than red. The most likely explanation is that this feature results from a grain or aggregate of reddish dust grains clinging to the front lens element. The feature has been present throughout most of the mission, at least through the sky flat image acquisitions on Sol 828. It has remained on the lens despite hundreds of dust cover actuations, arm positioning of the camera and other tools, and vibration caused by drilling and sample processing and storage.

We strongly suspect that the feature is indeed a grain or aggregate of fine dust particles (examples of both are seen on the U.S. cent in **Figure 15**) and that it has been observed by Mastcam-100. Only once has the Mastcam-100 imaged the front end of the MAHLI lens when the dust cover was open; this occurred on Sol 617 (02 May 2014) during an effort to inspect the instrument after a fault left MAHLI with its dust cover open for several sols. The green arrow in **Figure 34** points to a feature observed on the MAHLI lens and its corresponding location—the circular spot—in MAHLI flat field products.

8.3.6 Pre-launch and sky flat field product assessment

The image used to create the pre-launch flat field product, CAL_MH0809770000001186B00, was obtained with MAHLI focused at m_{open} 12750. Through February 2015, we have not acquired sky flat field data at this focus position (**Table 15**). The best comparison available between the pre-launch and Mars sky flat field products, at present, is to consider the Sol 86 data obtained at m_{open} 12600 and 12972. As shown in **Figure 35**, the differences between the pre-launch and Sol 86 flat field products range up to 15% in all color bands. The differences exceed those between the two Sol 86 focus positions; similar behavior is seen when more recent sky flat field products are compared with the pre-launch flat field, as well. As the pre-flight image was of a non-uniformly illuminated Spectralon™ target, it is likely that this fact contributes to the differences observed in **Figure 35**.

The ultimate assessment of flat field products comes in the form of mosaicking images of a given target. **Figure 36** compares a mosaic of MAHLI images made using the pre-launch flat field product and the appropriate (in terms of focus motor count position) mission-averaged sky flat field product. The best performance is the most seamless mosaic; in this case, application of the sky flat field created the more seamless product, consistent with the 6% relative radiometric accuracy described above.

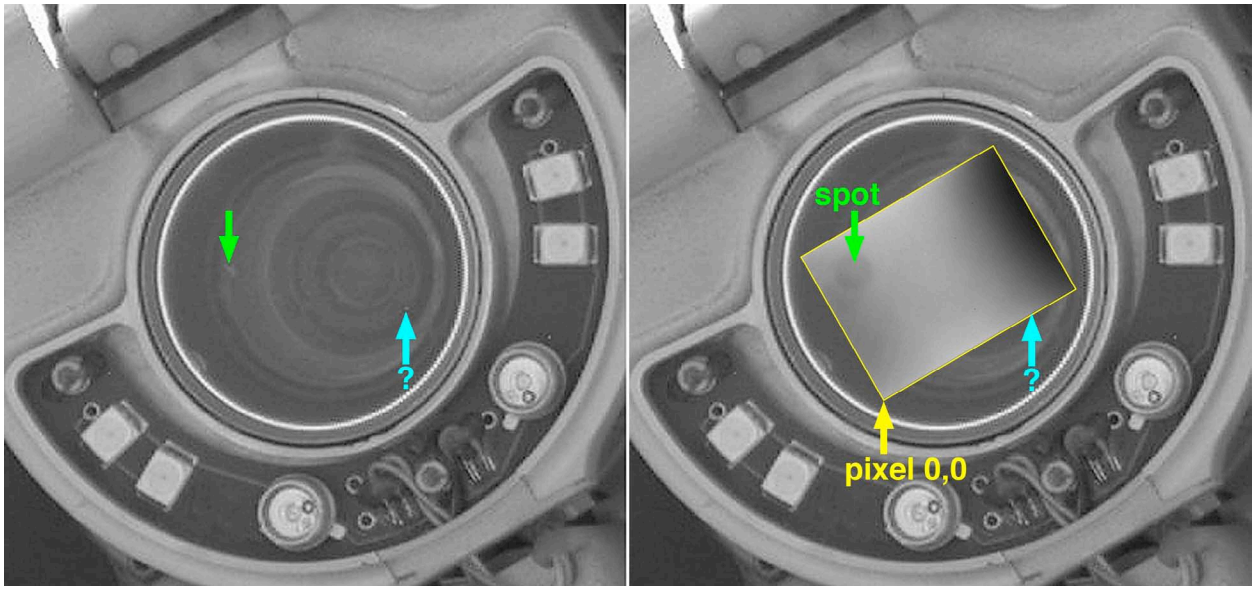

Figure 34. Green arrow at left points to a material (e.g., grain or dust grain aggregate) on the outside surface of the MAHLI front lens element, as seen by the Mastcam-100 camera on Sol 617 (2 May 2014). Green arrow at right points to the dark spot seen in all MAHLI sky flat field products throughout the Sol 86–828 period; the location of the dark spot (right) matches the location of the feature on the lens (left). The blue arrow points to a bright spot seen in the image on the left for which there is no corresponding feature in the flat field products; its nature is unknown (one speculation is that it could be a grain that was on the lens for a short period of time, between sky flat acquisitions). The Mastcam-100 image is a sub-frame of 0617MR0026380030401081E01; received as a color JPEG of compression quality 85, it was rendered into grayscale for easier viewing, here, of the spot(s) on the lens. The flat field product, at the right, is enhanced from an average of green channel sky flat products acquired Sols 322–828 at m_{open} 13014.

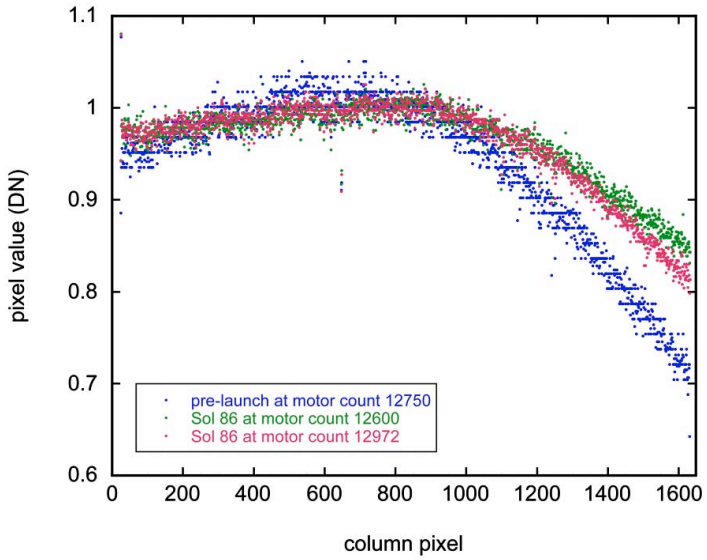

Figure 35. Comparison of pre-flight flat field (blue) and averages of Sol 86 sky flat field products acquired at nearby focus positions m_{open} 12600 (green) and 12972 (red). These are plots of green band flat field product normalized pixel values along row 599. Similar differences are observed in interpolated red and blue data (not shown). The data are in **Supplement S24**.

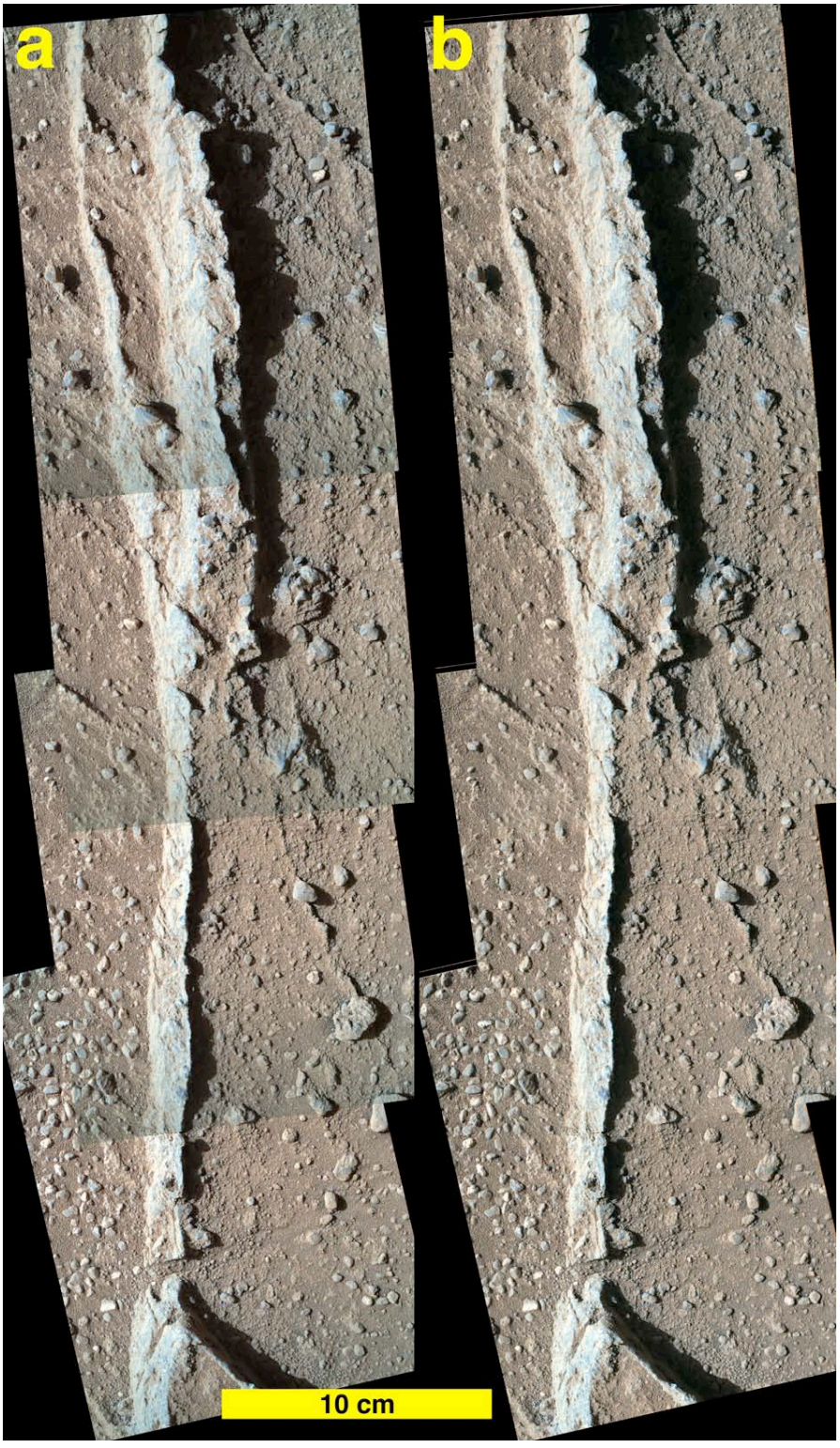

Figure 36. Comparison of MAHLI image mosaic made using **(a)** pre-flight flat field product with **(b)** an averaged (Sols 322, 516, 653, and 828) sky flat field product (at m_{open} 13014). Illuminated from the left, the four images of an erosion-resistant vein-filling material were acquired on Sol 400 (21 September 2013); they are images 0400MH0001900010104767C00, 0400MH0001900010104769C00, 0400MH0001900010104771C00, and 0400MH0001900010104773C00.

8.4 Color adjustment and white balance

White balance or color adjustments are generally a matter of individual preference or objective. Targets can look quite different, independent of calibration or other image processing, whether the scene is entirely in shadow, partially in shadow, or in full sun. In MAHLI images from Mars, fully shadowed targets always appear to be more brownish-orange than they are when viewed in sunlight; this is true even for dark gray rocks like the example in **Figure 37**.

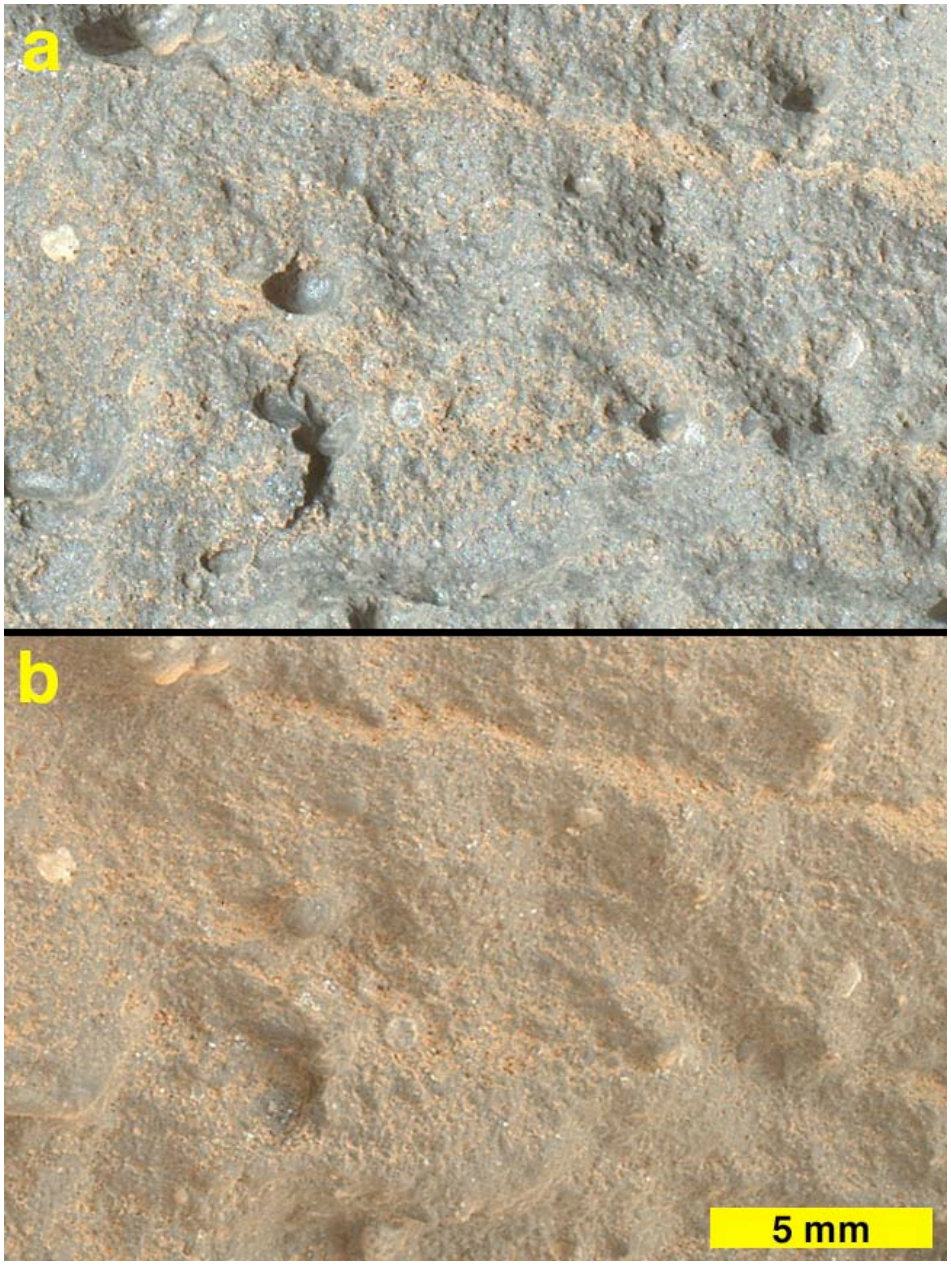

Figure 37. Gray Martian sandstone as viewed in **(a)** full sunlight (from the right) and **(b)** full shadow. In shadow, the rock appears to have a brownish-orange cast; this is typical for geologic material imaged by MAHLI in full shadow on Mars. The sunlit image is a portion of focus merge product 0586MH0003680000202977R00, acquired on Sol 585 (30 March 2014); the shadowed image is part of focus merge product 0583MH0003610000202079R00, acquired on Sol 583 (28 March 2014).

The main reason one might perform a color or white balance adjustment to an image is to accommodate illumination source "temperatures" (*i.e.*, the light source hue as compared with the temperature of a blackbody radiator matching that hue). Consumer digital cameras, for example, commonly have built-in capabilities that allow the user to adjust for differences in illumination conditions, such as a bright, sunny day, an overcast day, or indoor illumination by different types of artificial lamps. The solar illumination reaching the Martian surface, through its atmosphere and with a given opacity at a given moment in time, would differ from the terrestrial experience. One motivator for performing a color adjustment on a MAHLI image, then, is to ensure that the geologic features observed appear as they would to a human eye working with the materials if they were in a laboratory or field setting on Earth.

Figure 9 shows portions of two MAHLI images, neither of which have been calibrated. Their colors are unaltered following Bayer pattern interpolation (in one case performed onboard the instrument, in the other performed outside the instrument using the same method). One image shows a view from a cleanroom through two windows to an outside scene on Earth. The other shows a landscape and a portion of the sky as viewed from Aeolis Palus, the valley between Aeolis Mons (Mt. Sharp) and the north wall of Gale crater on Mars. The blue sky and green vegetation in the image acquired on Earth demonstrate that MAHLI produces a relatively faithful representation of color in a scene without white balance.

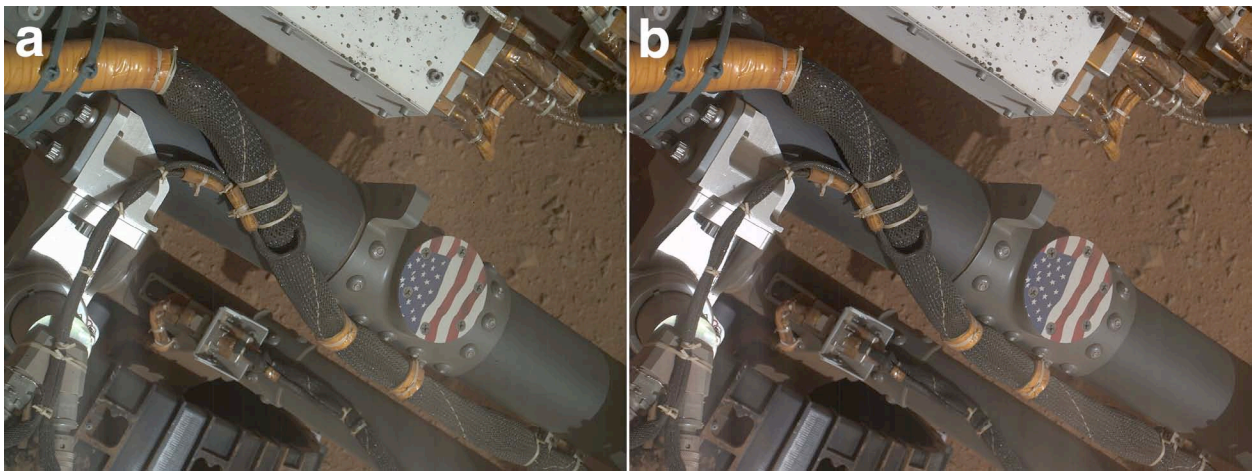

Figure 38. Color correction example. **(a)** Unprocessed image received from Mars as a JPEG 422 Bayer interpolated product; NASA PDS archive EDR product 0044MH0000060010100081E01_XXXX. **(b)** Same image with color correction as applied to NASA PDS archive RDR products (this is 0044MH0000060010100081E01_DRCX). The color-corrected view removes some of the blue tint observed on white rover surface (top center), and in the white stripes on the US flag emblem, but introduces a somewhat reddish cast. These are both from MAHLI image 0044MH0000060010100081E01 and show the middle left rover wheel (lower left), a portion of the rover body (top center), and the Martian surface (center right) in sunlight on Sol 44 (20 September 2012). Dark spots on the rover (top center) are sand grains and pebbles deposited during the terminal descent phase of the rover's landing on Mars.

MAHLI data archived with the NASA PDS include a product for which we have applied a color correction (Malin *et al.*, 2013; Caplinger, 2013). **Figure 38** shows an example of the results (we recommend that the reader examine the actual archive products, not the figure, to be certain of the colors represented). The color-corrected PDS archived MAHLI products make use of a simple, empirical analysis—independent of bandpass data—of an image acquired by the full fidelity life test/testbed MAHLI (currently onboard the testbed rover at JPL-Caltech; Edgett *et al.* (2012)). The image (see **Supplement S25**) shows a medium-fidelity prototype of the MAHLI calibration target aboard Curiosity. We took the target and testbed-MAHLI outside so that the target was illuminated by sunlight. From the resulting image, we derived color correction factors

(1.16 for red, 1.00 for green, and 1.05 for blue) based on examination of the 40% gray swatch on the target (see annotated **Supplement S25** product). The 40% gray swatch was cut from the same sheet of room temperature volcanized (RTV) silicone as the corresponding swatch on the flight MAHLI Calibration Target.

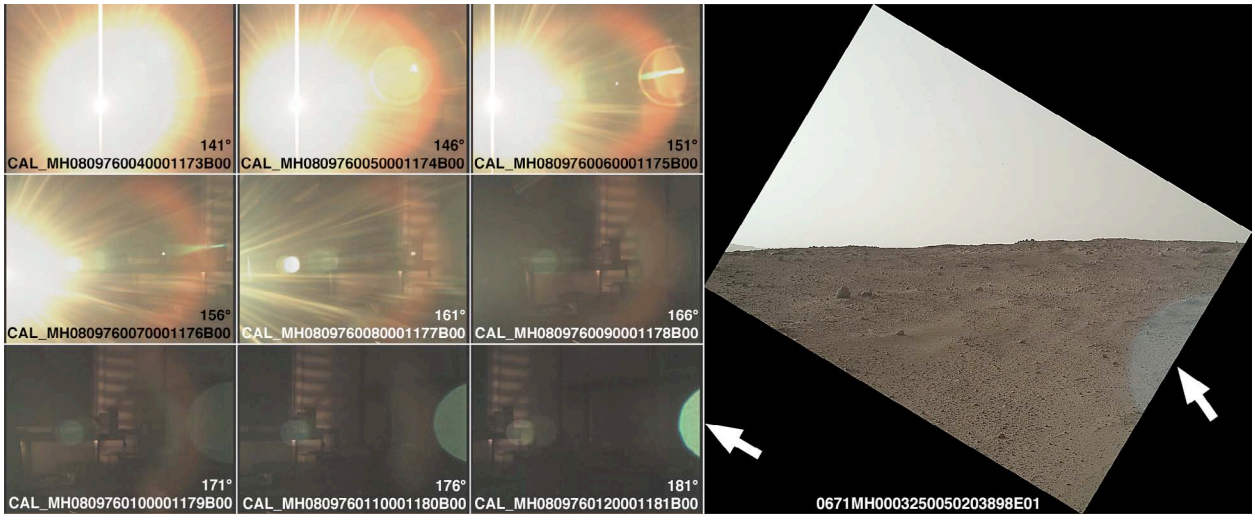

Figure 39. MAHLI images from the pre-launch stray light test, with illuminator azimuth and image ID indicated, left, and an example of lens flare observed in a MAHLI image of the Martian landscape acquired on Sol 671 (26 June 2014), right. Arrows indicate similar lens flare in an image acquired on Earth (left) and Mars (right).

8.5 Scattered and stray light

Given the MAHLI lens design and our plans to mainly use it for close-up imaging of geologic material, we had no concern regarding stray light from the sun or internally scattered sources. Indeed, we have observed no such concerns with respect to the quality and utility of geologic images that we have actually acquired on Mars. A few images of the landscape or wheels exhibit lens flare resulting from solar illumination (*e.g.*, right arrow in **Figure 39**), but the effects have not inhibited the science nor engineering value of the data. Nevertheless, we acquired stray light observations during pre-launch testing. Images CAL_MH0809760040001173B00 – CAL_MH0809760120001181B00 show a bright fiber optic illuminator that we used to simulate the sun. We obtained images of the illuminator positioned from near the optic axis to perpendicular to the optic axis in 5° increments (**Figure 39**). The illuminator was also placed at a HEPA filter on the MAHLI lens body (image CAL_MH0809760150001184B00), for which no stray light or scattering effect was observed.

9 Onboard illumination source characterization

When we proposed the MAHLI investigation to NASA in 2004, the MSL mission design included the possibility of landing at a latitude as high as ± 60° (Golombek *et al*., 2012). For a one-Mars-year primary mission, this could mean that the rover would spend substantial time in autumn and winter darkness. Thus we proposed to include white light LEDs to permit observation of

geologic materials and seasonal frost at night (Edgett *et al*., 2005). We also included UV LEDs on a best efforts basis to seek fluorescent minerals (Edgett *et al*., 2012).

9.1 White light LEDs

The MAHLI camera head has two groups of two white light Avago Technologies HSMW-100 LEDs (Edgett *et al*., 2012). Each pair (**Figure 28**), called Group 1 and Group 2, can operate independently or together. Avago Technologies describes these LEDs as having a color temperature of 6800 K; they emit light with a cool white or somewhat bluish cast (**Figure 40**) with a spectrum between 400 and 750 nm. Edgett *et al.* (2012) provided a plot of irradiance as a function of wavelength for the flight MAHLI white light LEDs. The full suite of irradiance measurements for Group 1, Group 2, and both groups operating together, with the dust cover open and closed, are provided in **Supplement S26**.

9.2 Longwave UV LEDs

The emission of MAHLI's Nichia NSHU550B LEDs UV LEDs is centered at 365 nm. Edgett *et al.* (2012) provided a plot of the flight MAHLI UV LED irradiance spectrum (the data are provided in **Supplement S26**). The LEDs induce fluorescence in responsive materials, including the fluorescent swatch on the MAHLI calibration target (Figure 14 of Edgett *et al*., 2012) and some minerals (*e.g*., Figure 31 of Edgett *et al*., 2012). The LEDs also emit sufficient visible-wavelength radiation that the images have a violet cast (**Figure 40**).

9.3 LED illumination relative to the detector

Figure 28 shows the location of the LEDs on the MAHLI camera head and how they map to the CCD, relative to the upper left pixel at column 0, row 0. **Figure 41** shows the reflections of the white light LEDs off of planar targets at different working distances. The purpose of this figure is to identify MAHLI images that one can use to estimate the position and per-pixel incidence angles of the LED illumination for images acquired on Mars. For example, we used this figure to plan how to position the camera head such that a single group of white LEDs can be pointed straight down a drill hole (*e.g*., image 0628MH0004120010203605C00).

9.4 Operational characterization

9.4.1 LED operational check-outs

As shown by Edgett *et al.* (2012), interplanetary cruise instrument check-outs included imaging with the MAHLI white LEDs illuminated to confirm their functionality following launch. After landing, robotic arm commissioning activities on Sol 32 (08 September 2012) provided the first opportunity to confirm LED operation on Mars. Illumination of the white LEDs is seen in Sol 32 Mastcam images 0032MR0000690020100777E01 and 0032ML0000690000100862E01. Comparison between Sol 32 Mastcam-100 image 0032MR0000760020100776E01 (LEDs off) and 0032MR0000690020100777E01 (LEDs on) also shows (in daylight) the violet emission from the UV LEDs, indicating that they, too, were functional after arrival on Mars. The ultimate confirmation of MAHLI LED operation on Mars came on Sol 165 (22–23 January 2013), when

we operated them at night for the first time. This first night campaign included imaging of the MAHLI calibration target with white light LEDs (*e.g.*, image 0165MH0001890010101967C00) and UV LEDs (image 0165MH0001890020101968C00) illuminated.

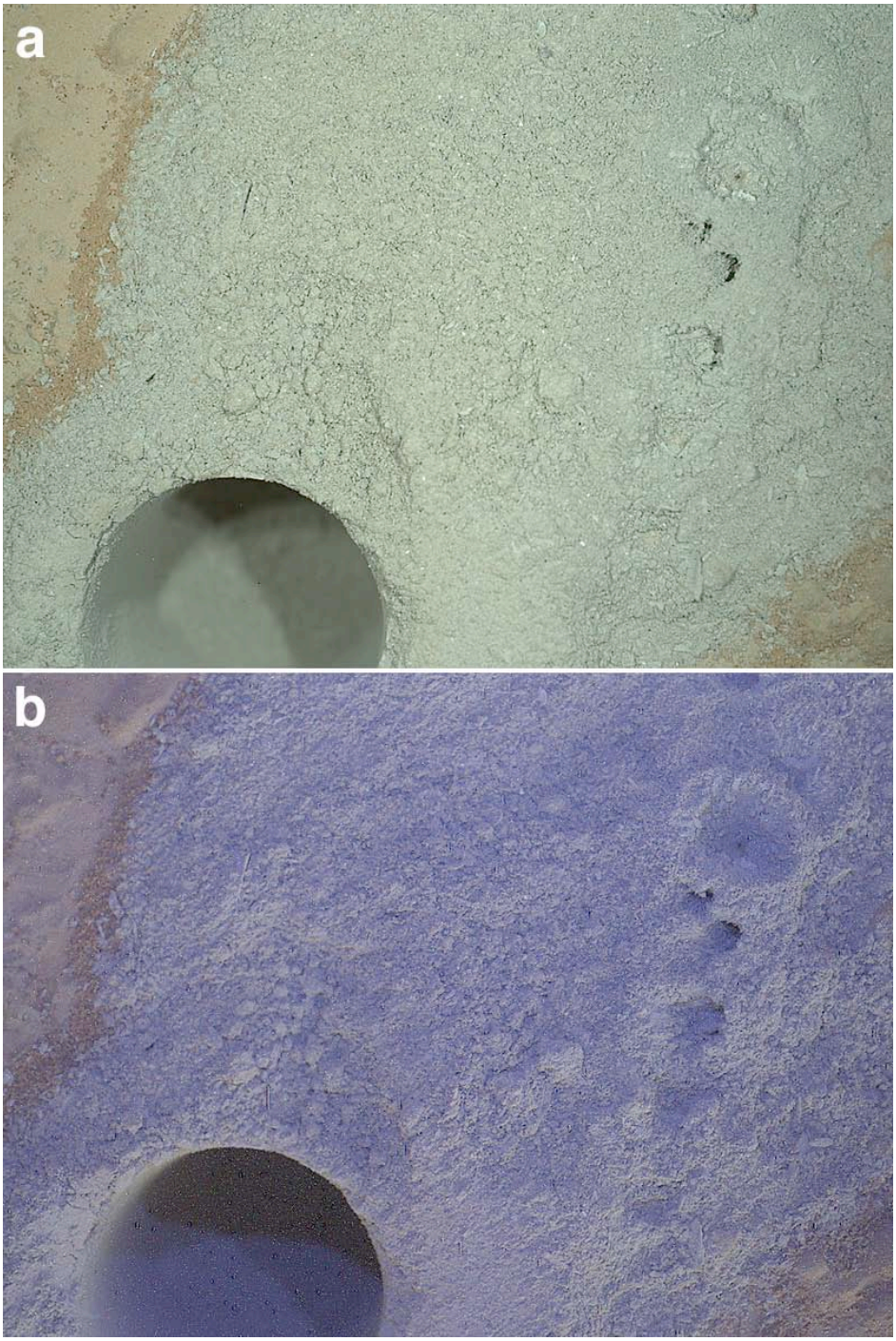

Figure 40. Examples of MAHLI images acquired at night with LEDs on. **(a)** Image 0292MH0002830030103529C00, acquired with both groups of white light LEDs on. **(b)** Image 0292MH0002830050103531C00 via 2-minute exposure with MAHLI's UV LEDs on. Acquired at night on Sol 292 (02 June 2013), the images show a portion of the 1.6 cm diameter Cumberland sample extraction drill hole and its cuttings. The rover's ChemCam LIBS formed the aligned pits on the right side of the figure.

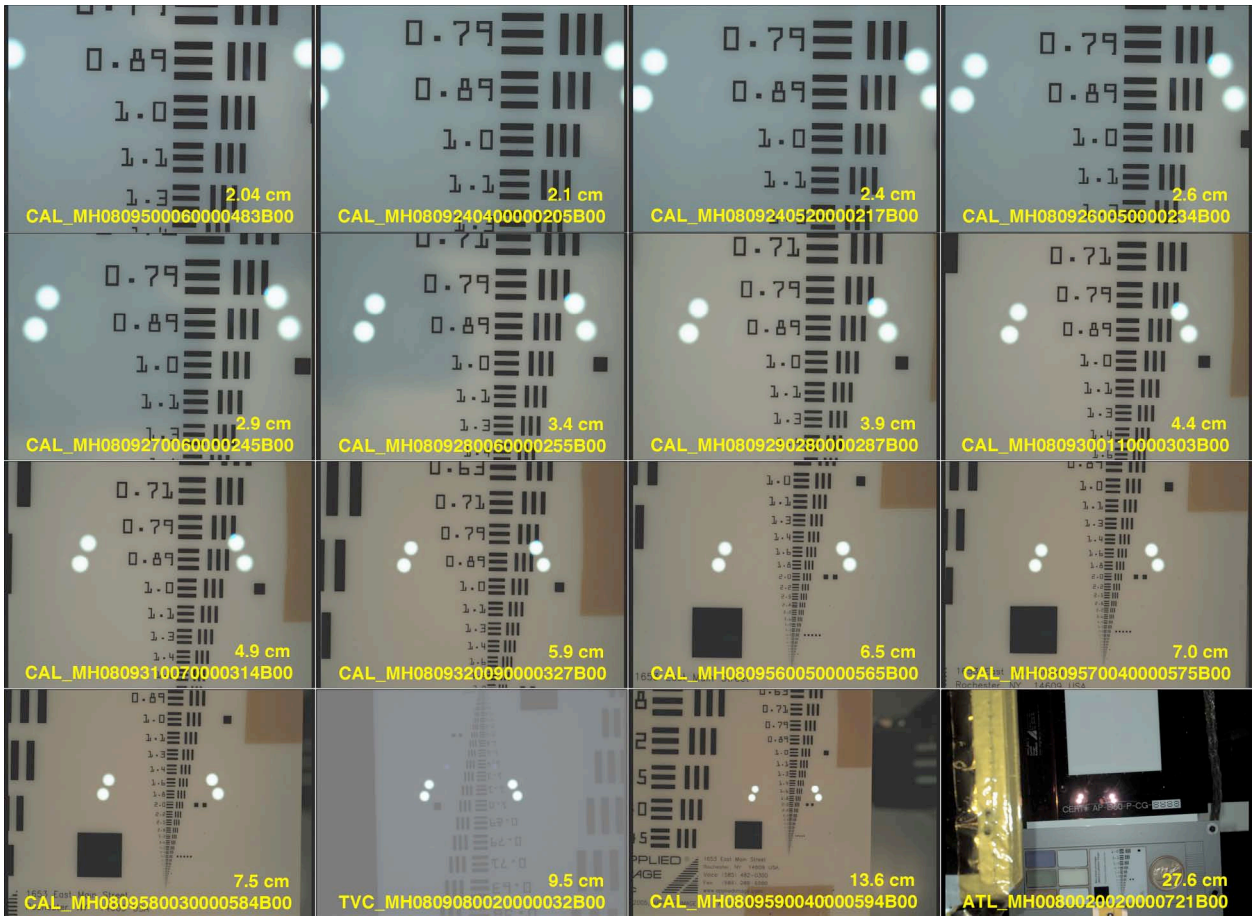

Figure 41. MAHLI white light LED zero-phase angle positions as a function of working distance. Shown are reflections of the white light LEDs off of planar targets imaged before launch. The working distance and image ID are indicated; the CCD column 0, row 0 pixel is at the upper left in each case.

9.4.2 Daytime characterization

Our instrument commissioning activities on Sol 34 (10 September 2012) included imaging of the white and UV LED reflections off of the opal glass bar target on the MAHLI calibration target. The target was in full sunlight and the camera was at a working distance of 5 cm. The white LED reflections were visible (image 0034MH0000440020100032E01) but the UV LED violet reflections were not (image 0034MH0000440030100033E01).

One notion we considered early in the MAHLI instrument development period was that the white light LEDs might be useful for illuminating targets in full shadow (Edgett *et al.*, 2005). We tested this idea during the Sol 46 and 47 imaging of the first contact science target, the boulder named Jake Matijevic (**Figure 18**). The value of operating the white light LEDs was minimal; the main effect was to reduce exposure duration by 0–10 milliseconds. On Sol 47, most of the exposure durations did not change, regardless of whether the LEDs were on or off. We have rarely pursued daytime operation of the LEDs since then.

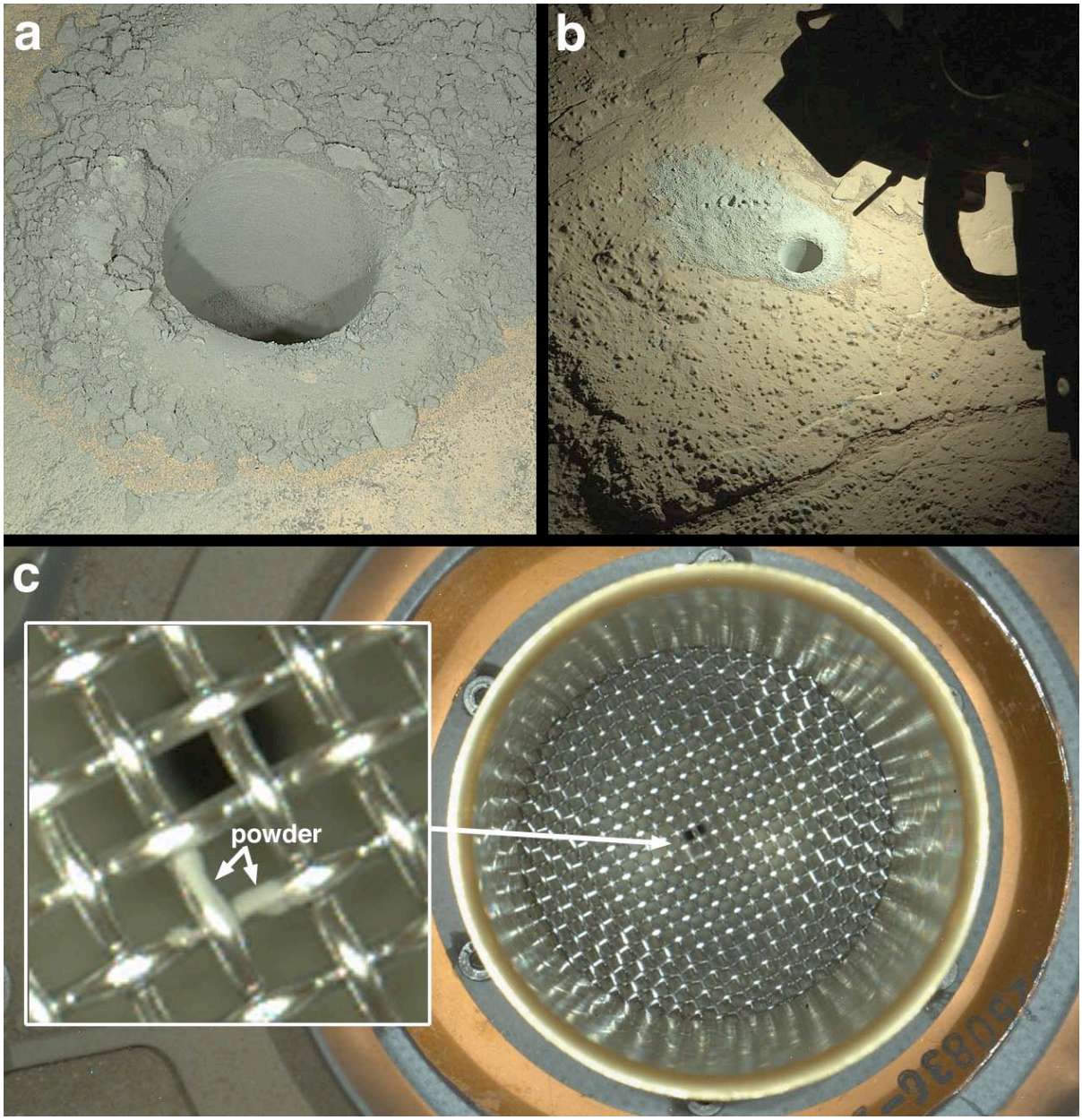

Figure 42. Examples of MAHLI nighttime white light LED operations. **(a)** Examination of sample extraction hole walls with minimized shadowing; this is the Windjana drill hole, 1.6 cm wide, imaged on Sol 628; sub-frame of focus merge product 0629MH0004130000203717R00). **(b)** Use of MAHLI camera head as a flashlight for night imaging by other cameras; this is Mastcam-100 image 0292MR0012330000203546E01, showing the Cumberland drill hole, 1.6 cm wide, on Sol 292. **(c)** MAHLI inspection of fines clinging to 1 mm mesh inside the 3.5 cm diameter ChemMin sample inlet, as seen on Sol 411. These are sub-frames of MAHLI images 0411MH0002280000200031C00 and 0411MH0003120020200029C00.

9.4.3 Night characterization and utility

Before landing, it was unclear to us whether night operation of the robotic arm would be permitted. Thus it was unclear whether night imaging would involve positioning MAHLI at night or during the preceding daylight period. If the latter, then MAHLI would only be able to image

one target from one position; further, it was unclear whether the dust cover would have to be left open all night if the target was too close to the cover to permit its motion.

After landing, and given the thermal environment in Gale, it became clearer that the robotic arm could be used to move the camera head at night, particularly as long as it retained sufficient heat (warmed by sunlight during the day) so as to minimize use of power to heat its actuators. Thus, for some time after sunset (the duration dependent on season), the robotic arm and MAHLI can be operated the same as if during the day.

The most important lesson we learned from the first night operations, on Sol 165, was to operate only one group of white light LEDs when performing an autofocus. With one group operational, the micro-relief on the target exhibits some shadowing and this enhances autofocus capability relative to the case in which both groups of LEDs are operated. This approach was implemented for nominal night operations thereafter.

In some cases, we found that night imaging was the most ideal option for specific science or engineering goals (Minitti *et al*., 2014). In other cases, we performed night imaging because rover hardware would cast shadows that prevent the target from being viewed in sunlight during the day (McBride *et al*., 2015). We also developed a preference for imaging sample extraction (drill) hole walls at night to minimize shadowing (**Figure 42a**); for example, compare images of the Cumberland drill hole acquired in the daytime on Sol 279 (19 May 2013; product 0279MH0002710000103164R00) and nighttime on Sol 292 (02 June 2013; product 0293MH0002850000103636R00).

Also because of shadowing, we found that night illumination of the interior of the CheMin sample inlet provided a sharper inspection for fine particles clinging to the mesh above the inlet funnel (**Figure 42c**). Finally, we also found the LEDs to have utility as a flashlight to illuminate targets that can be viewed by other cameras aboard Curiosity, when desired (**Figure 42b**).

Figure 43 shows the white LED auto-exposure durations for full-frame images, as a function of camera standoff distance, measured by MAHLI imaging for geologic materials encountered by the Curiosity rover during the first 869 sols of operations; these values are typical and can be used to make estimates for manual exposures of similar targets.

10 Archival data product calibration

A *calibration pipeline* is a series of steps—that can optionally be computer automated—which lead to the creation of calibrated data products. Here, we refer specifically to products we create from MAHLI Experiment Data Record (EDR) images archived with the NASA PDS to produce the calibrated PDS archival products called Reduced Data Records (RDR). In this section we describe the present implementation of the MAHLI calibration pipeline as applied to RDR products. Provided that the mission lasts several more years and resources are available to do so, we anticipate that we will improve this implementation. Data users who require a more sophisticated calibration are encouraged to use this report and the PDS archived data and documentation to produce their desired product.

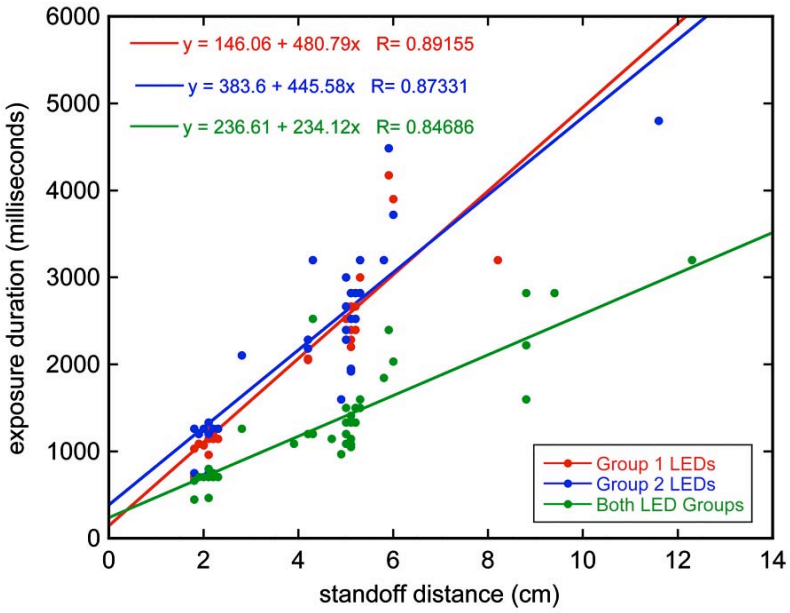

Figure 43. Auto-exposure durations for white light LED illuminated geologic targets on Mars at night, as a function of standoff distance, for full-frame image targets observed between Sols 165 (23 January 2013) and 869 (16 January 2015). The relations between distance and exposure expressed here are independent of target color and albedo and represent typical cases encountered during the sol range. The plotted data are listed in **Supplement S27**.

10.1 NASA Planetary Data System (PDS) archival products

The NASA PDS archives include documentation that describes the MAHLI image ID and file naming scheme and the nature of the EDR and RDR products (Malin *et al*., 2013). The RDR products, created via the calibration pipeline described below, are of the following nature:

1 **[Image ID]_DRXX** – 16-bit depth (per band) relative radiometric calibrated color images,

2 **[Image ID]_DRLX** – 16-bit depth (per band) relative radiometric calibrated and geometric calibrated color images,

3 **[Image ID]_DRCX** – 8-bit relative radiometric calibrated images for which the color correction described in Section 8.4 has been applied, and

4 **[Image ID]_DRCL** – 8-bit relative radiometric and geometric calibrated images for which the color correction described in Section 8.4 has been applied.

For completeness, the MAHLI EDR products, the raw data product, have the following file name scheme: **[Image ID]_XXXX**. **Table 7** describes the variety of image types (raw, lossless, JPEG, focus merge, thumbnail, *etc.*); the EDR files are always 8-bit images except for the 16-bit products (type A) returned from MAHLI for calibration purposes.

10.2 RDR calibration pipeline

The MAHLI archival calibration pipeline is illustrated in Figure 5.1-1 of Malin *et al.* (2013). The process begins with the EDR image; we decompress and decompand it from 8 to 12 bits (forming a 16-bit image). Then we remove dark current, followed optionally by shutter smear mitigation, then flat field correction. If necessary, additional bad pixels can be identified and removed. This results in a relative radiometric calibration product (**_DRXX**) with attendant

information, in the image label (.LBL file), regarding an approach to expressing the 16-bit DN values in *I/F* (irradiance, *I*, as a function of solar flux, *F*) form. Thereafter, we apply color correction (**_DRCX**), geometric correction (**_DRLX**), and both (**_DRCL**), to produce the full suite of RDR products. MAHLI focus merge best focus image products receive only a dark current correction to produce the **_DRXX** product and a color correction to create the **_DRCX** product; they are not flat field nor geometrically corrected. Focus merge range map products receive no calibration (only EDR **_XXXX** products are available).

10.3 Relative radiometric calibration

10.3.1 Data from the instrument

Onboard the instrument, an analog-to-digital converter digitizes the MAHLI CCD output and the resulting 12-bit image is sent from the camera head to the DEA. These 12-bit pixels have a nominal scale factor of 16.3 electrons per DN. Read noise is ~1 DN and the full well capacity is near 30,000 electrons. Most of the data returned from MAHLI are companded onboard from 12-bit to 8-bit form using a lookup table with 4096 entries. A residual DC offset is subtracted prior to encoding; the value of the offset is commandable and is documented in the NASA PDS archive label for each data product. The default onboard companding table quantizes larger DNs more coarsely because larger values have a higher shot noise component. The full suite of compand/decompand tables is presented with the archived PDS products in Appendix B of Malin *et al.* (2013).

10.3.2 Image decompression and decompanding

For traceability to the original data, the archived RDR products begin with a corresponding parent EDR file. If the EDR image was compressed, then it is decompressed into spatial domain format. The $Y{:}C_R{:}C_B$ coefficient 8 by 8 frequency domain JPEG minimum coded units (MCUs) are transformed back into 8 by 8 spatial MCUs and reordered into image arrays for each of the three output color bands (RGB). The output, at this stage, is an 8-bit grayscale image for some of the products (those for which the parent is not a color image) or a 24-bit (3 band sequential channels) color product.

Decompanding returns the 8-bit images to their original 12-bit form, but there are potential losses owing to the nature of the encoding scheme. The most commonly used companding table is a square root encoding table, which maps several 12-bit values to the same 8-bit value. For example, original 12-bit values 31 and 32 are companded to 25, 338 through 344 are companded to 100, 773-785 are companded to 155, *etc.* Expanding these back to 12-bit products potentially leads to DN contouring, although noise tends to mitigate this effect (indeed, square root encoding is commonly used because it preserves noise). Functionally, decompanding applies the following:

$$DN_{16}(i, j) = LUT_n[DN_8(i, j)], \quad (13)$$

in which *i* and *j* are the image array pixel columns and rows, DN_8 are the 8-bit array values, DN_{16} are the 16-bit decompanded values, and *n* is the decompanding look-up table (*LUT*) in Appendix B of Malin *et al.* (2013).

10.3.3 Dark current compensation

We implemented three options for image dark current compensation (Malin *et al*., 2013). Our preferred option is to use dark current information captured in columns 9–16 of a given MAHLI image. When this is not possible (*e.g*., if columns 9–16 were not acquired), the next option is to relate the temperature of the focal plane with dark current values determined in pre-launch testing. When neither of these first two options is available, our third approach is to apply information from a different image acquired close to the same time.

Our preferred approach uses the dark pixels in columns 9–16 of the CCD (in which the upper left corner pixel is column 0, row 0). As described in **Section 8.1.3**, these pixels provide dark current information and we can relate their DN values to temperature and exposure duration. The 16-bit DN value of dark current (DN_{dark}) as a function of temperature (T) is computed from the following equation, which is a fit to the curve for the 1000 millisecond exposure case in **Figure 23b**:

$$DN_{dark} = a + bT + cT^2 + dT^3 + eT^4 + fT^5 + gT^6, \quad (14)$$

in which $a = 120.003$, $b = 3.32437\times10^{-2}$, $c = 1.42158\times10^{-2}$, $d = 2.32654\times10^{-4}$, $e = -5.62326\times10^{-7}$, $f = 6.48101\times10^{-8}$, and $g = 1.65756363432\times10^{-9}$. A key limitation of the approach, as currently implemented, is that it is based only on the 1000 millisecond exposure case and does not yield dark current as a function of exposure time.

We only use dark pixel data from columns 9–16 because some images are returned as JPEG-compressed products and the MCU size for JPEG images is 8 by 8 pixels and columns 9–16 are the only eight columns that are entirely composed of masked, dark pixels. Thumbnail images, which are ~1/8th the dimensions of the parent image, have columns 9–16 averaged to form column 2. For consistency, columns 9–16 are also utilized for uncompressed and lossless compressed image processing. Functionally, removal of dark current (DN_{dkrm}) from these images is as follows:

$$DN_{dkrm}(i, j) = DN_{16}(i, j) - c_m \quad (15)$$

in which c_m is the estimate of dark current using the mean value from the dark pixel columns.

When dark columns 9–16 have not been acquired for a given image, our first alternative is to use the downlinked temperature of the focal plane. Charge accumulation as a function of temperature and exposure duration can be expressed as *DN* per second. The DC offset is removed from DN values during image acquisition; the DC offset and exposure duration are provided in the headers for each archived MAHLI image:

$$DN_{dkrm}(i, j) = DN_{16}(i, j) - bias \quad (16)$$

in which bias is the exposure duration times DN/second minus the DC offset.

Finally, in cases for which dark columns 9–16 are not present and a focal plane temperature is not available, we supply a user-determined value. This value is perhaps best determined, using **Equation 16**, using the bias from an image acquired close in time from the same instrument.

10.3.4 Shutter smear mitigation

Cameras without physical shutters implement shuttering by shifting the accumulated photoelectrically generated charge to locations that are less but still somewhat light sensitive. As the charge is read out, a small amount of light falls on the detector and is added in a sequentially to the image. This is called shutter smear. Under appropriate conditions (a static scene without much pixel to pixel structure), shutter smear can be mitigated by taking a part of the scene (usually one line at a time) and computing its fractional contribution to the next line, repeatedly through the entire image.

Our shutter smear mitigation approach is optional for MAHLI images. Indeed, shutter smear is negligible for images with exposures > 100 milliseconds. It is most pronounced when the readout time is large relative to the exposure time. Shutter smear mitigation was developed to accommodate the MSL MARDI, which is electronically equivalent to MAHLI. The short exposure time for MARDI's descent images (0.9 ms) were considered likely to exhibit shutter smear. The nature of the imaged scene, itself, can be used to determine the accumulated effect of shutter smear, and to subtract that accumulation from the final image. A complication in mitigating shutter smear in cameras like MARDI and MAHLI is that the sensitivity of each pixel in each line varies because the Bayer micro-filtered array imposes an additional pattern on the image. Mitigation is thus only applied to images that were color interpolated onboard the instrument and does not include focus merge products.

The shutter smear approach considers that photon-induced electrons are shifted off the CCD sensor, vertically, toward row 0. As electrons are shifted past pixels accumulating scene-dependent charge, they accumulate a portion of that charge. This charge is based on the clock readout rate, and shutter smear is a fraction of the readout rate and the exposure time. Because the smear is scene-dependent, we assume that the scene does not vary during integration or readout time (as this assumption can not always be correct, shutter smear is only mitigated, not removed). A fraction of each line is added to an accumulator, which is subtracted from each line in the direction opposite the readout direction. The smear factor (s_f) is dependent on exposure duration (e_{time}) and line readout rate (t_{line_read}):

$$S_{(i,j)} = (\mathrm{DN}_{(i)}\,(s_f) t_{line\_read}\,)\; e_{time}^{-1}$$

$$DN_{\mathrm{desmeared}(i,j)} = DN_{(i,j)} - S_{(i,j\text{-}1)} \qquad (17)$$

in which $S_{(i,j)}$ is the accumulated smear at image column i, row j. The accumulator is seeded with zero values for row j = 0. Note that a value for s_f has not yet been established for MAHLI.

10.3.5 Flat field application

The pixel-to-pixel, non-uniform variation of the camera's response is corrected through application of a flat field product. Our current implementation uses the pre-launch flat field product (PDS archived file FLAT_MH_0.IMG). As of this writing, we have not yet approved application of the Mars sky flat field products to archival product creation.

The flat field product is a matrix of fractional values with the same dimensions as a full-frame MAHLI image. If the image received from the instrument is an image sub-frame, then the corresponding portion of the flat field product is referenced accordingly. For pixel i, j in the acquired image (sub-frames must be offset):

$$DN_{flat\_corrected(i,j)} = DN_{(i,j)} / flat_{(i,j)} \quad (18)$$

in which *flat* is the flat field product applied specific to that image. Flat fields can be applied to images received uncompressed and losslessly compressed with high resolution fields encoded specific to each Bayer filter array and pixel position. JPEG images have flat fields for either luminance, or red, green, and blue channels; these are derived via a Bayer pattern color interpolation of the reference file (*e.g.*, FLAT_MH_0.IMG). Thumbnail images make use of a subsampled flat field product that is 1/8th of the original image dimensions. As in the case of JPEG-compressed full-size images, thumbnail flat field products are derived from a reference file (*e.g.*, FLAT_MH_0.IMG) for luminance or red, green, and blue channels.

10.3.6 Bad pixel mitigation

As described in **Sections 8.1.4 and 8.1.5**, MAHLI images have three sources for localized pixel response variations: non-uniformities in the sensitivity of the individual pixels, particulates on the detector, and radiation damage. The calibration pipeline for RDR products currently archived with the PDS does not implement bad pixel mitigation but we might do so in the future. Application of a flat field removes most of the effects of particulates on the detector.

10.3.7 *I/F* radiometry

The output of the above steps, decompanding, dark current correction, flat field application, and optional shutter smear and bad pixel mitigation, result in a RDR product (**_DRXX**) for which the label file (.LBL) also includes a RADIANCE_SCALING_FACTOR. This consists of three values, one for each of the Bayer RGB filters. They provide the data user an option to convert the **_DRXX** image 16-bit DNs to *I/F* values, the ratio of reflected energy to incoming energy (irradiance/solar flux), for each RGB pixel. *I/F*, in this case, is the ratio between the observed signal level and that which would be produced by imaging a perfectly white surface illuminated by sunlight at 0° incidence at the perihelion distance of Mars with no atmospheric attenuation. Multiplying the RADIANCE_SCALING_FACTOR by the 16-bit DN of the **_DRXX** product provide the *I/F* values.

The RADIANCE_SCALING_FACTOR thus provides the user with an option for computing *I/F*; the uncertainty is of the order of 10% for cases in which the target is illuminated by the sun. The RADIANCE_SCALING_FACTOR is not always applicable to a given image; for example, some images are acquired with the target in shadow or they are obtained at night with LED illumination. The RADIANCE_SCALING_FACTOR for red, green, and blue (three values, reported in that order, in the **_DRXX** image .LBL file) is determined relative to a reference case computed for a white target with Mars at the perihelion solar distance of 2.07×10^8 km, an exposure duration of 10 milliseconds, and a camera focal ratio of f/8. In this reference case, the number of electrons reaching each red, green, and blue (RGB) pixel is 152298, 164451, and 176259, respectively. Dividing by the scale factor of 16.3 electrons per 16-bit DN, the reference case 16-bit signal levels per RGB band, r_{band}, are 9343, 10088, and 10813, respectively.

To determine the expected signal (s_{band}, in 16-bit DN per RGB band) for a given MAHLI image of exposure duration e_{time} (in milliseconds), solar distance of d_{sun} (in kilometers), and focal ratio f_n, relative to the reference case described above, we use:

$$s_{band} = r_{band} (e_{time}/10.0) ((2.07 \times 10^8)^2/d_{sun}^2) (f_n^2/8.0^2) \quad (19)$$

In the current implementation that produces the RADIANCE_SCALING_FACTOR reported in the **_DRXX** image labels (.LBL files), we assume a constant focal ratio of f/9.0. The RADIANCE_SCALING_FACTOR reported is the ratio of s_{band} to r_{band} for each RGB band.

10.4 Color correction

Following creation of the relative radiometric calibrated product, a color correction or white balance can optionally be applied. For the MAHLI RDRs, we apply the color correction factors described in **Section 8.4** for the red, green, and blue channels: 1.16, 1.00, 1.05.

10.5 Geometric correction (linearization)

10.5.1 CAHVOR model reported in archived products

For a given MAHLI image, the JPL-produced CAHVOR camera model (**Section 7.2**) parameters are determined by JPL-Caltech and archived with each EDR (**_XXXX**) image as well as each RDR product that has not been geometrically corrected (**_DRXX**, **_DRCX**). The CAHVOR vectors are reported in the image label files (.LBL). As currently implemented, these reports assume a fixed focus position of $m_{open} = 12594$, corresponding to a working distance > 250 cm—*i.e.*, approaching infinity.

10.5.2 CAHV model and creation of archived linearized products

Our MSSS-produced camera model (**Section 7.1**) is directly applied to MAHLI images to produce the linearized RDR products (**_DRLX**, **_DRCL**). In the image label (.LBL) file, these results are reported as a four vector CAHV model. A *linearized* image is one from which the effects of lens distortion have been removed and slight deviations of each pixel from square have been adjusted. The processing involves warping the image pixels to show how the scene would appear if imaged by an ideal camera that has no distortion. The resulting image can be modeled using a simple pinhole camera model or, equivalently, a CAHV model.

Radial lens distortion is modeled by adjusting the image point in the focal plane using a polynomial. Given the x, y focal plane coordinate system—without distortion, in millimeters, and for which the center of distortion is at x_0, y_0, which might be offset from the principal point at 0, 0—and a radial distance, r, in millimeters from the center of distortion to the image point (see **Equation 8**), then the radial distortion of that point is:

$$\Delta r = k_1 r^3 + k_2 r^5 + k_3 r^7 \tag{20}$$

and

$$\Delta x = x(\Delta r/r) \text{ and } \Delta y = x(\Delta r/r). \tag{21}$$

Distortion is removed by inverting the nonlinear equation using an iterative procedure such as Newton's method. The interior orientation part of the camera model models the relationship between the focal plane and the actual detector (**Equations 10 and 11**).

Geometric correction of a MAHLI image begins with determination of the size of the linearized image by projecting points along the edge (this process uses the four corners and four midpoints) onto the focal plane. The limits of the projection are used to set the sub-frame for the new image. A detector in this case is defined as having square pixels with the nominal pixel pitch and principal point as the original image. The value for each pixel in the linearized image is calculated by projecting the center of each pixel onto the focal plane, application of the radial distortion model and then transfer of the position to a fractional pixel location in the original image. Bi-cubic interpolation is then used to calculate the actual value. Some pixels in the linearized image might project outside the original image and are given a missing data value. This value is defined by the MISSING_VALUE keyword in the PDS product label (.LBL) files.

For the NASA PDS archival RDR products, the linearized camera model is stored a CAHV model in the PDS product label. The CAHV model can be losslessly constructed from the pinhole camera model. Via the CAHV model, if P is a point in the scene, then the corresponding image locations x, y (columns, rows) can be computed as follows:

$$x = ((P - C)\,V) / ((P - C)\,A) \text{ and } y = ((P - C)\,H) / ((P - C)\,A). \quad (22)$$

11 Future refinement and monitoring

11.1 New calibration and performance data acquisitions

The current NASA plan funds the MSL mission through at least September 2016. As long as the mission continues and MAHLI is operational, we will continue to acquire images of the MAHLI calibration target and flat field sky data on a regular basis to monitor for changes in instrument performance, contribute to the refinement of MAHLI calibration, and ensure these images are collected for future data users to apply to their calibration needs. Most importantly, we will add sky flat field imaging at m_{open} 12750 to mimic that of the pre-launch flat field product. As shown in **Table 4**, the repeat interval for these MAHLI calibration observations is 180 sols, but the actual intervals vary depending on other, higher priority science and engineering activities that may take place. Of course, during the sols between the sky flat and calibration target imaging, we continually observe instrument health and imaging performance by inspection of all of the downlinked images and instrument engineering data.

11.2 Potential for cross-calibration with MSL Mast Cameras

On two occasions, Sols 544 (16 February 2014) and 707 (2 August 2014), we had the robotic arm position the MAHLI camera head at a location from which it can image the Mastcam calibration target (Kinch *et al*., 2013) with similar geometry and illumination as viewed by the Mastcams. We acquired these observations in conjunction with MAHLI photometric image suites described by Johnson *et al.* (2015). MAHLI images of the Mastcam calibration target are not regularly repeated (**Table 4**) but we plan to continue to acquire them whenever the Johnson *et al.* (2015) photometric sequence is re-run. These images form a data set that can be used by to consider not only MAHLI radiometric performance on Mars but also provide potential for cross-calibration with the Mastcams.

11.3 Refinement of geometric calibration and 3D product performance

In 2015–2016 we are investigating the utility of MAHLI to provide quantitative 3D representation of objects, particularly in the context of Mars habitability assessment (Garvin *et al.*, 2015). For example, on Sol 808 (14 November 2014), we acquired a stereo pair covering the REMS ultraviolet sensor (Gómez-Elvira *et al*., 2012) located on the rover deck. The purpose for this acquisition, images 0808MH0000950010300741C00 and 0808MH0000950010300743C00, was to provide an object of known dimensions to help characterize the accuracy of quantitative 3D models produced from MAHLI data. Garvin *et al.* (2015) reported initial results. We plan to conduct additional characterization of quantitative 3D products by imaging additional natural (*e.g.*, Mars rocks) and artificial (*e.g.*, MAHLI calibration target) subjects.

11.4 Refinements to calibrated archived data products

Provided that the MSL mission and MAHLI operations activities continue and resources are available to improve calibration, then we plan to improve the archived RDR data products over time. Improvements would include refinements to the removal of dark current, application of flat field products derived from Mars sky observations, and the camera model.

12 Lessons learned

We conclude with a brief description of lessons learned that might be applicable to future instrumentation similar to MSL MAHLI. MAHLI is an outstanding science instrument and engineering tool. It has performed spectacularly on Mars to address a wide range of science and science-enabling engineering objectives. The lessons learned are as follows:

1 **Prioritization:** The prioritization of tasks for both the collection of instrument characterization and calibration data and for analysis of the data was excellent for the particular case of the MSL MAHLI. Priority was given to characterizing the specific relationship between focus position (motor count) and the scale of features observed in images; characterization of robotic arm positioning, repeatability and motion damping; and understanding of the information content and quality of onboard focus merge products.

2 **Data archiving:** The fact that we organized, validated, and archived (with NASA PDS) the pre-launch MAHLI images was of high value to the effort of assembling and communicating this report. This archive also ensures that future investigators have access to these data. It is not always the case, with publicly funded planetary science investigations, that the pre-launch data are deposited in a public archive.

3 **Pre-launch instrument characterization:** Although there is no vital impact to the utility of MAHLI images for geoscience interpretation, we wish we had acquired better pre-launch data to address flat field response and MTF. In particular, these would have been acquired at multiple focus positions, including the minimum and maximum working distances and the distances between them that we anticipated to be used most frequently during the surface mission. The choice of MTF targets (and their illumination) could be improved and the

impact on MTF of the application of different Bayer color interpolation schemes could be more deeply considered.

4 **Characterization for 3D product generation:** We did not intend that the MAHLI investigation would require quantitative relief modeling; that is, to make use of multiple images, such as stereo pairs, to provide 3D models that give measures of rock, regolith, and eolian deposit surface texture. However, interest in and use of such products in the geosciences has generally increased since we started our work in 2004. Given the interest, calibration plans for future instruments similar to MAHLI should consider acquiring sufficient data to characterize the instrument's 3D visualization capabilities over the full range of focus, from minimum to maximum working distance focus positions. Quantitative relief models derived from such images could be validated before launch using independently characterized natural materials (*e.g.*, rock surfaces).

5 **Autofocus and autofocus sub-frames in pre-launch testing:** Autofocus was not available until late in the pre-delivery testing of MAHLI. Application of autofocus via sub-frames, as is routinely performed on Mars, was not often used in pre-launch tests. Future instruments similar to MAHLI should use this capability. For example, autofocus sub-frames centered on each calibration target imaged by MAHLI on 2–7 December 2010 would have permitted these data to be used to inform knowledge of the relationship between motor count, working distance and image scale, especially at distances > 1 m.

6 **Flight calibration target design:** The flight MAHLI calibration target, described by Edgett *et al.* (2012), need not have been as large as it is. The width was essential to ensure the MAHLI contact sensor probes do not touch the target, but the length was more than necessary. In a revised target, the color, gray, and fluorescent swatches could be smaller; the bar target size is sufficient but the use of reflective opal glass and blue chrome printing should be reconsidered; the U.S. cent target is useful for estimates of scale and public demonstration of camera capabilities but it is not required; the utility of the stair-step target for 3D visualization characterization is perhaps not necessary if pre-launch characterization for stereo and 3D applications is adequate. The surfaces designed to be touched by the MAHLI contact sensor probes are recessed such that the target elements are closer to the lens than these contact surfaces; this was unnecessary (as built, the camera would be too close to the target to focus the lens when the contact probes are touching a target); a revised target would place these surfaces flush with the upper surface of the target. Finally, if the target is mounted such that it could become coated with dust during the landed payload terminal descent, then a one-time deployable dust cover should be considered; alternatively, perhaps use a dust cover that can be opened and closed regularly, to keep the target clean throughout the mission if it will be deployed in an eolian environment like the surface of Mars.

Supplementary material are in file MAHLITechRept0001_Supplement.zip

Acknowledgements

The MAHLI investigation was developed and operated under subcontracts 1269421 and 1273887 in collaboration with JPL-Caltech (Jet Propulsion Laboratory, California Institute of Technology) under NASA contracts NAS7-03001 and NMO710846. JPL-Caltech manages MSL for NASA. Part of this research was conducted at JPL. This report is the product of a very large team effort involving everyone who helped build, test, and operate the instrument; everyone who contributed to funding, managing, building, testing, and operating the spacecraft (including successful launch and landing); everyone who contributed to the process of data archiving and peer review; and the many persons involved with contracts, payroll, office support, *etc.*; thousands of individuals contributed. In particular, we thank N. Izenberg, J. Johnson, K. Klaasen, R. West, and H. H. Kieffer for their critiques of the MAHLI calibration plan performed in 2007–2008, M. Milazzo for a helpful review of a January 2015 version of this manuscript, and D. Fey for a review of the June 2015 manuscript. We heartily thank T. Lesperance for his work in development of the MAHLI onboard focus merge capability; S. Brylow, J. Schaffner, M. Clark, P. Otjens, H. Olawale, J. Tamayo, M. C. Malin and B. A. Cantor for their roles in instrument fabrication, testing, delivery, calibration analysis, and management; J. J. Simmonds for his extensive efforts as the MSL Science Payload Manager throughout the instrument development and operations periods; the Mastcam, MAHLI, MARDI Science Team, including J. F. Bell III, J. Cameron, W. E. Dietrich, L. J. Edwards, J. B. Garvin, B. Hallet, E. Heydari, L. C. Kah, M. T. Lemmon, T. S. Olson, T. J. Parker, S. K. Rowland, J. Schieber, R. Sletten, R. J. Sullivan, and P. C. Thomas; the MSL Science Team, especially J. Grotzinger, A. Vasavada, J. Crisp; M. L. Robinson, L. Jandura, B. Pavri, C. Collins, A. Thompson, and many others for their efforts in MAHLI testing at JPL-Caltech; Curiosity's robotic arm operators, including P. Bellutta, J. J. Biesiadecki, J. L. Carsten, B. K. Cooper, D. T. Fuller, M. Gildner, F. R. Hartman, M. C. Heverly, E. K. Hines, R. Kinnett, S. R. Kuhn, P. C. Leger, M. W. Maimone, S. A. Maxwell, S. H. McCloskey, M. C. McHenry, J. M. Morookian, A. B. Okon, O. Pariser, C. Roumeliotis, V. V. Tompkins, O. Toupet, N. Wiltsie, J. R. Wright, and J. Yen; APXS team members J. A. Berger and S. J. VanBommel for assistance regarding APXS field of view; R. B. Anderson, E. M. Lee, M. R. Rosiek, and R. M. Sucharski for work on MTF and sky flat field data analyses; T. Litwin for work on the JPL-Caltech CAHVOR model; and the personnel who helped operate MAHLI on Mars including B. Baker, M. Beach, A. Godber, C. Hardgrove, D. Harker, P. Herrera, J. Hudgins, E. Jensen, A. Magee, E. McCartney, L. Posiolova, N. Stewart, and R. Zimdar.

References

Anderson, R. B. and Bell III, J. F. (2010) Geologic mapping and characterization of Gale crater and implications for its potential as a Mars Science Laboratory landing site, *Mars 5*, 76–128. doi:10.1555/mars.2010.0004

Anderson, R. C., Jandura, L., Okon, A. B., Sunshine, D., Roumeliotis, C., Beegle, L. W., Hurowitz, J., Kennedy, B., Limonadi, D., McCloskey, S., Robinson, M., Seybold, C., and Brown, K. (2012) Collecting samples in Gale crater, Mars; an overview of the Mars Science Laboratory Sample Acquisition, Sample Processing and Handling System, *Space Sci. Rev. 170*, 57–75. doi:10.1007/s11214-012-9898-9

Arvidson, R. E., Bellutta, P., Calef, F., Fraeman, A. A., Garvin, J. B., Gasnault, O., Grant, J. A., Grotzinger, J. P., Hamilton, V. E., Heverly, M., Iagnemma, K. A., Johnson, J. R., Lanza, N., LeMouélic, S., Mangold, N., Ming, D. W., Mehta, M., Morris, R. V., Newsom, H. E., Rennó, N., Rubin, D., Schieber, J., Sletten, R., Stein, N. T., Thuillier, F., Vasavada, A. R., Vizcaino, J., and Wiens, R. C. (2014) Terrain physical properties derived from orbital data and the first 360 sols of Mars Science Laboratory Curiosity rover observations in Gale crater, *J. Geophys. Res. 119*, 1322–1344. doi:10.1002/2013JE004605

Bayer, B. E. (1976) Color imaging array, U.S. Patent 3971065.

Bell III, J. F., Squyres, S. W., Herkenhoff, K. E., Maki, J. N., Arneson, H. M., Brown, D., Collins, S. A., Dingizian, A., Elliot, S. T., Hagerott, E. C., Hayes, A. G., Johnson, M. J., Johnson, J. R., Joseph, J., Kinch, K., Lemmon, M. T., Morris, R. V., Scherr, L., Schwochert, M., Shepard, M. K., Smith, G. H., Sohl-Dickstein, J. N., Sullivan, R. J., Sullivan, W. T., and Wadsworth, M. (2003) Mars Exploration Rover Athena Panoramic Camera (Pancam) investigation, *J. Geophys. Res. 108*, 8063. doi:10.1029/2003JE002070

Bell III, J. F., Joseph, J., Sohl-Dickstein, J. N., Arneson, H. M., and Johnson, M. J. (2006) In-flight calibration and performance of the Mars Exploration Rover Panoramic Camera (Pancam) instruments, *J. Geophys. Res. 111*, E02S03. doi:10.1029/2005JE002444

Berger, J. A., King, P. L., Gellert, R., Campbell, J. L., Boyd, N. I., Pradler, I., Perrett, G. M., Edgett, K. S., Van Bommel, S. J. V., Schmidt, M. E., and Lee R. E. H. (2014) MSL-APXS titanium observation tray measurements: Laboratory experiments and results for the Rocknest fines at the Curiosity field site in Gale crater, Mars, *J. Geophys. Res. 119*, 1046–1060. doi:10.1002/2013JE004519

Bhandari, P., Birur, G., Bame, D., Mastropietro, A. J., Miller, J., Karlmann, P., Liu, Y., and Anderson, K. (2013) Performance of the mechanically pumped fluid loop rover heat rejection system used for thermal control of the Mars Science Laboratory Curiosity rover on the surface of Mars, *43rd International Conference on Environmental Systems*, Vail, Colorado, USA, 14–18 July 2013, AIAA-2013-3323. doi:10.2514/6.2013-3323

Blake, D. F., Morris, R. V., Kocurek, G., Morrison, S. M., Downs, R. T., Bish, D., Ming, D. W., Edgett, K. S., Rubin, D., Goetz, W., Madsen, M. B., Sullivan, R., Gellert, R., Campbell, I., Treiman, A. H., McLennan, S. M., Yen, A. S., Grotzinger, J., Vaniman, D. T., Chipera, S. J., Achilles, C. N., Rampe, E. B., Sumner, D., Meslin, P.-Y., Maurice, S., Forni, O., Gasnault, O., Fisk, M., Schmidt, M., Mahaffy, P., Leshin, L. A., Glavin, D., Steele, A., Freissinet, C., Navarro-González, R., Yingst, R. A., Kah, L. C., Bridges, N.,

Lewis, K. W., Bristow, T. F., Farmer, J. D., Crisp, J. A., Stolper, E. M., Des Marais, D. J., Sarrazin, P., and the MSL Science Team (2013) Curiosity at Gale crater, Mars: Characterization and analysis of the Rocknest sand shadow, *Science 341*. doi:10.1126/science.1239505

Burt, P. J. and Adelson, E. H. (1983) A multiresolution spline with application to image mosaics, *Assoc. Comput. Mach. Trans. Graph. 2*, 217–236. doi:10.1145/245.247

Cabrol, N. A., Grin, E. A., Newsom, H. E., Landheim, R., and McKay, C. P. (1999) Hydrogeologic evolution of Gale crater and its relevance to the exobiological exploration of Mars, *Icarus 139*, 235–245. doi:10.1006/icar.1999.6099

Campbell, J. L., King, P. L., Burkemper, L., Berger, J. A., Gellert, R., Boyd, N. I., Perrett, G. M., Pradler, I., Thompson, L., Edgett, K. S., and Yingst, R. A. (2014) The Mars Science Laboratory APXS calibration target: Comparison of Martian measurements with the terrestrial calibration, *Nucl. Instrum. Meth. B 323*, 49–58. doi:10.1016/j.nimb.2014.01.011

Caplinger, M. (2013) MSSS MSL camera calibration summary, Version 1.1, File MSL_MMM_CAL.TXT archived by the NASA Planetary Data System, 9 May 2013.

Carr, G. A., L. Jones, and Moreno, V. (2012) Mars Science Laboratory (MSL) power system architecture, *AIAA 10th International Energy Conversion Engineering Conference*, Atlanta, Georgia, USA, 30 July – 1 August 2012, AIAA-2012-4058, doi:10.2514/6.2012-4058, 2012.

CCITT, International Telegraph and Telephone Consultative Committee (1993) Information Technology – Digital Compression and Coding of Continuous-tone Still Images – Requirements and Guidelines – Recommendation T.81 (9/92), International Telecommunication Union.

Collins, C. L. and Robinson, M. L. (2013) Accuracy analysis and validation of the Mars Science Laboratory (MSL) robotic arm, *Proceedings of the ASME 2013 International Design Engineering Technical Conferences and Computers and Information in Engineering Conference, Mechanisms and Robotics Conference 6B*, Portland, Oregon, USA, 4–7 August 2013. doi:10.1115/DETC2013-13034

Di, K. and Li, R (2004) CAHVOR camera model and its photogrammetric conversion for planetary applications, *J. Geophys. Res. 109*, E04004. doi:10.1029/2003JE002199

DiBiase, D. R. and Laramee, J. (2009) Mars Hand Lens Imager: lens mechanical design, *Proceedings of the 2009 IEEE Aerospace Conference*, Big Sky, Montana, USA, 7–14 March 2009, 1215. doi:10.1109/AERO.2009.4839434

Edgett, K. S., Bell III, J. F., Herkenhoff, K. E., Heydari, E., Kah, L. C., Minitti, M. E., Olson, T. S., Rowland, S. K., Schieber, J., Sullivan, R. J., Yingst, R. A., Ravine, M. A., Caplinger, M. A., and Maki. J. N. (2005) The Mars Hand Lens Imager (MAHLI) for the 2009 Mars Science Laboratory, Abstract 1170, *Lunar and Planetary Science Conference 36*, League City, Texas, USA, 14–18 March 2005.

Edgett, K. S., Yingst, R. A., Ravine, M. A., Caplinger, M. A., Maki, J. N., Ghaemi, F. T., Schaffner, J. A., Bell J. F. III, Edwards, L. J., Herkenhoff, K. E., Heydari, E., Kah, L. C., Lemmon, M. T., Minitti, M. E., Olson, T. S., Parker, T. J., Rowland, S. K., Schieber, J., Sullivan, R. J., Sumner, D. Y., Thomas, P. C., Jensen, E. H., Simmonds, J. J., Sengstacken, A. J., Willson, R. G., and Goetz, W. (2012) Curiosity's Mars Hand Lens Imager (MAHLI) investigation, *Space Sci. Rev. 170*, 259–317. doi:10.1007/s11214-012-9910-4

Edwards, C. D., Bell, D. J., Gladden, R. E., Ilott, P. A., Jedrey, T. C., Johnston, M. D., Maxwell, J. L., Mendoza, R., McSmith, G. W., Potts, C. L., Schratz, B. C., Shihabi, M. M., Srinivasan, J. M., Varghese, P., Sanders, S. S., and Denis, M. (2013) Relay support for the Mars Science Laboratory mission, *Proceedings of the 2013 IEEE Aerospace Conference*, Big Sky, Montana, USA, 2–9 March 2013. doi:10.1109/AERO.2013.6497325

Farley, K. A., Malespin, C., Mahaffy, P., Grotzinger, J. P., Vasconcelos, P. M., Milliken, R. E., Malin, M., Edgett, K. S., Pavlov, A. A., Hurowitz, J. A., Grant, J. A., Miller, H. B., Arvidson, R., Beegle, L., Calef, F., Conrad, P. G., Dietrich, W. E., Eigenbrode, J., Gellert, R., Gupta, S., Hamilton, V., Hassler, D. M., Lewis, K. W., McLennan, S. M., Ming, D., Navarro-González, R., Schwenzer, S. P., Steele, A., Stolper, E. M., Sumner, D. Y., Vaniman, D., Vasavada, A., Williford, K., Wimmer-Schweingruber, R. F., and the MSL Science Team (2014) In situ radiometric and exposure age dating of the Martian surface, *Science 343*. doi:10.1126/science.1247166

Freissinet, C., Glavin, D. P., Mahaffy, P. R., Miller, K. E., Eigenbrode, J. L., Summons, R. E., Brunner, A. E., Buch, A., Szopa, C., Archer P. D. Jr., Franz, H. B., Atreya, S. K., Brinckerhoff, W. B., Cabane, M., Coll, P., Conrad, P. G., Des Marais, D. J., Dworkin, J. P., Fairén, A. G., François, P., Grotzinger, J. P., Kashyap, S., ten Kate, I. L., Leshin, L. A., Malespin, C. A., Martin, M. G., Martin-Torres, F. J., McAdam, A. C., Ming, D. W., Navarro-González, R., Pavlov, A. A., Prats, B. D., Squyres, S. W., Steele, A., Stern, J. C., Sumner, D. Y., Sutter, B., Zorzano, M-P., and the MSL Science Team (2015) Organic molecules in the Sheepbed mudstone, Gale crater, Mars, *J. Geophys. Res. 120*(3) 495–514. doi:10.1002/2014JE004737

Garvin, J. B., Edgett, K. S., Kennedy, M. R., Minitti, M. E., McBride, M. J., Krezoski, G. M., Dotson, R., Yingst, R. A., Gómez-Elvira, J., and Conrad, P. G. (2015) Assessment of micro-relief derived from Curiosity's MAHLI stereo imaging, Abstract 2482, *Lunar and Planetary Science Conference 46*, The Woodlands, Texas, USA, 16–20 March 2015.

Gennery, D. B. (2001) Least-squares camera calibration including lens distortion and automatic editing of calibration points, In: *Calibration and Orientation of Cameras in Computer Vision, Grun*, A. and Huang, T. (Eds.), Springer, Berlin, Germany, 123–136. doi:10.1007/978-3-662-04567-1_5

Gennery, D. B. (2006) Generalized camera calibration including fish-eye lenses, *Int. J. Comput. Vis. 68*, 239–266. doi:10.1007/s11263-006-5168-1

Getreuer, P. (2011) Zhang–Wu directional LMMSE image demosaicking, *Image Processing On Line 1*. doi:10.5201/ipol.2011.g_zwld

Ghaemi, F. T. (2009) Design and fabrication of lenses for the color science cameras aboard the Mars Science Laboratory rover, *Opt. Eng. 48*, 103002. doi:10.1117/1.3251343

Ghosh, S., Froebrich, D., and Freitas, A. (2008) Robust autonomous detection of the defective pixels in detectors using a probabilistic technique, *Appl. Opt. 47*, 6904–6924. doi:10.1364/AO.47.006904

Golombek, M., Grant, J., Kipp, D., Vasavada, A., Kirk, R., Fergason, R., Bellutta, P., Calef, F., Larsen, K., Katayama, Y., Huertas, A., Beyer, R., Chen, A., Parker, T., Pollard, B., Lee, S., Sun, Y., Hoover, R., Sladek, H., Grotzinger, J., Welch, R., Noe Dobrea, E., Michalski, J., and Watkins, M. (2012) Selection of the Mars Science Laboratory landing site, *Space Sci. Rev. 170*, 641–737. doi:10.1007/s11214-012-9916-y

Gómez-Elvira, J., Armiens, C., Castañer, L., Domínguez, M., Genzer, M., Gómez, F., Haberle, R., Harri, A.-M., Jiménez, V., Kahanpää, H., Kowalski, L., Lepinette, A., Martín, J., Martínez-Frías, J., McEwan, I., Mora, L., Moreno, J., Navarro, S., de Pablo, M. A., Peinado, V., Peña, A., Polkko, J., Ramos, M., Renno, N. O., Ricart, J., Richardson, M., Rodríguez-Manfredi, J., Romeral, J., Sebastián, E., Serrano, J., de la Torre Juárez, M., Torres, J., Torrero, F., Urquí, R., Vázquez, L., Velasco, T., Verdasca, J., Zorzano, M.-P., and Martín-Torres, J. (2012) REMS: The environmental sensor suite for the Mars Science Laboratory rover, *Space Sci. Rev. 170*, 583–640. doi:10.1007/s11214-012-9921-1

Grotzinger, J. (2009) Beyond water on Mars, *Nat. Geosci. 2*, 231–233. doi:10.1038/ngeo480

Grotzinger, J. P., Crisp, J., Vasavada, A. R., Anderson, R. C., Baker, C. J., Barry, R., Blake, D. F., Conrad, P., Edgett, K. S., Ferdowski, B., Gellert, R., Gilbert, J. B., Golombek, M., Gómez-Elvira, J., Hassler, D. M., Jandura, L., Litvak, M., Mahaffy, P., Maki, J., Meyer, M., Malin, M. C., Mitrofanov, I., Simmonds, J. J., Vaniman, D., Welch, R. V., and Wiens, R. C. (2012) Mars Science Laboratory mission and science investigation, *Space Sci. Rev. 170*, 5–56. doi:10.1007/s11214-009-9892-2

Grotzinger, J. P., Sumner, D. Y., Kah, L. C., Stack, K., Gupta, S., Edgar, L., Rubin, D., Lewis, K., Schieber, J., Mangold, N., Milliken, R., Conrad, P. G., DesMarais, D., Farmer, J., Siebach, K., Calef III, F., Hurowitz, J., McLennan, S. M., Ming, D., Vaniman, D., Crisp, J., Vasavada, A., Edgett, K. S., Malin, M., Blake, D., Gellert, R., Mahaffy, P., Wiens, R. C., Maurice, S., Grant, J. A., Wilson, S., Anderson, R. C., Beegle, L., Arvidson, R., Hallet, B., Sletten, R. S., Rice, M., Bell III, J., Griffes, J., Ehlmann, B., Anderson, R. B., Bristow, T. F., Dietrich, W. E., Dromart, G., Eigenbrode, J., Fraeman, A., Hardgrove, C., Herkenhoff, K., Jandura, L., Kocurek, G., Lee, S., Leshin, L. A., Leveille, R., Limonadi, D., Maki, J., McCloskey, S., Meyer, M., Minitti, M., Newsom, H., Oehler, D., Okon, A., Palucis, M., Parker, T., Rowland, S., Schmidt, M., Squyres, S., Steele, A., Stolper, E., Summons, R., Treiman, A., Williams, R., Yingst, A., and the MSL Science Team (2014) A habitable fluvio-lacustrine environment at Yellowknife Bay, Gale crater, Mars, *Science 343*, doi:10.1126/science.1242777

Grotzinger, J. P., Crisp, J. A., Vasavada, A. R., and the MSL Science Team (2015) Curiosity's mission of exploration at Gale crater, Mars, *Elements 11*, 19–26. doi:10.2113/gselements.11.1.19

Harris, C. and Stephens, M. (1988) A combined corner and edge detector, *Proceedings of the 4th Alvey Vision Conference*, University of Manchester, 31 August – 2 September 1988, 147–151. doi:10.5244/C.2.23

Herkenhoff, K. E., Squyres, S. W., Bell III, J.F., Maki, J. N., Arneson, H. M., Bertelson, P, Brown, D. I., Collins, S. A., Dingizian, A., Elliot, S. T., Goetz, W., Hagerott, E. C., Hayes, A. G., Johnson, M. J., Kirk, R. L., McLennan, S., Morris, R. V., Scherr, L. M., Schwochert, M. A., Shiraishi, L. R., Smith, G. H., Soderblom, L. A., Sohl–Dickstein, J. N., and Wadsworth, M. V. (2003) Athena Microscopic Imager investigation, *J. Geophys. Res. 108*, 8065. doi:10.1029/2003JE002076

Herkenhoff, K. E., Squyres, S. W., Anderson, R., Archinal, B. A., Arvidson, R. E., Barrett, J. M., Becker, K. J., Bell III, J. F., Budney, C., Cabrol, N. A., Chapman, M. G., Cook, C., Ehlmann, B. L., Farmer, J., Franklin, B., Gaddis, L. R., Galuszka, D. M., Garcia, P. A., Hare, T. M., Howington-Kraus, E., Johnson, J. R., Johnson, S., Kinch, K., Kirk, R. L., Lee, E. M., Leff, C., Lemmon, M., Madsen, M. B., Maki, J. N., Mullins, K. F., Redding, B. L., Richter, L., Rosiek, M. R., Sims, M. H., Soderblom, L. A., Spanovich, N.,

Springer, R., Sucharski, R. M., Sucharski, T., Sullivan, R., Torson, J. M., and Yen, A. (2006) Overview of the Microscopic Imager investigation during Spirit's first 450 sols in Gusev crater, *J. Geophys. Res. 111*, E02S04. doi:10.1029/2005JE002574

Heverly, M., Matthews, J., Lin, J., Fuller, D., Maimone, M., Biesiadecki, J., and Leichty, J. (2013) Traverse performance characterization for the Mars Science Laboratory rover, *J. Field Robot. 30*, 835–846. doi:10.1002/rob.21481

Jandura, L., Burke, K., Kennedy, B., Melko, J., Okon, A., and Sunshine, D. (2010) An overview of the Mars Science Laboratory sample acquisition, sample processing and handling subsystem, *American Society of Civil Engineers Proceedings of the Earth and Space 2010 Conference*, 14–17 March 2010, Honolulu, Hawaii, USA doi:10.1061/41096(366)89

Janesick, J. R., Klaasen, K. P., and Elliott, T. (1987) Charge-coupled-device charge-collection efficiency and the photon-transfer technique, *Opt. Eng. 26*, 972–980. doi:10.1117/12.7974183

Johnson, J. R., Bell III, J. F., Hayes, A., Deen, R., Godber, A., Arvidson R. E., Kuhn, S., Carsten, J., and Kennedy, M. R. (2015) Recent Mastcam and MAHLI visible/near-infrared spectrophotometric observations: Kimberley to Hidden Valley, Abstract 1424, *Lunar and Planetary Science Conference 46*, The Woodlands, Texas, USA, 16–20 March 2015.

Kah, L. C. and the MSL Science Team (2015) Images from Curiosity: A new look at Mars, *Elements 11*, 27–32. doi:10.2113/gselements.11.1.27

Kinch, K. M., Madsen, M. B., Bell III, J. F., Johnson, J. R., Goetz, W., and the MSL Science Team (2013) Dust on the Curiosity mast camera calibration target, Abstract 1061, *Lunar and Planetary Science Conference 44*, The Woodlands, Texas, USA, 18–22 March 2013.

Li, X., Gunturk, B., and Zhang, L. (2008) Image demosaicking: A systematic survey, *Visual Communications and Image Processing*, Pearlman, W. A., Woods, J. W., Lu, L. (Eds.), Proceedings of the SPIE, 6822, San Jose, California, USA, 27 January 2008, 68221J. doi:10.1117/12.766768

Lucas, B. D. and Kanade, T. (1981) An iterative image registration technique with an application to stereo vision, *Proceedings of the 1981 DARPA Image Understanding Workshop*, Cambridge, Massachusetts, USA, April 1981, 121–130.

Maki, J., Thiessen, D., Pourangi, A., Kobzeff, P., Litwin, T., Scherr, L., Elliott, S., and Dingizian, A. (2012) The Mars Science Laboratory engineering cameras, *Space Sci. Rev. 170*, 77–93. doi:10.1007/s11214-012-9882-4

Malin, M. C. and Edgett, K. S. (2000) Sedimentary rocks of early Mars, *Science 290*, 1927–1937. doi:10.1126/science.290.5498.1927

Malin, M. C., Caplinger, M. A., Edgett, K. S., Ghaemi, F. T., Ravine, M. A., Schaffner, J. A., Maki, J. N., Willson, R. G., Bell III, J. F., Cameron, J. F., Dietrich, W. E., Edwards, L. J., Hallet, B., Herkenhoff, K. E., Heydari, E., Kah, L. C., Lemmon, M. T., Minitti, M. E., Olson, T. S., Parker, T. J., Rowland, S. K., Schieber, J., Sullivan, R. J., Sumner, D. Y., Thomas, P. C., and Yingst, R. A. (2009) The Mars Science Laboratory (MSL) Mars Descent Imager (MARDI) flight instrument, Abstract 1199, *Lunar and Planetary Science Conference 40*, The Woodlands, Texas, USA, 23–27 March 2009.

Malin, M. C., Caplinger, M. A., Edgett, K. S., Ghaemi, F. T., Ravine, M. A., Schaffner, J. A., Baker, J. M., Bardis, J. D., DiBiase, D. R., Maki, J. N., Willson, R. G., Bell III, J. F., Dietrich, W. E., Edwards, L. J., Hallet, B., Herkenhoff, K. E., Heydari, E., Kah, L. C., Lemmon, M. T., Minitti, M. E., Olson, T. S., Parker, T. J., Rowland, S. K., Schieber, J., Sullivan, R. J., Sumner, D. Y., Thomas, P. C., and Yingst, R. A. (2010) The Mars Science Laboratory (MSL) Mast-mounted cameras (Mastcams) flight instruments, Abstract 1123, *Lunar and Planetary Science Conference 41*, The Woodlands, Texas, USA, 1–5 March 2010.

Malin, M., Edgett, K., Jensen, E., Lipkaman, L. (2013) Mast Camera (Mastcam), Mars Hand Lens Imager (MAHLI), and Mars Descent Imager (MARDI) Experiment Data Record (EDR) and Reduced Data Record (RDR) PDS data products, version 1.2, *Mars Science Laboratory Project Software Interface Specification (SIS)*, JPL D-75410, SIS-SCI0135-MSL, file MSL_MMM_EDR_RDR_DPSIS.PDF archived by the NASA Planetary Data System, 29 October 2013.

Malvar, H. S., He, L.-W., and Cutler, R. (2004) High-quality linear interpolation for demosaicing of Bayer-patterned color images, *Proceedings of the IEEE International Conference on Acoustics, Speech, and Signal Processing 3*, Montreal, Quebec, Canada, 17–21 May 2004, 485–488. doi:10.1109/ICASSP.2004.1326587

Markiewicz, W. J., Sablotny, R. M., Keller, H. U., Thomas, N., Titov, D., and Smith, P. H. (1999) Optical properties of the Martian aerosols as derived from Imager for Mars Pathfinder midday sky brightness data, *J. Geophys. Res. 104*(E4), 9009–9017. doi:10.1029/1998JE900033

McBride, M. J., M. E. Minitti, M. E., Stack, K. M., Yingst, R. A., Edgett, K. S., Goetz, W., Herkenhoff, K. E., Heydari, E., Kah, L. C., Rowland, S. K., Schieber, J., Harker, D., Kennedy, M. R., Krezoski, G. M., Lipkaman, L., Nixon, B., Van Beek, J. (2015) Mars Hand Lens Imager (MAHLI) observations at the Pahrump Hills field site, Gale crater, Abstract 2885, *Lunar and Planetary Science Conference 46*, The Woodlands, Texas, USA, 16–20 March 2015.

Mikhail, E. M., Bethel, J. S., McGlone, J. C. (2001) *Introduction to Modern Photogrammetry*, John Wiley and Sons, New York.

Milliken, R. E., Grotzinger, J. P., and Thomson, B. J. (2010) Paleoclimate of Mars as captured by the stratigraphic record in Gale crater, *Geophys. Res. Lett. 37*, L04201. doi:10.1029/2009GL041870

Minitti, M. E., Kah, L. C., Yingst, R. A., Edgett, K. S., Anderson, R. C., Beegle, L. W., Carsten, J. L., Deen, R. G., Goetz, W., Hardgrove, C., Harker, D. E., Herkenhoff, K. E., Hurowitz, J. A., Jandura, L., Kennedy, M. R., Kocurek, G., Krezoski, G. M., Kuhn, S. R., Limonadi, D., Lipkaman, L., Madsen, M. B., Olson, T. S., Robinson, M. L., Rowland, S. K., Rubin, D. M., Seybold, C., Schieber, J., Schmidt, M., Sumner, D. Y., Tompkins, V. V., Van Beek, J. K., and Van Beek, T. (2013) MAHLI at the Rocknest sand shadow: Science and science-enabling activities, *J. Geophys. Res. 118*, 2338–2360. doi:10.1002/2013JE004426

Minitti, M. E., Edgett, K. S., Yingst, R. A., Conrad, P. G., Fisk, M., Hardgrove, C. J., Herkenhoff, K. E., Kah, L. C., Kennedy. M. R., Krezoski, G. M., Lemmon, M. T., Lipkaman, L., Kuhn, S. R., Robinson, M. L., Tompkins, V. V., Treiman, A., and Williford, K. H. (2014) MAHLI after dark: Nighttime Mars Hand Lens Imager observations under LED illumination, Abstract 2029, *Lunar and Planetary Science Conference 45*, The Woodlands, Texas, USA, 17–21 March 2014.

Mitrofanov, I. G., Litvak, M. L., Varenikov, A. B., Barmakov Y. N., Behar, A., Bobrovnitsky, Y. I., Bogolubov, E. P., Boynton W. V., Harshman, K., Kan, E., Kozyrev, A. S., Kuzmin, R. O., Malakhov, A. V., Mokrousov, M. I., Ponomareva, S. N., Ryzhkov, V. I., Sanin, A. B., Smirnov, G. A., Shvetsov, V. N., Timoshenko, G. N., Tomilina, T. M., Tret'yakov, V. I., and Vostrukhin, A. A. (2012) Dynamic Albedo of Neutrons (DAN) experiment onboard NASA's Mars Science Laboratory, *Space Sci. Rev. 170*, 559–582. doi:10.1007/s11214-012-9924-y

NASA (1995) *An Exobiological Strategy for Mars Exploration*, NASA Special Publication SP-530, U.S. Government Printing Office, Washington, D.C., USA, 56 pp., April 1995.

Novak, K. S., Kempenaar, J. E., Bhandari, P., and Dudik, B. A. (2012) Mars Science Laboratory rover system thermal test, *42nd International Conference on Environmental Systems*, San Diego, California, USA, 15–19 July 2012, AIAA-2012-3516. doi:10.2514/6.2012-3516

ON Semiconductor (2014) Vertical timing optimization for interline CCD image sensors, ON Semiconductor Application Note, AND9190/D, revision 2, September 2014.

Pollack, J. B., Ockert-Bell, M., and Shepard, M. K. (1995) Viking lander image analysis of Martian atmospheric dust, *J. Geophys. Res. 100*, 5235–5250. doi:10.1029/94JE02640

Pye, K. (1987) *Aeolian Dust and Dust Deposits*, Academic, London, UK.

Reichenbach, S. E., Park, S. K., and Narayanswamy, R. (1991) Characterizing digital image acquisition devices, *Opt. Eng. 30*(2), 170–177. doi:10.1117/12.55783

Robinson, M. R., Collins, C., Leger, P., Carsten, J., Tompkins, V., Hartman, F., and Yen, J. (2013a) In-situ operations and planning for the Mars Science Laboratory robotic arm: The first 200 sols, *8th International Conference on System of Systems Engineering*, Maui, Hawaii, USA, 2–6 June 2013, 153–158. doi:10.1109/SYSoSE.2013.6575259

Robinson, M. R., Collins, C., Leger, P., Kim, W., Carsten, J., Tompkins, V., Trebli–Ollennu, A., and Florow, B. (2013b) Test and validation of the Mars Science Laboratory robotic arm, *8th International Conference on System of Systems Engineering*, Maui, Hawaii, USA, 2–6 June 201, 184–189. doi:10.1109/SYSoSE.2013.6575264

Schieber, J. (2001) Finding life on Mars: A mudrock geologist's perspective, Abstract 1072, *Lunar and Planetary Science Conference 32*, Houston, Texas, USA, 12–16 March 2001.

Schieber, J., Malin, M. C., Olson, T. S., Calef, F., Comeaux, K., and the MSL Science Team (2013) The final 2½ minutes of terror – What we learned about the MSL landing from the images taken by the MARDI descent imager, Abstract 1260, *Lunar and Planetary Science Conference 44*, The Woodlands, Texas, USA, 18–22 March 2013.

Sengupta, A., Kulleck, J., Sell, S., Van Norman, J., Mehta, M., and Pokora, M. (2009) Mars lander engine plume impingement environment of the Mars Science Laboratory, *2009 IEEE Aerospace Conference*, Big Sky, Montana, USA, 7–14 March 2009. doi:10.1109/AERO.2009.4839345

Shi, J. and Tomasi, C. (1994) Good features to track, *Proceedings of the 1994 IEEE Computer Society Conference on Computer Vision and Pattern Recognition*, Seattle, Washington, USA, 21–23 June 1994, 593–600. doi:10.1109/CVPR.1994.323794

Siebach, K. L. and Grotzinger, J. P. (2014) Volumetric estimates of ancient water on Mount Sharp based on boxwork deposits, Gale crater, Mars, *J. Geophys. Res. 119*, 189–198. doi:10.1002/2013JE004508

Stack, K. M., Grotzinger, J. P., Kah, L. C., Schmidt, M. E., Mangold, N., Edgett, K. S., Sumner, D. Y., Siebach, K. L., Nachon, M., Lee, R., Blaney, D. L., De Flores, L. P., Edgar, L. A., Fairén, A. G., Leshin, L. A., Maurice, S., Oehler, D. Z., Rice, M. S., and Wiens, R. C. (2014) Diagenetic origin of nodules in the Sheepbed member, Yellowknife Bay formation, Gale crater, Mars, *J. Geophys. Res. 119*, 1637–1664. doi:10.1002/2014JE004617

Summons, R. E., Amend, J. P., Bish, D., Buick, R., Cody, G. D., Des Marais, D. J., Dromart, G., Eigenbrode, J. L., Knoll, A. H., and Sumner, D. Y. (2011) Preservation of Martian organic and environmental records: Final report of the Mars Biosignature Working Group, *Astrobiol. 11*, 157–181. doi:10.1089/ast.2010.0506

Thomson, B. J., Bridges, N. T., Milliken, R., Baldridge, A., Hook, S. J., Crowley, J. K., de Souza Filho, C. R., Brown, A. J., and Weitz, C. M. (2011) Constraints on the origin and evolution of the layered mound in Gale crater, Mars, using Mars Reconnaissance Orbiter data, *Icarus 214*, 413–432. doi:10.1016/j.icarus.2011.05.002

Tomasko, M. B., Doose, L. R., Lemmon, M., Smith, P. H., and Wegryn, E. (1999) Properties of dust in the Martian atmosphere from the imager on Mars Pathfinder, *J. Geophys. Res. 104*, 8987–9007. doi:10.1029/1998JE900016

Truesense Imaging, Inc. (2013) Using interline CCD image sensors in high intensity lighting conditions, Truesense Imaging Reference Document, revision 2.0 PS-0056, http://www.truesenseimaging.com/support/reference-documents/doc_download/3-use-of-ccds-in-high-intensity-visible-lighting-conditions, 1 October 2013.

Vaniman, D. T., Bish, D. L., Ming, D. W., Bristow, T. F., Morris, R. V., Blake, D. F., Chipera, S. J., Morrison, S. M., Treiman, A. H., Rampe, E. B., Rice, M., Achilles, C. N., Grotzinger, J., McLennan, S. M., Williams, J., Bell III, J., Newsom, H., Downs, R. T., Maurice, S., Sarrazin, P., Yen, A. S., Morookian, J. M., Farmer, J. D., Stack, K., Milliken, R. E., Ehlmann, B., Sumner, D. Y., Berger, G., Crisp, J. A., Hurowitz, J. A., Anderson, R., Des Marais, D., Stolper, E. M., Edgett, K. S., Gupta, S., Spanovich, N., and the MSL Science Team (2014) Mineralogy of a mudstone at Yellowknife Bay, Gale crater, Mars, *Science 343*. doi:10.1126/science.1243480

Vasavada, A. R., Grotzinger, J. P., Arvidson, R. E., Calef, F. J., Crisp, J. A., Gupta, S., Hurowitz, J., Mangold, N., Maurice, S., Schmidt, M. E., Wiens, R. C., Williams, R. M. E., and Yingst, R. A. (2014) Overview of the Mars Science Laboratory mission: Bradbury Landing to Yellowknife Bay and beyond, *J. Geophys. Res. 119*, 1134–1161. doi:10.1002/2014JE004622

Wentworth, C. K. (1922) A scale of grade and class terms for clastic sediments, *J. Geol. 30*, 377–392. doi:10.1086/622910

Williams, R. M. E., Grotzinger, J. P., Dietrich, W. E., Gupta, S., Sumner, D. Y., Wiens, R. C., Mangold, N., Malin, M. C., Edgett, K. S., Maurice, S., Forni, O., Gasnault, O., Ollila, A., Newsom, H. E., Dromart, G., Palucis, M. C., Yingst, R. A., Anderson, R. B., Herkenhoff, K. E., Le Mouélic, S., Goetz, W., Madsen, M. B., Koefoed, A., Jensen, J. K., Bridges, J. C., Schwenzer, S. P., Lewis, K. W., Stack, K. M., Rubin, D., Kah, L. C., Bell III, J. F., Farmer, J. D., Sullivan, R., Van Beek, T., Blaney, D. L., Pariser, O., Deen, R. G., and the MSL Science Team (2013) Martian fluvial conglomerates at Gale crater, *Science 340*, 1068–1072. doi:10.1126/science.1237317

Wray, J. J. (2013) Gale crater: The Mars Science Laboratory Curiosity rover landing site, *Int. J. Astrobiol. 12*, 25–38. doi:10.1017/S1473550412000328

Yakimovsky, Y. and Cunningham, R. (1978) A system for extracting three-dimensional measurements from a stereo pair of TV cameras, *Comput. Graph. Image Process. 7*, 195–210. doi:10.1016/0146-664X(78)90112-0

Yingst, R. A., Edgett, K. S., Kennedy, M. R., Minitti, M. E., and Ravine, M. A. (2014) Cameras on landed payload robotic arms — MAHLI on Mars and lessons learned from one Mars year of operations, Article 1031, *International Workshop on Instrumentation for Planetary Missions*, NASA Goddard Space Flight Center, Greenbelt, Maryland, USA, 4–7 November 2014.

Yotam, E., Pinsky, E., and Ami, Y. (2007) MTF for color Bayer pattern detector, *Proceedings of SPIE, 6567, Signal Processing, Sensor Fusion, and Target Recognition XVI*, Kadar, I. (Ed.), Orlando, Florida, USA, 9 April 2007, 65671M. doi:10.1117/12.723140

— end —